Functional spherical dielectric resonators at microwave and millimeter-wave frequency

Von der Fakultät Informatik, Elektrotechnik und Informationstechnik der Universität Stuttgart zur Erlangung der Würde eines Doktors der Ingenieurwissenschaften **(Dr.-Ing.)** genehmigte Abhandlung

Vorgelegt von

Georg Sterzl

aus Prien am Chiemsee

Hauptberichter:	Prof. Dr. Jan Hesselbarth
Mitberichter:	Prof. Dr. Jens Anders
Tag der mündlichen Prüfung:	06.08.2024

Institut für Hochfrequenztechnik der Universität Stuttgart

2024

Acknowledgements

Five years is around 6 % of a human life. I was in Stuttgart at the Institute of Radio Frequency Technology for over five years. During this time, I got to know a many people, and many supported me on my journey. With this text, I want to say thank you to you all!

In particular, I want to say thank you to my family, who always stuck with me; my friends, my Ph.D. colleagues; especially Utpal Dey, who was my fellow in my first years as a Ph.D. student; PD Dr.-Ing. Ning Yan Zhu, for the excellent discussion and for being somebody who was always there if something was lying in my heart; the secretariat; workshop; technology workshop, and IT.

Thank you to my cooperation partner Yu Zhu far away in Dresden.

Last but of course not least, thank you to my supervisor Prof. Dr. Jan Hesselbarth. I learned a lot directly from the challenges he gave me and indirectly by reflecting on him. One statement which burned in my head is, "If it would be easy, somebody else would have it done already." This statement often encouraged me very when things did not work out and it took a while to figure out a solution. Therefore, I learned a lot during my time under your supervision and developed a lot in the last five years. Also, I appreciate your understanding of my situation and support me when Murphy's Committee hit me with their full power and nearly everything in my life went down the drain.

To appreciate the mountain's view, you have must have been in the valley. Moreover a summit is only an intermediate step for the subsequent descent into the valley to climb even higher mountains. It's not about how many mountains you climbed and how high they are, but about enjoying the ascent and the descent and not to resting too long. (Inspired by Dale Carnegie, Dieter Lange, Fera F. Birkenbihl, Joseph Campbell).

Abstract

The most sensitive electromagnetic sensors to determine the complex permittivity are presented, evaluated, and compared for microwaves and mm-waves. Own definitions of sensitivity are presented to be able to compare the state of the art. The Spherical Dielectric Resonator (SDR) sensors are the most sensitive sensors at mm-wave and scalable to THz frequencies. Liquid Under Test (LUT)s are measured in-flow, and the permittivity of them are determined at microwaves, mm-waves, and sub THz frequencies. The needed volume of LUT could be reduced until $0.35\,\mathrm{nl}$. Also, particles in liquids at microwave and mm-wave have been detected in-flow at the sub-wavelength scale. Solutions for temperature control or getting rid of the temperature influence with another resonator mode are presented. The problems with using a Waveguide (WG) with a hole and tube inside to broadband determine the permittivity of Material Under Test (MUT) are explained.

Silicon, especially Bipolar Complementary Metal-Oxide Semiconductor (BiCMOS) Silicon–Germanium (SiGe) chips application as antennas, filters, and oscillators, are presented and compared produced with the IHP technology SG13G2. The advantages of improving the Spherical Dielectric Resonator Antenna (SDRA) on silicon chips are highlighted for passive and active multi-port cases. The presented resonator or filter with a ceramic sphere has the highest Quality (Q)-factor of all presented on-silicon chips until now. Also, a voltage-tunable resonator version is presented and used in a Voltage Controlled Oscillator (VCO) to tune the oscillator. The oscillator is generating a signal at circa $100\,\mathrm{GHz}$ and is $100\,\mathrm{MHz}$ tunable. The oscillation is extremely shock and pressure sensitive and has space for improvement.

Zusammenfassung

Es werden die empfindlichsten elektromagnetischen Sensoren zur Bestimmung der komplexen Dielektrizitätskonstante für Mikrowellen und mm-Wellen vorgestellt, bewertet und verglichen. Es werden eigene Definitionen der Empfindlichkeit präsentiert, um den Stand der Technik vergleichen zu können. Die kugelförmigen dielektrischen Resonatoren-Sensoren sind die empfindlichsten Sensoren bei mm-Wellen Frequenzen und skalierbar bis zu THz-Frequenzen. Flüssigkeiten werden im Durchfluss gemessen und ihre Permittivität bei Mikrowellen, mm-Wellen und Sub-THz-Frequenzen bestimmt. Das benötigte Volumen von den Flüssigkeiten konnte bis auf $0.35\,\mathrm{nl}$ reduziert werden. Auch Partikel in Flüssigkeiten konnten bei Mikrowellen- und mm-Wellen im Durchfluss im Sub-Wellenlängenbereich detektiert werden. Es werden Lösungen zur Temperaturkontrolle bzw. zum Herausrechnen des Temperatureinflusses mit Hilfe einer zusätzlichen elektromagnetischen Resonanzmode vorgestellt. Die Probleme bei der Verwendung eines metallischen Hohlleiters mit einem Loch und einem Rohr dadurch im Inneren zur breitbandigen Bestimmung der Permittivität von Materialien werden erläutert.

Silizium- und insbesondere BiCMOS-SiGe-Chips-Anwendungen wie Antennen, Filter und Oszillatoren, die mit der IHP-Technologie SG13G2 hergestellt wurden, werden vorgestellt und mit dem Stand der Technik verglichen. Die Vorteile sowie Details zur Verbesserung der spherischen dielektrischen Resonator-Antennen auf Siliziumchips werden für passive und aktive Multi-Port-Fälle hervorgehoben. Der vorgestellte Resonator oder auch Filter mit einer Keramikkugel hat den höchsten Qualitäts-Faktor aller bisher vorgestellten On-Silizium-Chips. Auch eine spannungsabstimmbare Version des Resonators wird vorgestellt und in einem Spannungsgesteuertem Oszillator zum Frequenzverstimmmen des Oszillators verwendet. Der Oszillator erzeugt ein Signal bei ca. $100\,\mathrm{GHz}$ und ist $100\,\mathrm{MHz}$ abstimmbar. Die Oszillation ist extrem stoß- und druckempfindlich und bietet daher Raum für Verbesserungen.

Contents

List of Figures

List of Tables

List of Acronyms

3D 3 Dimensions

AMC Artificial Magnetic Conductor

BEL Back End of Line

BEOL Back-End-Of-Line

CPW Coplanar Waveguide

DR Dielectric Resonator

DRA Dielectric Resonator Antenna

FIR Finite Impulse Response

FSS Frequency Selective Surface

GSG Ground-Signal-Ground

LBE Localised Backside Etching

LUT Liquid Under Test

MEMS MicroElectroMechanical System

MH Mosh Hardness

MMIC Monolithic Microwave Integrated Circuit

MSTL Microstip Line

MUT Material Under Test

PN Phase Noise

PTFE Polytetrafluorethylen

PTFE PolyTetraFluoroEthylene

PUT Particle Under Test

Q Quality

SDR Spherical Dielectric Resonator

SDRA Spherical Dielectric Resonator Antenna

SDRS Spherical Dielectric Resonator Sensor

SIW Substrate-Intergrated Waveguide

SNR Signal to Noise Ratio

S-parameters Scattering-parameters

SRR Split Ring Resonator

TRL Through-Reflect-Line

WG Waveguide

WGM Whispering-Gallery-Mode

VCO Voltage Controlled Oscillator

VNA Vector Network Analyzer

BiCMOS Bipolar Complementary Metal-Oxide Semiconductor

SiGe Silicon–Germanium

Chapter 1

Introduction

1.1 Motivation

Cancer is an illness everybody can suffer at any age. Often it is detected when it is already too late to heal it. Early detection is mandatory to have a chance to survive. Different methods exist to detect more giant tumors with many cancer cells. If just a few cells are to be determined, usually, cells are bred and analyzed afterward. A noninvasive and contactless way is by spectroscopy. With dielectric spectroscopy, single cell analysis, medical diagnoses and liquid mixture characterizations are possible. Therefore, a susceptible sensor for low volumes of liquid is needed. The most sensitive electromagnetic sensors are resonators, whose resonance is detuned by MUT [1]. Now the way to reduce the sensed volume is by shrinking the whole resonator and its sensing region by reducing the wavelength, which goes with increasing the frequency (or changing the dielectric materials of the resonator). This work uses SDR to accomplish that. The advantages of these dielectric resonators, also as the evaluation of these sensors, are presented in the first part of this thesis.

DRs were first studied in 1939 [26]. It took 44 years to put a Dielectric Resonator (DR) on top of a circuit as an antenna – a standing dielectric cylinder [27]. Lying cylinders and especially spheres were used on circuits instead because of their self-alignment ability. The scope of applications of the dielectric spheres on-chip extends from antennas [28], packaged gain improved antennas [29], over transitions [30], filters [10] to different sensors as for liquid spectroscopy [12] and heartbeat decoding [31].

As yet, there are more challenging handle solutions for well-radiating antennas or resonators with a high-quality factor for BiCMOS technology or other technologies with very thin substrates compared to the used wavelengths. Spherical dielectric resonator antennas (SDRA)s are a simple way to transmit the signal directly from one chip, such as a computer processor, to another. These DRs with high-quality factors would help to build oscillators or different kinds of sensors at sub-THz frequencies

on silicon chips. The combination of these different technologies is explained in this thesis.

For the SDRs, especially at frequencies beyond sub-THz, accurate placement / positioning are necessary. The most accurate produce dimensions are done by lithography, such as on-chip. Nowadays, the high-technology chips are made with silicon technology. The challenging part with silicon chips is the high loss of the doped silicon, and the thin Back End of Line (BEL)s are often in the region of $10\,\mu\mathrm{m}$. Both challenges impede using standard Microstip Line (MSTL) antennas, filters, and oscillators. The second part of this work presents how to solve this problem Monolithic Microwave Integrated Circuit (MMIC) with a dielectric sphere. However, why is it so interesting to have MMIC components on the silicon chip?

1.2 Theory basics consulting in permittivity and E-field perturbation

The theory behind the basics of this work starts with the description of electromagnetics by Maxwell's equations. He published the first version in 1865 in [32]. These equations were expanded and rewritten in different forms. The modern equations in the time-dependent form as in [33] are:

$$\nabla \times \vec{E} = -j\omega\vec{B} - \vec{M} \tag{1.1}$$

$$\nabla \times \vec{H} = j\omega\vec{D} + \vec{j} \tag{1.2}$$

$$\nabla\cdot \vec{D} = \rho \tag{1.3}$$

$$\nabla\cdot \vec{B} = 0 \tag{1.4}$$

$\vec{E}$, $\vec{H}$ are the electric, magnetic field intensity; $\vec{D}$, $\vec{B}$ are the electric, magnetic flux density; $\vec{M}$, $\vec{j}$, $\vec{\rho}$ are the magnetic, electric current density and electric charge density; ω is the angular frequency. The two belonging material equations are:

$$\vec{B} = \mu\vec{H} = \mu_0\mu_r\vec{H} \tag{1.5}$$

$$\vec{D} = \epsilon\vec{E} = \epsilon_0\epsilon_r\vec{E} \tag{1.6}$$

μ_0 and ϵ_0 belong to the free space vacuum. $\mu_r = \mu_{\text{material}}$ and $\epsilon_r = \epsilon_{\text{material}}$ are the material characteristics. μ and ϵ are complex values so that $\mu = \mu' + j\mu''$ and $\epsilon = \epsilon' + j\epsilon''$.

($j = \sqrt{-1}$). Therefore the electromagnetic loss by the permittivity is defined as $tan\delta = \Im(\epsilon)/\Re(\epsilon) = \epsilon''/\epsilon' = \sigma/(\omega\epsilon')$. σ is the material conductivity [1,34].

In [33], the equations for the E- and H-fields are combined to approximate the influence on the resonance frequency $f_0 = \omega_0/2\pi$ of any resonant cavity. The influence is the perturbation by a material in this cavity. This leads to the following equation for the relative resonance frequency shift:

$$\frac{\omega - \omega_0}{\omega_0} \simeq \frac{-\int_{V_0}(\Delta\epsilon|\vec{E}_0|^2 + \Delta\mu|\vec{H}_0|^2)dv}{\int_{V_0}(\epsilon|\vec{E}_0|^2 + \mu|\vec{H}_0|^2)dv} \tag{1.7}$$

$\Delta\mu$ and $\Delta\epsilon$ are the change of the permeability and permittivity, respectively, in another material. Therefore, when $\mu = \mu_0 * \mu_{\text{material}}$ or $\epsilon = \epsilon_0 * \epsilon_{\text{material}}$ is increased in (1.7) the resonance frequency ω_0 is decreased. Also, the wavelength $\lambda_{\text{material}}$ at a certain frequency f_{material} is dependent on μ_{material} and $\epsilon_{\text{material}}$ of the material because of the different speed of light c_{material} in this material. This looks as follows:

$$c_{\text{material}} = \frac{1}{\sqrt{\mu_0 * \mu_{\text{material}} * \epsilon_0 * \epsilon_{\text{material}}}} \tag{1.8}$$

$$\lambda_{\text{material}} = \frac{c_{\text{material}}}{f_{\text{material}}} \tag{1.9}$$

A decrease in the resonance frequency also implies that the stored energy in the resonator is increased [33]. The perturbation can be different kinds of materials. We can distinguish between conductors, intrinsic semiconductors, and insulators and also between their aggregate state [35]. This work focuses mainly on the perturbation through liquid at room temperature (25°C), and through particles inside these liquids.

1.3 Polarization mechanism and Debye values

The basic concept for spectroscopy is perturbation in this thesis. Now it is essential to understand what is causing the perturbation and why it is how it is. The perturbation is caused by the MUTs or, better said, by the complex permittivity of these materials. Permittivity is a value every material has. As with other values, such as the material density or electrical conductivity, the permittivity also depends more on the temperature. How an E-field sees the permittivity of a material is also depending on the frequency of the E-field or electromagnetic wave penetrating the material. This means the observer determines the observed, too. The material's temperature and frequency dependency is caused by various physical phenomena such as ionic conduction, dipolar relaxation, electronic polarization, and atomic polarization. A sketch

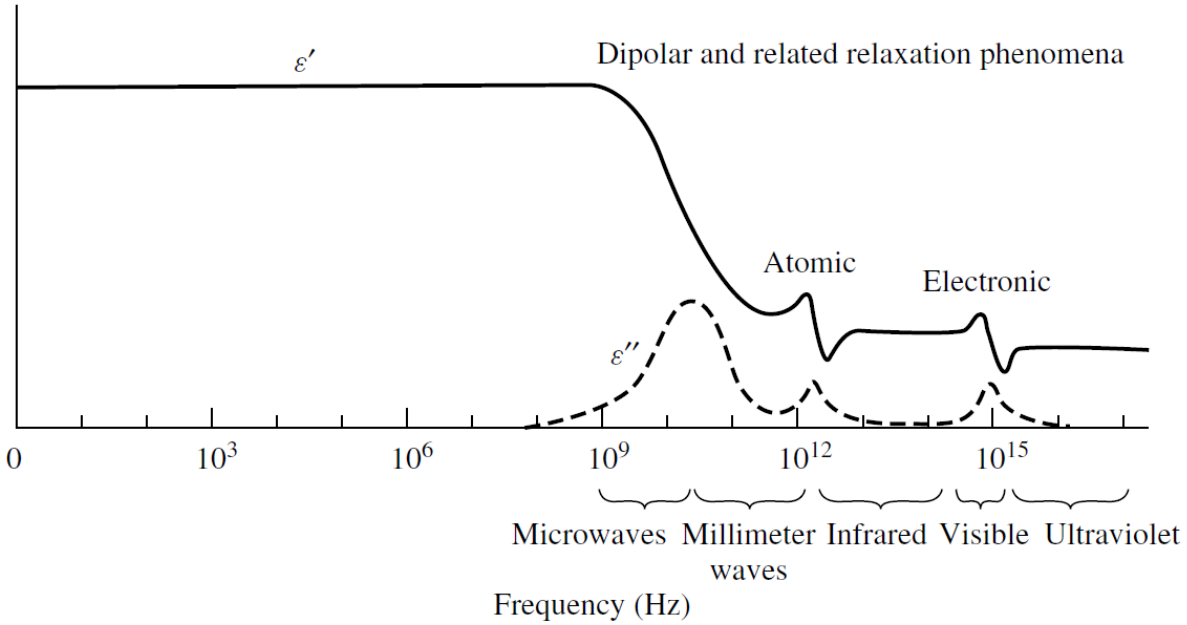

FIGURE 1.1: Sketch of permittivity behavior of material over frequency and associated relaxation phenomena [1].

of the permittivity change because of this mechanism is shown in Fig. 1.1. Electronic polarization is one of the main influences in the infra-red region and above. It occurs in neutral atoms. Therefore, an electric field has to displace the nucleus concerning the surrounding electrons.

Atomic polarization is another primary influence on the permittivity at the infrared region and higher, too. It occurs when an applied electric field stretches adjacent positive and negative ions. Electronic and atomic polarization effect nearly no loss. Therefore, other mechanisms are responsible.

The first to name is ionic conduction. At low frequencies, the complex part of the permittivity is mainly influenced by electrolytic conduction. Free ions cause electrolytic conduction in the presence of a solvent. Water is a typical example of the strength of ionic conduction's influence on permittivity. The effect of ionic conductivity is inversely proportional to operating frequency, which means it reduces to a higher frequency.

The last mechanism to name, which is also the most important for this thesis, is dipolar polarization. It is responsible for the permittivity peaks at microwave frequencies [1]. Dipolar polarization is when a molecule, especially a dipole, changes its orientation inside because of the E-field. With increasing frequency, it will rotate around its axe and stay shorter in the same rotation position until it does not manage any more the $180°$ rotation. With increasing the frequency, the rotation deflection will be less and less from this frequency. The loss $\tan\delta$ is behaving the same way. The loss

starts low, then it increases with increasing frequency until to the frequency when the molecule can make its full half rotation, and decreases afterward with higher frequency. A way to describe this behavior in most cases is with the Debye model. The Debye model predicts that the dielectric constant of a material is frequency-dependent and can be written as:

$$\epsilon(\omega) = \epsilon_\infty + \frac{\epsilon_s - \epsilon_\infty}{1 + i\omega\tau} \tag{1.10}$$

where ϵ_∞ is the high-frequency dielectric constant, ϵ_s is the static dielectric constant, ω is the angular frequency of the applied electric field, $i = \sqrt{-1}$, and τ is the relaxation time of the dipoles.

The high-frequency dielectric constant represents the material's polarization due to electronic charge displacement and is independent of frequency. The static dielectric constant represents the material's polarization due to the alignment of the dipoles in the absence of an electric field.

The relaxation time τ represents the characteristic time for the dipoles to rotate in response to the applied electric field. It is related to the viscosity and temperature of the material, as well as the size and shape of the dipoles.

The Debye model is often used to describe the behavior of polar solvents, such as water and alcohols, and polar molecules, such as those containing O-H, N-H, or C=O bonds. The model provides a simple way to estimate the dielectric constant of a material as a function of frequency, which is essential for understanding the behavior of the material in various applications, such as in capacitors, dielectric materials, and polar solvents [36].

According to the established Debye model for molecular-dipole-relaxation, the real and imaginary components of the complex permittivity of nearly all liquids at room temperature consisting of a combination of exponentially decaying functions, which extend into the sub- and terahertz frequency range [1,33].

1.4 Quality factor

The quality factor is the total energy stored in a resonator multiplied by the angular frequency over the average dissipating energy in the resonator. Detailed explanations are in [1]. There are three different Q-factor types to distinguish: Q_L, Q_U and Q_{ext} which are the loaded Q-factor, the intrinsic or also called unloaded Q-factor and the

external Q-factor. They are linked as following [1,37]:

$$\frac{1}{Q_L} = \frac{1}{Q_U} + \frac{1}{Q_{ext}} \tag{1.11}$$

To compare different sensors, always the Q-factor of the whole system is essential, which is the Q_L. The loaded Q is calculated from the transmission S_{21} of the scattering parameter as following [37]:

$$Q_L = \frac{f_r}{BW_{-3dB}} \tag{1.12}$$

f_r is the frequency of the transmission peak which is the resonance frequency for the resonators presented, and BW_{-3dB} is the $3\,\mathrm{dB}$ bandwidth related to the transmission peak.

The unloaded Q is also calculated from the transmission S_{21} of the scattering parameter as following [37]:

$$Q_U = \frac{Q_L}{1 - 10^{\frac{S_{21}dB}{20}}} \tag{1.13}$$

Chapter 2

State of the art: sensing and electromagnetic spectroscopy

There are criteria to distinguish and compare different methods of spectroscopy of liquids and particles in liquid: The first thing to distinguish is the LUT in the open as [38] or closed system. Can the measurement be done in flow or not? Is it a resonant or non-resonant system [1]? Is it a wave reflection or transmission system? The complex permittivity can be determined for some methods by analytic formulas such as the reflection of an open-ended coax cable [39] or measured data-based set methods as Split Ring Resonator (SRR) in [2], by comparing the system impedance [40], or the most accurate by numerical simulation of a 3 Dimensions (3D) model to match a measured dataset [7]. The determinations of the complex permittivity values can be sped up primarily by the simulation matching method using self-created look-up tables.

On the one hand, Hamzah and Abduljabar have already researched and listed many of the different applications of electromagnetic permittivity spectroscopy of LUT and particles in LUT. On the other hand, they also did much research about electromagnetic heating. Their most used application is the SRR for sensing and heating [41,42]. The idea behind their use was also the perturbation theory, and they highlighted the details in their publications. In their Ph.D. theses [41] and [42], they already collected the state of the art of liquid and particle sensing and heating until their publication years 2016 and 2017. Their work does not need to be repeated; just essential concepts are explained for understanding, and ones that are interesting for comparison are pointed out and explained. Also, affiliated publications beyond 2017 are added to the state of the art.

At first, it is to determine what spectroscopy is. Spectroscopy is a group of physical methods that decompose or analyze radiation according to a particular property. The most important properties are wavelength, energy, and mass. The intensity distribution that occurs is called the spectrum. At microwave and mm-waves, spectroscopy is an

analytical method investigating the interactions between electromagnetic radiation and the MUT [43].

2.1 Broadbands methods

First, the broadband methods are presented.

2.1.1 Over-the-air or -medium methods

A method with two conical horn antennas, two dielectric lenses for focusing, and a MUT in the middle is presented in [44]. Measuring mixture changes with transmitting and receiving antennas is explained in [45]. A method with a monopole is presented in [46].

2.1.2 Transmissionline methods

Another broadband method is dielectric spectroscopy with transmission lines. Therefore, the liquid is dropped or channeled through the E-field of a transmission line. These lines often have a capacity gap in which the tube filled with sometimes exchangeable LUT is placed and is capacity loaded for higher sensitivity. A line can be a simple microstrip line as in [47] or also a coplanar waveguide (CPW) as in [48] or [49].

2.1.3 Reflect methods

The typical reflect method uses an open coax cable for solids and liquids in [39]. The open-ending coaxial cable is positioned in the LUT or on the solid MUT, and the permittivity is calculated by the from the MUT reflected signal.

Another way is with a microwave horn as presented in [50]. Again the permittivity is calculated by the reflected signal.

2.2 Resonant methods

There are two types of resonances: non-transmission resonances, such as ring resonators and sphere resonators, and transmission resonances, as all of the following explained resonator [1]. The first one to start with is the planar resonator.

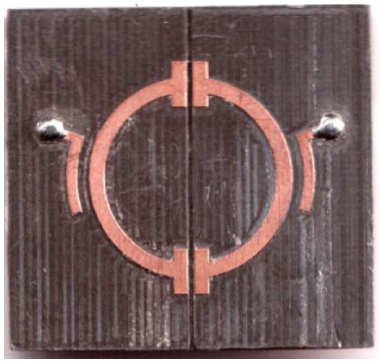

FIGURE 2.1: SRR with double capacity split 3 GHz [2].

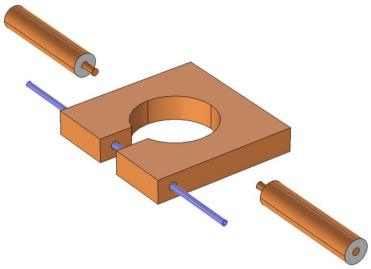

FIGURE 2.2: SRR with a hole through both shanks 2.5 GHz [3].

2.2.1 Planar resonators

Typical planar resonators are MSTLs resonators such as SRR. Hamzah and Abduljabar have already researched the different applications of SRR in the last decade for sensing and heating [51,52]. In Fig. 2.1, a double split MSTL resonator with two series capacitors for sensing is presented.

The electromagnetic signal is parallel capacitively coupled from an open-ended MSTL in the middle of on halve ring of the double split ring resonator. The line width is circa tripled at both splits to increase the capacitive coupling between both SRR halves. The tube with the LUT is placed between both splitting gaps. Therefore the E-field is penetrating the LUT perpendicular and influencing the resonance [2].

A SRR with parallel E-field in the LUT can be seen in Fig. 2.2. The electromagnetic signal is coupled in and out with an open coax cable with an extended inner conductor. The coax is not touching the metal split ring. The split ring has a cut gap on one side. There is a hole through each shank, and the tube with the LUT is placed inside. Therefore, the LUT is tangential to the split ring inner circle. Standard placement of the tube to the inner ring is also possible. It is shown that the parallel placement of the tube with LUT has a more significant influence on the resonance than the perpendicular. The measured volume of the MUT is for both tube directions in the same magnitude [3]. At last, a metamaterials planar resonator is mentioned [53].

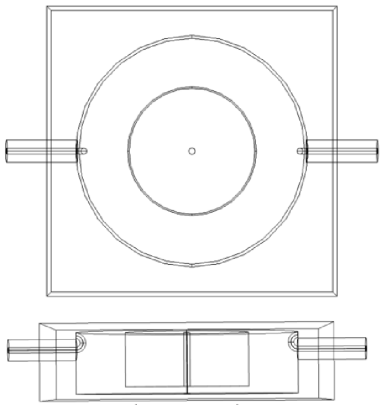

FIGURE 2.3: Re-entrant coaxial cavity resonator 2.4 GHz [4].

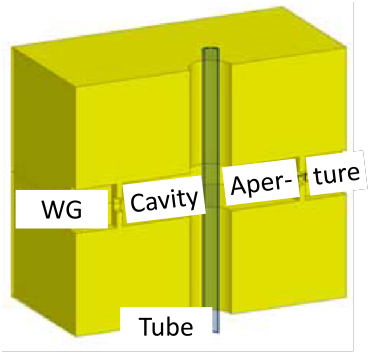

FIGURE 2.4: Cavity resonator at 83 GHz modified after [5].

2.2.2 Cavity resonator

A re-entrant coaxial cavity resonator 2.4 GHz is presented in [4]. See Fig. 2.3. It is a cylindrical metallic coaxial structure closed on all sides. Inner and outer cylinders are connected on one end of the cylinder. Conversely, the inner cylinder is shorter than the outer cylinder. The E-field maximum is in this gap between the shorter inner cylinder and the closed outer cylinder. The tube with the LUT is inside a hole in the middle of the inner cylinder and goes through the entire length of the cylinder in the direction of the cylinder. The E-field penetrates the LUT parallel and detunes the resonance frequency.

In Fig. 2.4 a cavity resonator at 82.5 GHz is presented [5]. The cavity resonator is overmoded to measure the liquid permittivity. The cavity resonator consists of a cylindrical chamber coupled in and out from both sides in the cylinder barrel via rectangular WG with an iris. The tube penetrates the cavity chamber via a hole from the top surface to the bottom surface. For the measurement, different higher modes are used with frequencies of similar magnitudes and compared related to their frequency shift for the LUT and their sensitivity. By measuring the resonant frequency shift caused by the LUT, the MUT permittivity is accurately determined.

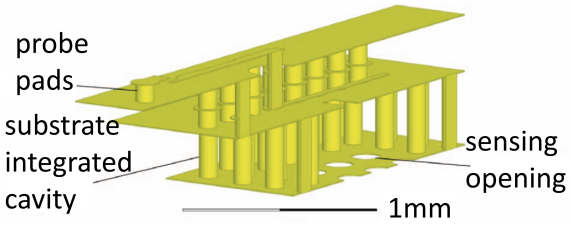

FIGURE 2.5: SIW cavity resonator at 92 GHz adapted after [6].

A unique form of cavity resonator is Substrate-Intergrated Waveguide (SIW) resonator. In SIW, vias, often in different substrate layers built together with metal layers, one or more cavities and WGs used for the resonances and to guide the waves. One SIW which is used to sense LUTs and is working at around 92 GHz is shown in Fig. 2.5 [6]. The SIW cavity is fabricated using (LTCC) technology, which allows for the integration of complex 3D structures and enables high-Q resonators [54]. The signal is guided via probing pads in the substrate-integrated cavity where the LUT is. The LUT is disturbing the resonance modes in the cavity. This disturbing is measured with a similar line method as in [55]. The permittivity of the LUTs and a kind of sensitivity is determined with this measurement. This sensitivity is used to compare this sensor with similar sensors.

2.2.3 Fabry-Perot

A Fabry-Perot resonator is an open resonator that consists of two opposite metal mirror plates. The shape of both mirrors can be plane or, most-time, parabolic. The MUT is positioned in the middle between the plates and in the focal point of the parabolic mirrors. The focal point is the highest E-field and, therefore, the most sensitive point [56]. A Fabry-Perot resonator is presented in [57] to detect water vapor at low levels.

2.2.4 Dielectric resonator

The last resonators to present are DR. DR has a significant advantage over other resonators from this chapter, especially at mm-wave and higher frequencies, to have less loss and a higher Q-factor. The reason is the ohmic metal loss. The DRs have most of their energy in free space around the dielectric or inside the low-loss dielectric and less inside metal parts. Therefore, DRs are affected less than the other resonators.

The Whispering-Gallery-Mode (WGM) resonator is a special dielectric resonator. They work with completely open boundaries, so no ohmic metal loss exists. A WGM

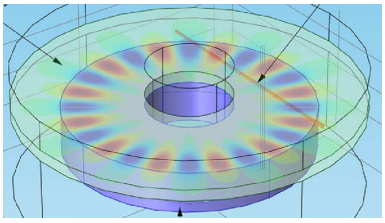

FIGURE 2.6: WGM resonator based on a sapphire disk 35 GHz with a tube inside [7]; the red and blue fields display the maxima and minima of the electric field.

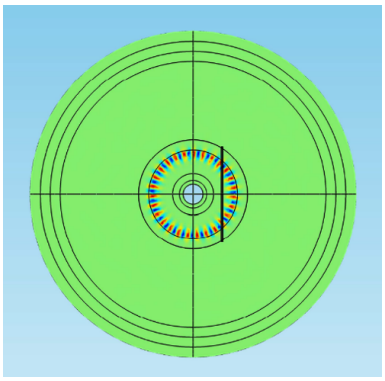

FIGURE 2.7: WGM resonator based on a quartz disk 167 GHz with a tube inside [8]; the red and blue fields display the maxima and minima of the electric field.

resonator working with a sapphire disk at 35 GHz is presented in [7] and shown in Fig. 2.6. A low-loss dielectric layer carrying the LUT in a channel is stacked on the sapphire disk. The signal is coupled in and out of the disk with two opposite dielectric waveguides passing by. The microfluidic channel is a tunnel in the plastic layer tangential positioned in the outer third party related to the disk diameter. In the disk are twelve maxima of the E-field. This is the gallery whispering. The LUT crosses by a few of these maxima, influencing the resonance. The E-field penetrates the sensed LUT from all kinds of directions. The whole disk tunnel is part of the sensing region. This increases the needed volume of liquid.

Another WGM resonator working with a quartz resonator is presented in [8]. The significant advantage and, therefore, why WGM resonators widely investigated in literature is their Q-factor, which is higher than any other dielectric resonator mode as transverse and hybrid: TE, TM, HEM modes. Nevertheless, in addition to being extremely susceptible to geometric variations, the significant confinement of the circumferential field leads to minimal or dispersed interference in the MUT, which ultimately restricts the ability to detect small amounts of LUT. An option to handle this problem and still be able to characterize the MUT is by increasing the volume of the MUT unregarded the influence on the sensitivity. This can be done for gas spectroscopy [58] and solid MUT [59]. The motivation idea in this work is to

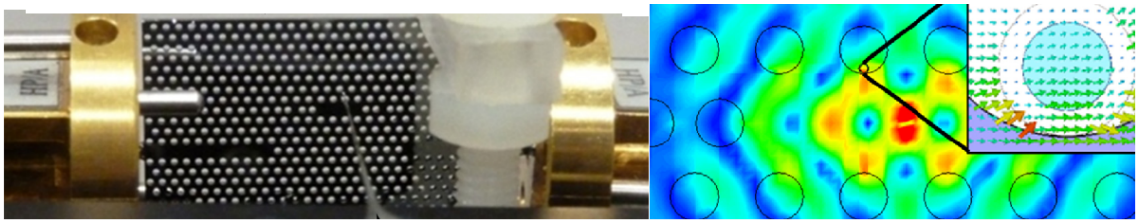

FIGURE 2.8: Photonic crystal defect resonator 100 GHz [9]. Left: LUT measurement setup. Right: E-field simulation.

be possible to characterize fluids and particles in cell size/volume or to distinguish particles. Therefore WGM is not the right solution.

Another dielectric resonator type is the photonic crystal defect resonator. A photonic crystal defect resonator at 100 GHz is the resonator based on a perforated high-resistivity silicon slab in Fig. 2.8 [9]. This crystal resonator was produced in the same way as described in [60]. Ion etching of a hexagonal lattice of holes produces the slab-type photonic crystal out of a silicon substrate. To produce a bandgap for TE-like modes centered at 112 GHz with a 26% fractional bandwidth, the lattice constant and hole radius were chosen in a matching size. The omission of three consecutive holes is a defect in the spatial periodicity of the photonic crystal and creates a resonant cavity in the center of the crystal. The signal is fed and received via facing WR10 WGs. The change from the resonator in [60] to the sensor in [9] is also the quartz tube, which is stuck through the hole in the crystal close to the resonator cavity. The closer the tube is placed to the resonator cavity, the more influence it has because of the more substantial field in and around this resonator part. This can be seen in the right part of Fig. 2.8. With the perturbation of the field and, therefore, of the resonance, the permittivity of the LUT is determined. The permittivity is determined analytically by comparison of the measured resonance frequency and Q-factor of the LUT within the same cycle measured liquids with known values. Also, it is shown in the right part of Fig. 2.8 that the E-field penetrates the tube and LUT perpendicular in the crystal. This perpendicular penetration also decreases the needed volume of liquid for sensing and increases the sensitivity.

A less voluminous and sophisticated dielectric resonator is the SDR. In this thesis, variations of the SDR from Fig. 2.9 are used [10]. In Fig. 2.9 three dielectric alumina ceramic spheres are sandwiched between a thin-film chip and a top metal plate and fed with MSTLs. The resonators in this thesis use just one and two dielectric alumina ceramic spheres with diameters depending on the wanted resonance frequency and fed by various feeding structures. With these setups, resonator modes, which have a magnetic symmetry plane parallel to the sandwiching plates, are used to prohibit

FIGURE 2.9: SDR with three between chip and metal cover sandwiched alumina ceramic spheres at $65\,\mathrm{GHz}$ [10].

leakage in the fundamental (TEM) parallel-plate mode [10]. The signal is coupled in the spheres from a MSTL or strongly coupled from a planar MSTL patch and out on the opposite side. Different modes are generated and create the filter characteristic. The main applications that will be highlighted in this thesis are from [11], [12], and [25].

2.3 Cells and micro-particle measurements

The giant cells in the human body are the egg cells of females. These cells have a diameter of $100\,\mu\mathrm{m}$ and therefore a volume of around $0.5\,\mathrm{nl}$ considering a spherical shape [61]. The smaller cells in the human body are the red and white blood cells called erythrocyte and leukocyte with $7\,\mu\mathrm{m}$ to $8\,\mu\mathrm{m}$ and $10\,\mu\mathrm{m}$ to $30\,\mu\mathrm{m}$ diameter [62]. This is a volume between $0.000\,18\,\mathrm{nl}$ and $0.014\,\mathrm{nl}$.

A work that illustrates how the growth of cells, especially yeast culture, can be measured at mm-waves is presented in [63]. A planar edge-coupled resonator is used at $124\,\mathrm{GHz}$ and changed to $125\,\mathrm{GHz}$ after 24 hours of yeast culture growing. How much influence the yeast cell sizes and amount have and how much the yeast produced ethanol influence is not distinguished. Nevertheless, this work gives good insights into how cell culture growth can be measured by simple means with a tube with a diameter of $500\,\mu\mathrm{m}$ [63]. The standard way cell suspensions are measured is presented in [55]. There are yeast cell suspensions measured with a Coplanar Waveguide (CPW) sensor. A way to measure cells and beads in-flow with impedance spectroscopy is presented in [64].

One of the most sensitive sensors for beads detection with microwave is presented in [65]. Polystyrene microspheres in water with the size of $15\,\mu\mathrm{m}$ and $25\,\mu\mathrm{m}$ diameter are recorded with a SRR. In [66], a microfabricated cytometer working with impedance spectroscopy is presented. Raman spectroscopy with laser light for measuring single cells is presented in [67]. In [68], an interdigitated CPW capacitance is used for sensing. Hordes of dead and alive cells are channeled in liquid over the capacitance and

sensed there. A pioneer in characterizing living tumor cell suspensions at microwave frequency is Grenier [69]. In [70], there is already a comprehensive analysis of the state of the art of spectroscopy of cell suspensions.

The alternative to measuring in-flow is by trapping cells and particles. Mechanical trapping of particles in flow with funnel traps at THz frequency is presented in [71–74]. Electrical trapping, for example, dielectrophoresis, is presented in [75].

2.4 Temperature influence on the measurements

Abduljabar explains in detail and with equations in his Ph.D. thesis [52] the influence of the temperature on the measurement of the permittivity of liquids. A temperature change affects the sensor's dimensions and the sensor's permittivity as the MUT permittivities.

The relative dielectric permittivity of a material is changing with its temperature. An essential liquid to carry particle is water. Water decreases its real part of permittivity ϵ_r circa $30\,\%$ during the heating from $0\,^{\circ}\mathrm{C}$ to $60\,^{\circ}\mathrm{C}$ [76]. Therefore, it is essential to keep the LUT and the environment temperature constant or to compensate for the temperature variation.

A solution to measure MUT with changing temperature without affecting the sensor and causing measurement errors of changed dimension is presented in [77]. To handle the difference temperatures of the MUT, a second SRR without MUT is used as a reference to compensate for the temperature change and to determine more accurate complex permittivity values for water and chloroform.

Chapter 3

Spherical dielectric resonator spectroscopy

[1]There are different types of resonators. Dielectric resonators do have some advantages over other resonators regarding spectroscopy. Dielectric resonators do not need full metal boundaries as cavity resonators, predominantly spherical dielectric resonators, can work with metal boundaries only on top and bottom and are not entirely covered with metal. Therefore, inserting liquid in-flow without disturbing the boundaries is easier and avoids Q-factor degradation. As a example a hole in a metal wall which is a boundary for a cavity resonator is degrading the resonator's Q-factor. Note: a choke system that electrically shorts the open hole could also be used with this kind of resonator. The next advantage of SDRs are their stable modes and strong coupling between the resonating sphere and feeding structure as an open-ended MSTL resulting in a sharp transmission Scattering-parameters (S-parameters) peak and, therefore, in a high Q-factor. Most resonators can only sense a volume fraction of lossy liquid, for example, water at $70\,\mathrm{GHz}$ at room temperature. If too much volume is used or the loss is too high, the sensing resonances of a resonator disappear. A small amount means that the inner diameter of the tube is less than 1% of the wavelength. Primarily SDR can be easily implemented in integrated circuits and, therefore, the Spherical Dielectric Resonator Sensor (SDRS).

This chapter starts with the theory for material characterization with the perturbation of a sensor. After that, the setups for characterization of LUT and particles at microwave are explained and evaluated. Then, follow the setups at mm-wave frequencies. Ultimately, the importance of temperature control and ways to improve accuracy are shown.

[1]The content of this section refers to the papers [11, 12].

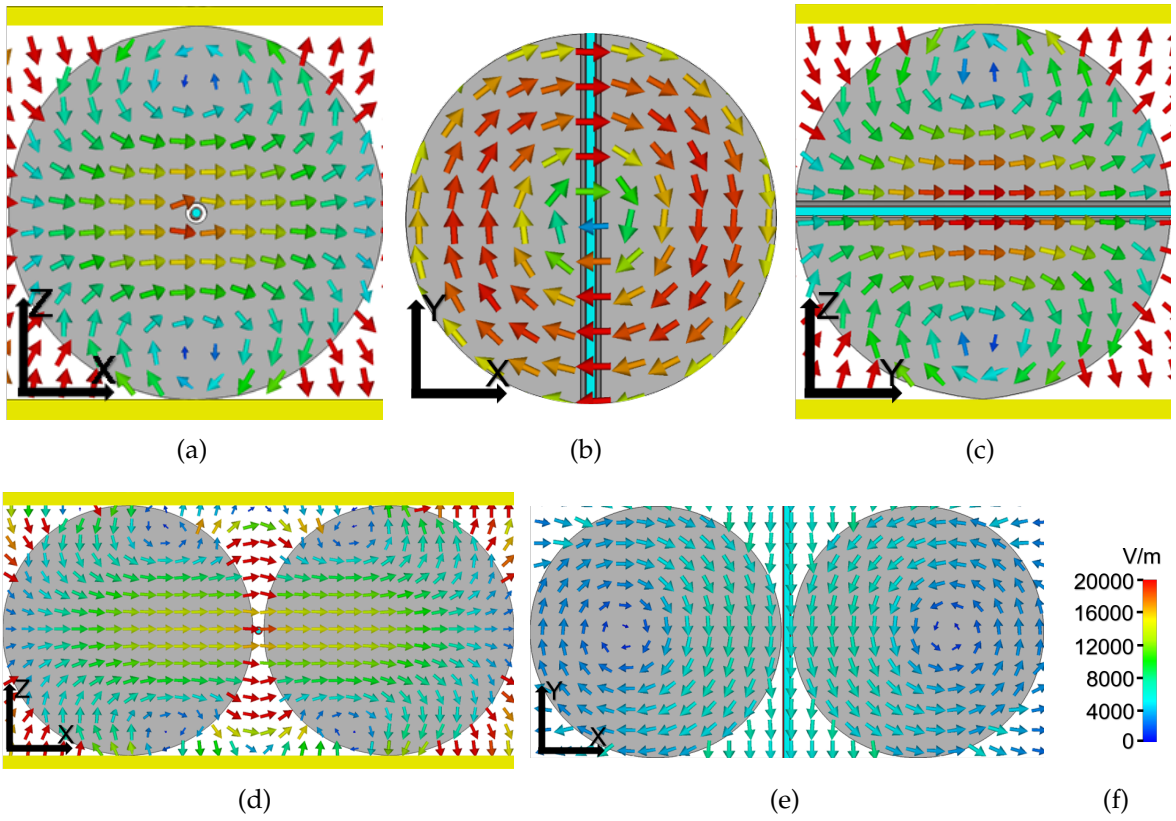

(a) (b) (c)

(d) (e) (f)

FIGURE 3.1: Modes of SDRs with one or two spheres and their E-field maximum penetrating the tube and the various liquids inside. (a) TE^{Y}_{112}; (b) TM_{211}; (c) TE^{X}_{112}; (d) TE_{112}; (e) TM_{101}; (f) E-field scale.

3.1 Theory about fields, modes, perturbation positions, and sensitivity

Every E-field penetrating a material is influenced by this material. Therefore, to increase the material's influence on the field it is necessary to focus the E-field in this material. This can be done by using resonant modes and not just propagating waves. These modes should have as much E-field strength in the material as possible to experience the strongest perturbation of the mode.

Every resonator stimulates different modes. The goal is to have the highest sensitivity, use as little MUT as possible, and find a mode with a single E-field maximum which has to penetrate the MUT. This work uses spherical dielectric resonators with a single dielectric sphere, a drilled hole for the tube, and paired solid dielectric spheres. In Fig. 3.1 resonant modes with their E-field maximum penetrating the tube and the various liquids inside are shown. The tube is always orientated in the y-direction for every setup. The modes are counted based on [78].

The modes are distinguished whether their E-field penetrates the MUT perpendicular or parallel to the tube. The perpendicular modes from Fig. 3.1(a), 3.1(b), and 3.1(d) are more sensitive for changes at low permittivity values of the MUT and therefore for mm-wave sensing. The modes in Fig. 3.1(c) and Fig. 3.1(e) are more suitable to sense changes at high permittivity values and, therefore, for microwaves and lower frequencies [11].

In order to be able to compare the sensitivity of different sensors, the sensitivity has to be defined in the way that sensors working with different volumes, MUTs, and frequencies are comparable. The sensitivity S is defined in (3.1) as in [11] to compare and evaluate different resonators. The resonator distinguishes in: the resonance frequency, the volume of the MUTs, and the permittivity of the MUT, which depends on the material itself, the temperature, the pressure, the frequency, and sometimes the orientation of field penetration. In this thesis, the MUTs are liquids and particles in liquids at normal air pressure.

$$S = \frac{(\Delta f_r / f_r)}{V/\lambda^3} \cdot \frac{1}{\epsilon_r - 1} \tag{3.1}$$

The normalized volume (V/λ^3) is the volume of the "active" MUT in relation to the free space wavelength at the resonance frequency. The relative resonance frequency shift ($\Delta f_r / f_r$) is from no MUT, which is an empty tube in this thesis, to a MUT filled tube. ($\epsilon_r - 1$) is the permittivity change from no MUT to the MUT. Active volume is the volume exposed to the resonator's electric field, influencing the resonance. Which volume active is, is vague because of the open conditions by the dielectric resonator. It can be seen in (3.1) that the sensitivity of a resonator increases if the relative resonance frequency shift increases or the relative volume or permittivity difference decreases.

To determine the complex permittivity of the MUT as already mentioned in chapter 2, the 3D simulation model is matched to the measured data. In this work, the software CST Microwave Studio mainly with finite-element working frequency solver, is used for the full-wave simulations.

3.2 Microwave-Measurement: Spectroscopy of MUT

In this thesis[2], as already mentioned in section 3.1 single alumina Al_2O_3 spheres with a drilled hole and the MUT in the hole and dual-coupled solid $18\,\mathrm{mm}$ diameter spheres with the MUT in the gap between the spheres are used. The MUT is investigated with different orientated E-fields. Standard $99.9\,\%$ pure Al_2O_3 has a $\epsilon_r \approx 9$ to 11

[2]This section is from [11]

and $\tan\Delta \approx 10^{-5}$ to 10^{-3} in the microwave and mm-wave range [79]. At first, the construction is described, and then the simulation and measurement results are shown and evaluated.

The modes from Fig. 3.1(c) TE^{X}_{112}, Fig. 3.1(d) TE_{112}, Fig. 3.1(e) TM_{101}, were chosen for sensing because they have more frequency shift caused by MUT than Fig. 3.1(a) TE^{Y}_{112} and Fig. 3.1(b) TM_{211} as simulations and measurements show. Different feeds, as can be seen in Fig. 3.2, are chosen to stimulate the wanted modes. The fringing fields of the opposite open-ended MSTLs as in Fig. 3.2(a) and Fig. 3.2(b) excite strong straight coupling modes such as the modes in Fig. 3.1(a), Fig. 3.1(c) and Fig. 3.1(d) and weaker other modes. However, the parallel open-ended MSTL as in Fig. 3.2(c) excites a strong rotating mode such as in Fig. 3.1(b) and Fig. 3.1(d). The setup in Fig. 3.2(a) is named Setup 1, in Fig. 3.2(b) and Fig. 3.2(c) is named Setup 2 and Setup 3.

In Setup 1, the sphere has an ultrasonic through the center drilled hole with a $1\,\mathrm{mm}$ diameter hole in the $18\,\mathrm{mm}$ ceramic sphere. In the hole is the LUT carrying tube. In Setups 2 and 3, the tube is placed between the ceramic spheres.

In this work, LUTs and LUTs with particles are the MUT. Therefore an empty tube, through which the different LUTs are pumped, is placed in the E-field maxima of the resonator. These tubes are PolyTetraFluoroEthylene (PTFE) and silicon glass tubes because of the low electromagnetic loss and availability in mm and μm diameters.

The sketches of a SDR with a single sphere are shown in Fig. 3.3. In Fig. 3.3(a), the feeding to excite a stronger rotating mode is shown, in Fig. 3.3(b) the feeding to excite a stronger direct straight coupling. The setup from Fig. 3.3(b) is more sensitive to the MUT in the drilled hole of the sphere than Fig. 3.3(a) because of the single maximum in the MUT and therefore is used in this work. Both types of feeding are used for the SDRs with two spheres. It should be noted again that the feeding as in Fig. 3.3(a) is more sensitive for extremely high permittivity materials.

In the thin boards, holes were drilled to align in relation to the excitation feed and to hold the spheres. The drilled holes are illustrated in Fig. 3.3 with the rectangular crates under the sphere. The thin board is made of Rogers RO3003 with a thickness of $0.254\,\mathrm{mm}$ and $\epsilon_r = 3.0$. The board is stacked on a $1\,\mathrm{mm}$ copper plate for stability and as another ground plane with a metal wall and boundary under the sphere.

On the end of the MSTLs of Setup 1, 2, and 3 are board-edge coax connectors soldered. These connectors are linked to a network analyzer. The tube and the inserted LUT, the MUT, are pitched over Rohacell foam blocks.

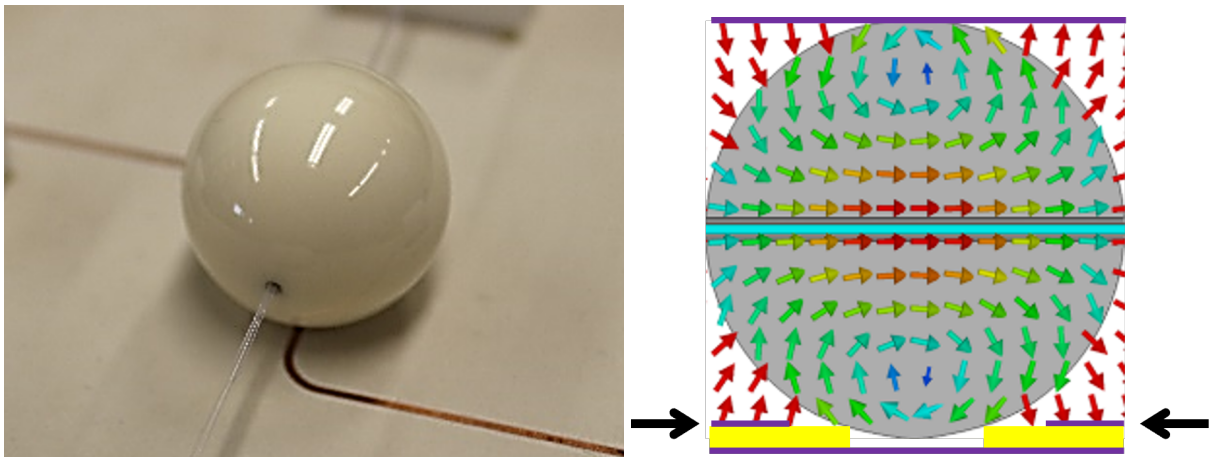

(a)

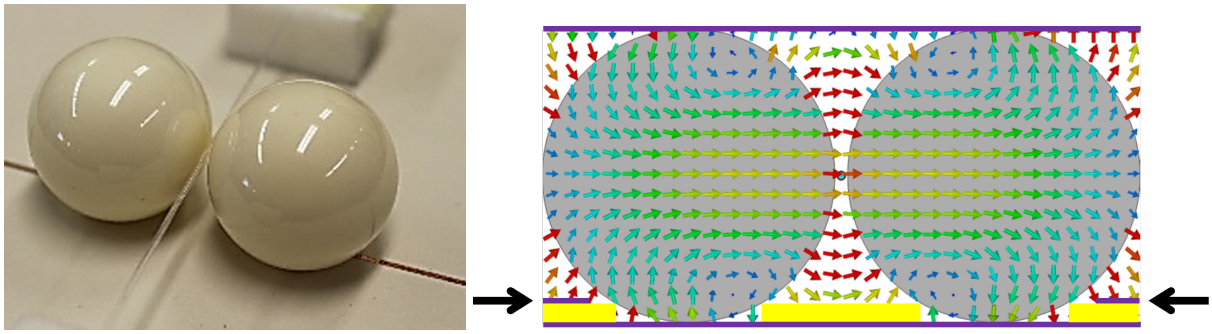

(b)

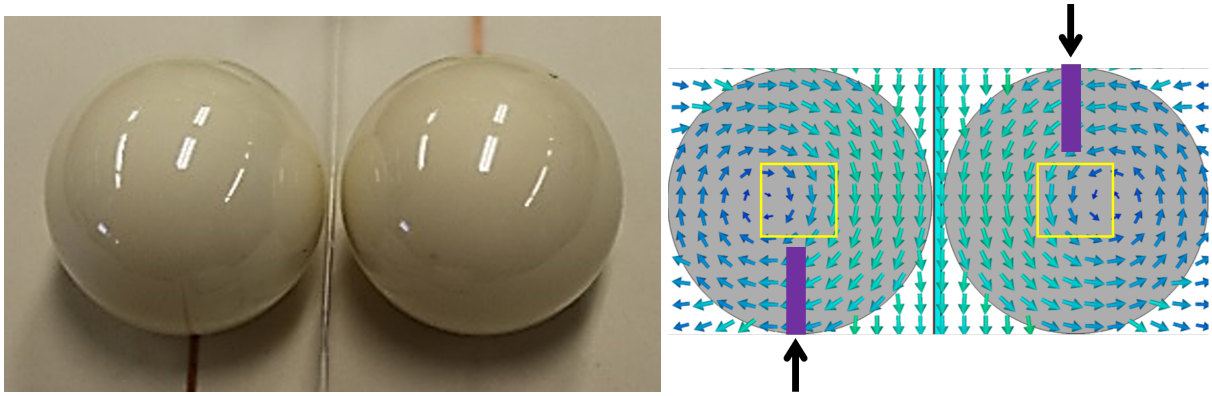

(c)

FIGURE 3.2: Microwave measurement setups (left) with E-field vector plots from Fig. 3.1 of corresponding modes (right). The covering top metal plate is removed for the pictures. The black arrows point out the feed ports. The violet inner and surrounding lines are MSTL feed lines with ground plane and the sphere sandwiching metal cover. The yellow surfaces are the substrate [11]. (a) Setup 1: single sphere with hole and tube inside. (b) Setup 2: two coupled spheres with feed lines perpendicular to the tube in between. (c) Setup 3: two coupled spheres with feed lines parallel to the tube in between. The yellow squares show the crates in which the spheres lie.

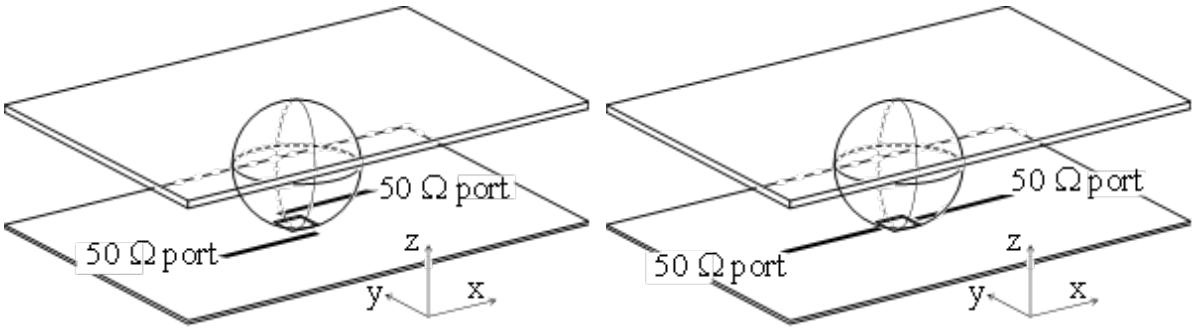

(a) (b)

FIGURE 3.3: Concept sketches of SDR with one dielectric sphere and different positions of open-ended MSTL as feeds. [11]. (a) feed position to excite stronger modes with rotating E-field. (b) feed position to excite stronger modes with a straight E-field through the center of the dielectric resonator.

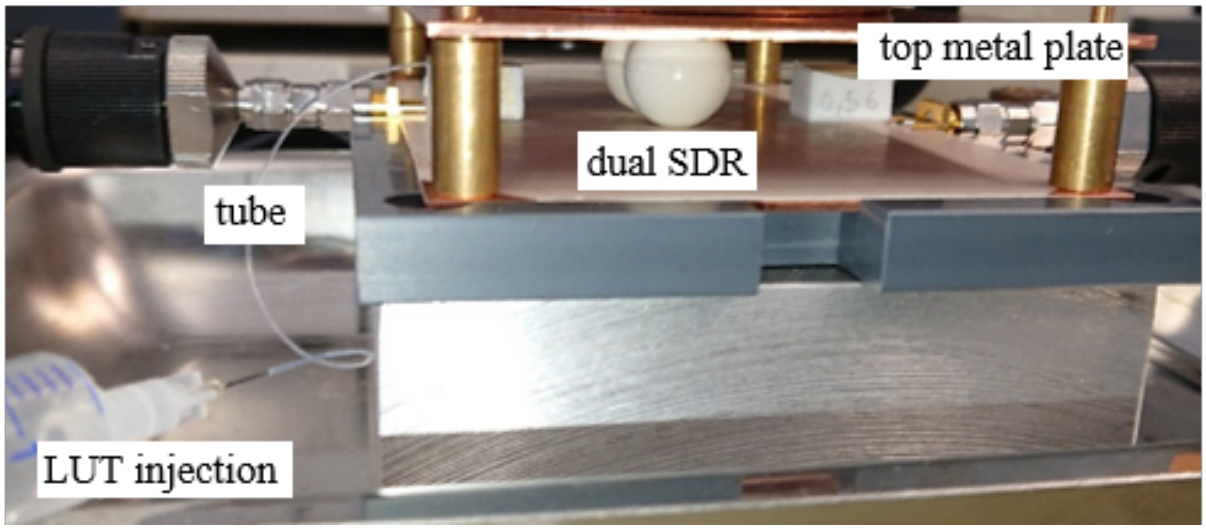

FIGURE 3.4: Measurement setup at microwaves with 18 mm diameter spheres [11].

3.2.1 Setup assembling for measurement and implementation instructions

All setups are assembled in the same way. Their circuit boards are the same sizes and fit in the holding constructions, as seen in Fig. 3.4. The central part is a stack of a heavy metal block, which gives stability and prevents slipping; the plastic holder is glued on the metal block, in which the circuit boards with their extra copper ground plane are embedded. The edges of the circuit boards and ground planes are drilled holes, and the corresponding holes with threads are in the plastic pieces. Brass cylindrical pillars with screws on one side are driven in the plastic piece to fix them and prevent the circuit board from moving. The alumina spheres are placed in the

drilled crates in the middle. In Fig. 3.4 is Setup 3 from Fig. 3.2(c) and there are two alumina spheres. The spheres are sandwiched between the circuit board and a top copper plate. The top metal plate also has holes in the corners and is stacked on up pins, an extension of the cylindrical pillars. This holds the top cover in position. To extend the SDR to an SDRS, also MUT has to be placed in the resonator. Therefore, Rohacell bricks with a channel on top are glued in cutouts of the circuit. The PTFE tube is stretched between the spheres held at both sides from white Rohacell bricks and aligned and glued in the channels with tape. Rohacell is a high-strength, CFC-free hard foam, and the in this work used type has nearly the same permittivity as air even at mm-waves [80].

There were a few improvements and changes tried little by little to get more accurate results or to solve unwanted occurrences: The first big problem is air bubbles. Air bubbles are an extremely disturbing factor because they distort the measurement completely. Big bubbles are noticed more easily than small ones because the resonance frequency shifts extreme to a higher frequency, sometimes the same as for an empty tube. Tiny bubbles do not get noticed. There will be just the feeling that something is wrong with the LUT, maybe some type of mix or liquid. The temperature change during the measurement should be kept small to avoid bubbles. Also, before linking the syringe to the tube, the syringe pump should be held with the syringe upwards and pumped until there is no air anymore in the syringe pump and liquid leaks out. Also, after one LUT is measured, there are two options. The LUT remaining in the tube can be sucked back or tried to blow out entirely with an air-filled syringe pump. Both ways are working. The following LUT is pumped through the tube after this, and the first parts of the liquid should be entirely pumped through and collected in a cup to have a clean LUT in the active region and not a mix. The open end of the tube should be placed over the cup and in the air and not in the liquid in the cup to avoid the liquid being sucked back into the tube from the cup.

It was also noted that the PTFE tube changed its diameter because of the inner pressure caused by the pumping. The position of the active tube part also changed with liquid pressure when the tube was tensed a long way between the spheres. The reason was the insufficient taut tension and the kinks that straighten oneself. Both reduced the accuracy of the measurement. Later the PTFE was replaced by a quartz glass tube where possible. Glass does not have this problem, but they have the disadvantage of being breakable.

Another wish is to open and close the top cover plate to check if there are any bubbles in the active region if the position has changed from the tube or for particle spectroscopy to check if the particle is in the middle. The problem is that now, during

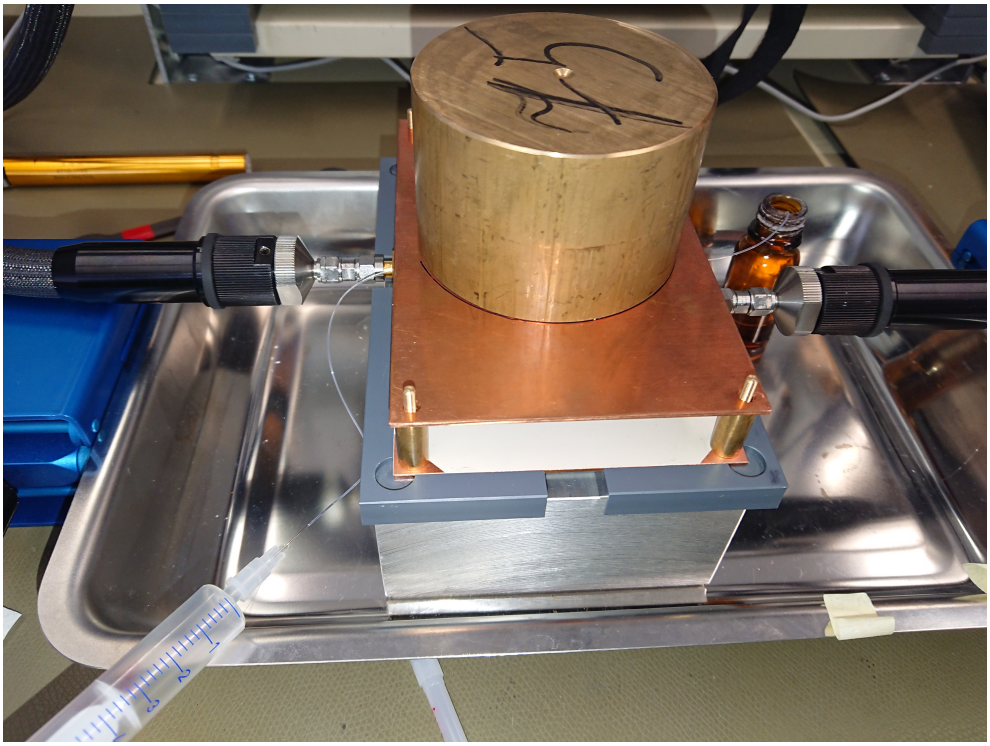

FIGURE 3.5: Photo of microwave SDR closed with weight on top and connected syringe pump and cables.

each opening, the spheres always moved slightly in their position or orientation. This caused a detuning of the resonator. The reason is that the spheres are not perfectly spherical, and the material is not homogeneous. Therefore, spheres have an orientation which means they are anisotropic. Now the idea was to be able to have the top plate in a position so that it is not touching the spheres anymore when lifted to avoid side movements of the spheres because of the leeway between wholes and pins. To lift the top plate without touching the spheres, ring spaces were added on the pins between the top plate and the pillars. On top of the top metal plate, a heavy weight was placed to bend down the metal plate so that it touched the spheres. See Fig. 3.5. This worked, but after lifting the weight, removing the plate, and assembling everything back again, the resonance frequency always changed. The transmission measurement results of over 25 openings and closings without any MUT are shown in Fig. 3.6. The absolute frequency shifting range is $0.5\,\mathrm{MHz}$, circa 0.01%. The frequency changed even just by lifting the weight and replacing it in the same position. Maybe with each touching of the sphere, the sphere rotates or is pushed slightly differently, so there is always a different resonance frequency. A solution could be to glue the sphere in the crate to avoid moving and rotation. For the LUT measurements in this thesis, the resonator is not opened during each measurement pass, and any mechanical influences are tried to avoid during measurements.

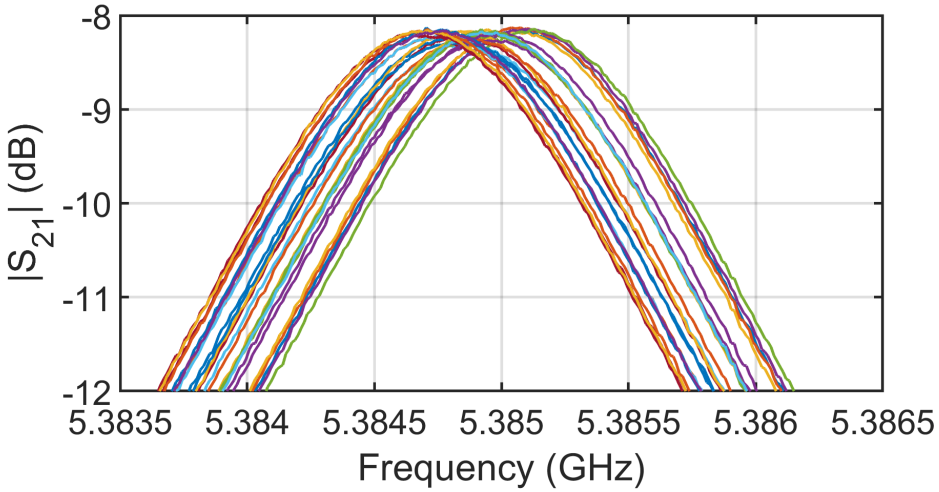

FIGURE 3.6: Transmission measurement results of over 25 openings and closings of Setup 3 without MUT.

At last, the metal plate should always touch the sphere to have the highest Q-factor and get the best sharpest resonance peak and most accurate results. The touching is controlled with the mirror image of the spheres on the bottom side of the top cover, see Fig. 3.7. If the image and the sphere touch, do the sphere and the top cover. How much the influence on the resonance can be seen in Fig. 3.8. At $5.385\,\mathrm{GHz}$, there is the passel of the openings and closings. At $5.372\,\mathrm{GHz}$ and $5.377\,\mathrm{GHz}$, there are the resonance frequencies for measurements without weight and, therefore, measurements of not the spheres touching the metal plate. As less the sphere is touched and the more considerable the distance is, the higher the frequency and lower the sharpness of the peak, which corresponds with the Q-factor.

3.2.2 Spectroscopy of LUT

The layouts of Setup 1, 2, and 3 are shown in Fig. 3.9. The MSTL width is circa $0.55\,\mathrm{mm}$ for all setups and the radius of the holes for the spheres is $2.1\,\mathrm{mm}$. In Fig. 3.9(a) is the distance between both open-ended MSTL $6.5\,\mathrm{mm}$. The distance from the open-ended MSTL to the center of the round crate in Fig. 3.9(b) and Fig. 3.9(c) is $2.5\,\mathrm{mm}$ and $2.8\,\mathrm{mm}$.

The MUT in this chapter are various LUT. The following sample liquids, with various permittivity values, were chosen for the measurements and characterization at frequencies at around $5\,\mathrm{GH}$ to $6\,\mathrm{GHz}$: water, methanol, ethanol, isopropanol (isopropyl alcohol, propane-2-ol, 2-propanol). The reference measurement is with an empty tube, meaning only air is in the tube. The resonators work as a transmission signal filter. The transmission S-parameters are measurements of the resonator for each liquid with

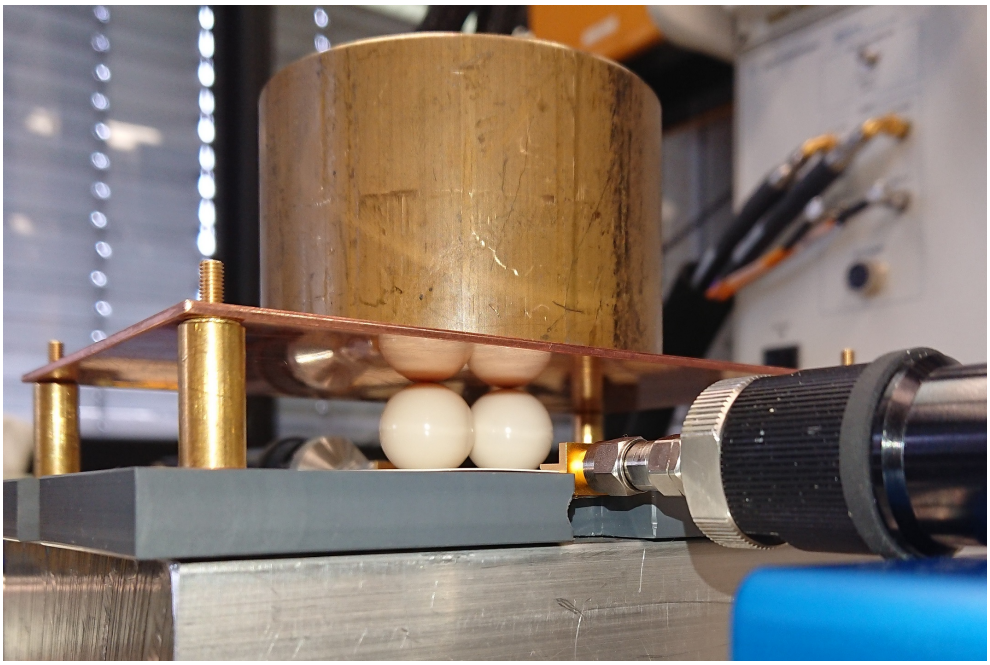

FIGURE 3.7: Resonator with two spheres sandwiched with extra weight on top. On the bottom of the top metal plate are mirror images of the spheres.

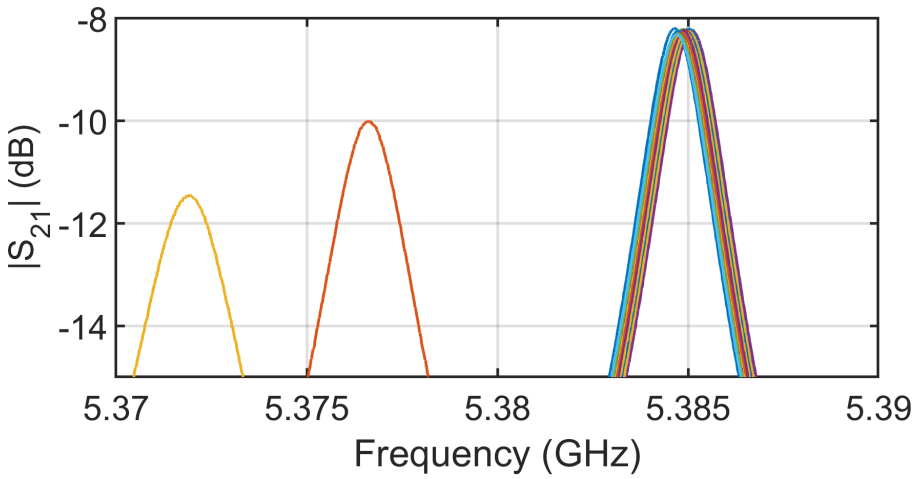

FIGURE 3.8: Transmission measurement results of over 25 openings and closings of Setup 3 without MUT and not well-touching top metal plate.

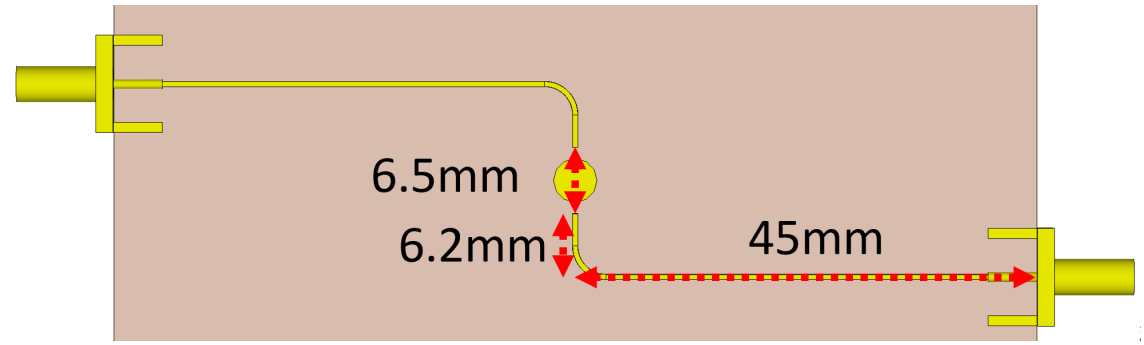

(a)

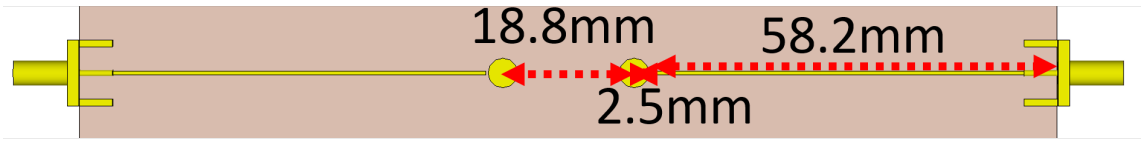

(b)

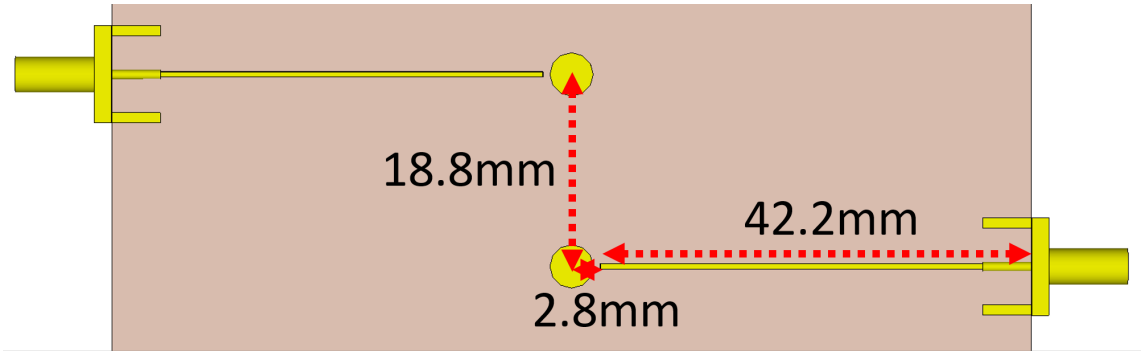

(c)

FIGURE 3.9: Top view of layout with dimensions. SMA connectors are soldered on the MSTLs on each side. (a) Setup 1. (b) Setup 2. (c) Setup 3.

a network analyzer. The resonance maximum peak appears in the transmission at the resonance frequency. For each liquid with different permittivity, there is another resonance peak. The frequency shift comes mainly from the changed real part of the LUT. The shape change as flattening belongs mainly to the imaginary part of the LUT, called dielectric loss [11]. It is also mandatory that the resonator itself has significantly less loss to support the shaping of a sharp resonance peak. A sharp resonance peak also indicates a high Q of the resonator. Less loss does not mean that a strong coupling is needed. A weak coupling of the resonator is working as long as an identifiable resonance peak with a minimum height of $3\,\mathrm{dB}$ appears for the most lossy of the measured liquids.

A PTFE tube with $0.56\,\mathrm{mm}$ outer and $0.4\,\mathrm{mm}$ inner diameter is used to carry the LUT. The LUTs are injected manually by a syringe as shown in Fig. 3.4 and Fig. 3.5. After the measurement, the geometrical details of the CST 3D model are changed until the model simulation matches with the S_{21} transmission measurement data. At first, the model is matched without liquid, and then the LUT is included in this model. The real part of permittivity ϵ_r, and loss tangent $\tan\delta$ in the simulation is optimized until measurement and simulation curves match. These optimized values from the simulation at the resonance frequencies are compared with the values from the literature [2, 76, 81–84], and shown together with the calculated relative error in Table 3.1, Table 3.2 and Table 3.3. The relative error is defined as the difference between the literature value and the calculated value over the middle. As mentioned, water, methanol, ethanol, and isopropanol are used as LUTs.

As described in section 3.2.1, with this measurement and determining method of the real part and loss tangent error which occur because of geometry changing especially during LUT changing are not considered. These are the most significant error causes but are tried to keep in check by measures such as not opening the resonator during the measurement and reducing other movements by fixing everything with tape and glue.

The measurement results for Setup 1, 2, and 3 are shown in Fig. 3.10, Fig. 3.11, Fig. 3.12 together with the curves of the matched simulation models.

The active volume length of the tubes as in section 3.1 mentioned is assumed to be $3/4$ of the sphere diameter for Setup 1 and 2 and two times the sphere diameter for Setup 3. They depend on the E-field mode and focus and were established by simulations so that the error between the active volume length of the tube and an infinitely long tube is less than 1%. With these active volume values, the sensitivity of Setups 1,2 and 3 can be compared with state of the art and seen in Table 3.4 and Table 3.5.

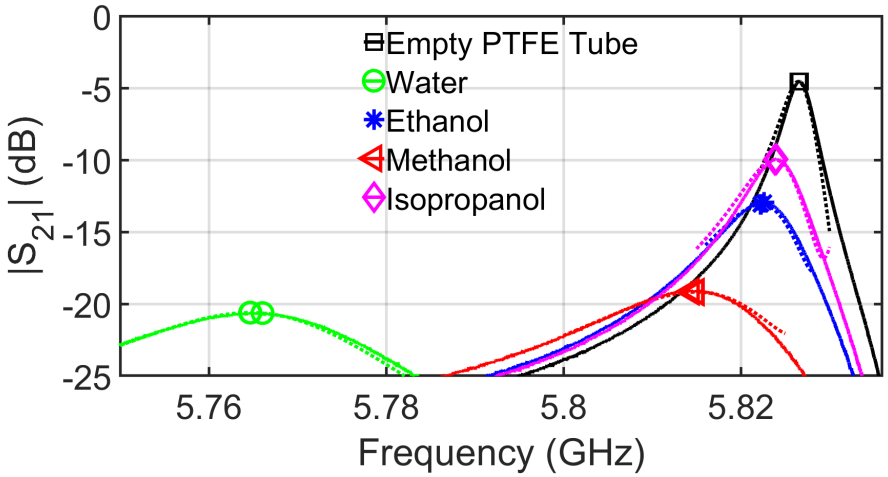

FIGURE 3.10: Measurements (solid) and fitted simulation (dotted) transmission $|S_{21}|$ result of Setup 1 [11].

TABLE 3.1: Calculated permittivity values of the measurement results of the LUT with Setup 1 at 30 °C [11].

LUT	measured f_r (GHz)	textbook (Debye)		fitted in simulation		relative error (%)	
		ϵ_r	$\tan\delta$	ϵ_r	$\tan\delta$	ϵ_r	$\Delta\tan\delta$
water	5.7683	71.9	0.24	71.9	0.22	0	8.7
ethanol	5.8225	5.16	0.75	4.85	0.88	6.2	16
meth.	5.8150	12.4	0.93	11.5	1.10	7.5	17
prop.	5.8240	3.60	0.48	3.5	0.65	2.8	30
air	5.8265	1	0	1	0	–	–

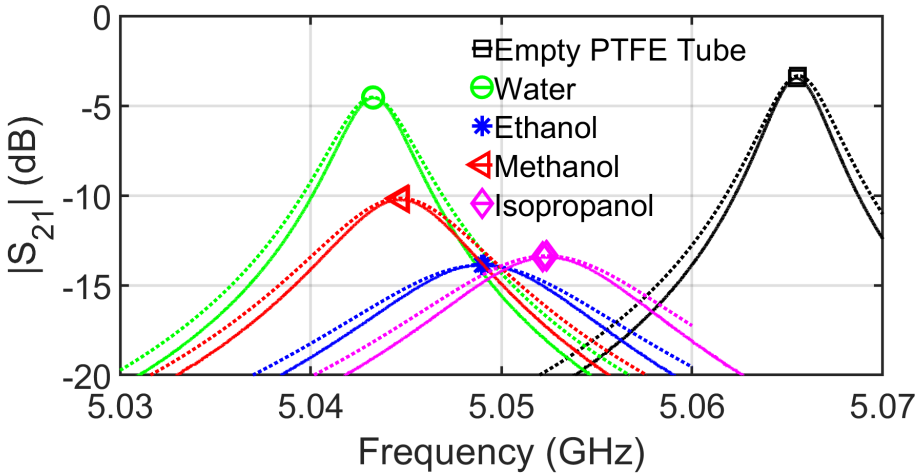

FIGURE 3.11: Measurements (solid) and fitted simulation (dotted) transmission $|S_{21}|$ result of Setup 2 [11].

TABLE 3.2: Calculated permittivity values of the measurement results of the LUT with Setup 2 at 25 °C [11].

LUT	measured f_r (GHz)	textbook (Debye)		fitted in simulation		relative error (%)	
		ϵ_r	$\tan\delta$	ϵ_r	$\tan\delta$	ϵ_r	$\Delta\tan\delta$
water	5.0433	73.7	0.24	65	0.35	13	37
ethanol	5.0491	4.93	0.76	4.6	1.00	6.9	27
meth.	5.0448	12.9	0.93	11.5	1.20	11	25
prop.	5.0524	3.60	0.47	3.6	0.65	0	32
air	5.0656	1	0	1	0	–	–

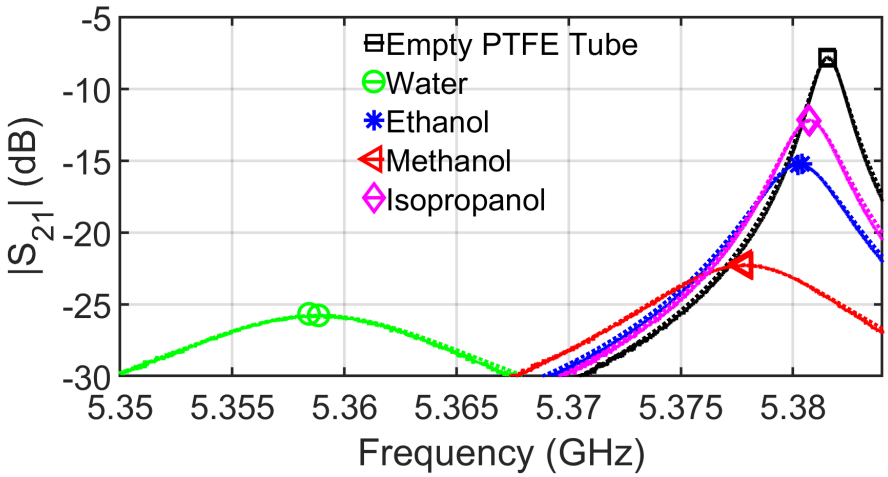

FIGURE 3.12: Measurements (solid) and fitted simulation (dotted) transmission $|S_{21}|$ result of Setup 3 [11].

TABLE 3.3: Calculated permittivity values of the measurement results of the LUT with Setup 3 at 25 °C [11].

LUT	measured f_r (GHz)	textbook (Debye)		fitted in simulation		relative error (%)	
		ϵ_r	$\tan\delta$	ϵ_r	$\tan\delta$	ϵ_r	$\Delta\tan\delta$
water	5.3588	73.1	0.26	72	0.26	1.5	0
ethanol	5.3804	4.82	0.73	5.3	0.79	9.5	7.9
meth.	5.3778	12.3	0.95	13.3	0.91	7.8	4.3
prop.	5.3808	3.58	0.45	3.6	0.52	0.6	14
air	5.3815	1	0	1	0	–	–

TABLE 3.4: Sensitivity comparison for microwaves and low permittivity [11].

setup	E-field direction	f_r (GHz)	ϵ_r	active length (mm)	active volume (μl)	sensitivity S
[4]	$\parallel$	2.43	4.7	1	0.13	1680
[2]	$\perp$	3.07	4.7	9	0.16	16950
[3]	$\parallel$	2.52	4.7	3	0.38	1430
1	$\parallel$	5.82	3.5	13.5	1.7	14
2	$\perp$	5.05	3.6	13.5	1.7	123
3	$\parallel$	5.38	3.6	36	4.5	2.3

TABLE 3.5: Sensitivity comparison for microwaves and high permittivity [11].

setup	E-field direction	f_r (GHz)	ϵ_r	active length (mm)	active volume (μl)	sensitivity S
[4]	$\parallel$	2.42	77.2	1	0.13	894
[2]	$\perp$	3.04	76.6	9	0.16	1490
[3]	$\parallel$	2.47	77.2	3	0.38	1340
1	$\parallel$	5.77	71.9	13.5	1.7	11
2	$\perp$	5.04	65	13.5	1.7	8.4
3	$\parallel$	5.36	72	36	4.5	1.9

For the sensors in [2–4], the capacitive gap constitutes the active MUT region. It can be now seen in Table 3.4 and Table 3.5 that for lower and higher permittivity of the LUT, the setups perform differently. For low permittivity (even with high loss), the perpendicular $\perp$ through the LUT coupling sensors are the more sensitive ones. If the permittivity is very high (higher than our samples), the parallel $\parallel$ penetrating sensors are more sensitive at some point. This chapter shows that capacitor-based resonators are especially sensitive at microwave frequencies because of their more concentrated E-field. The section 3.3.2 will show that mm-waves and sub-THz dielectric resonators are the better and more sensitive options because of their high Q-factor. The active length and volume will decrease at sub-THz from mm and μl to μm and nl.

3.2.3 Spectroscopy of single particles in flow in liquids

The first measurements of Particle Under Test (PUT) were done in this work in a PTFE tube. As already mentioned in the LUTs measurements, the PTFE tube expands its cross section with pressure and even more when a sphere in a similar size as the inner diameter is passing by. This expansion changes the volume under test and

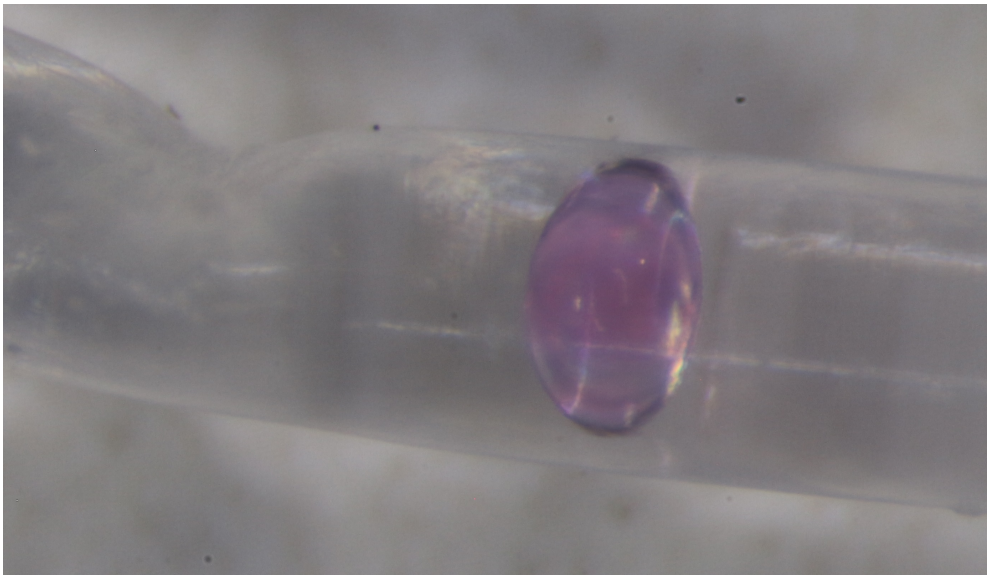

FIGURE 3.13: Ruby sphere in water in-flow inside a PTFE tube with a kink.

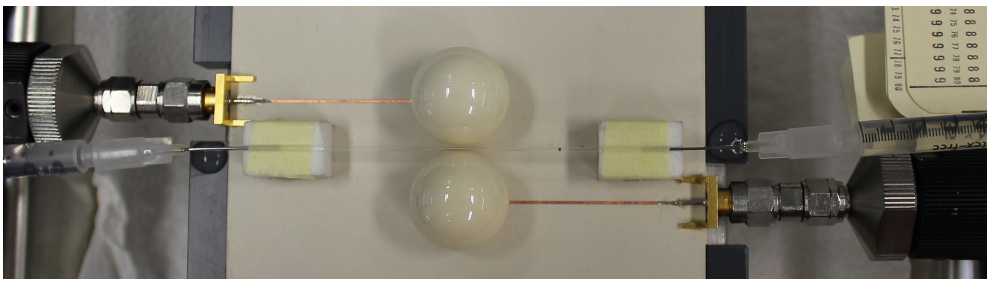

FIGURE 3.14: Microwave setup measurement of a black silicon particle in-flow inside a glass tube filled with water with leaking syringes stuck in.

increases the inaccuracy. Additionally, the PTFE is susceptible to kinks, as shown in Fig. 3.13. Particles in the size range of the inner tube diameter sometimes get stuck at the kinks, or much pressure is needed to pass the particle, which also decreases the accuracy.

Therefore a solid quartz glass tube is used for further particle measurements. The setup with quartz glass and syringes stuck in the solid tube without sealing is shown in Fig. 3.14. The PUT is placed in the glass tube, a syringe stuck in it from both sides and filled from both sides with LUT until there is no air anymore in the tube, and the first drops of the LUT are leaking out on both sides of the tube. Now the sphere is positioned in the middle of the SDRS with the flow of injected liquid, and afterward, the top metal cover is closed. This is now the measurement of the most influence of the particle. After this measurement, the particle is blown to one end of the tube by injecting liquid with one syringe and removed from the active sensing region. This is the contrast measurement, which shows the influence of the particle on the sensor.

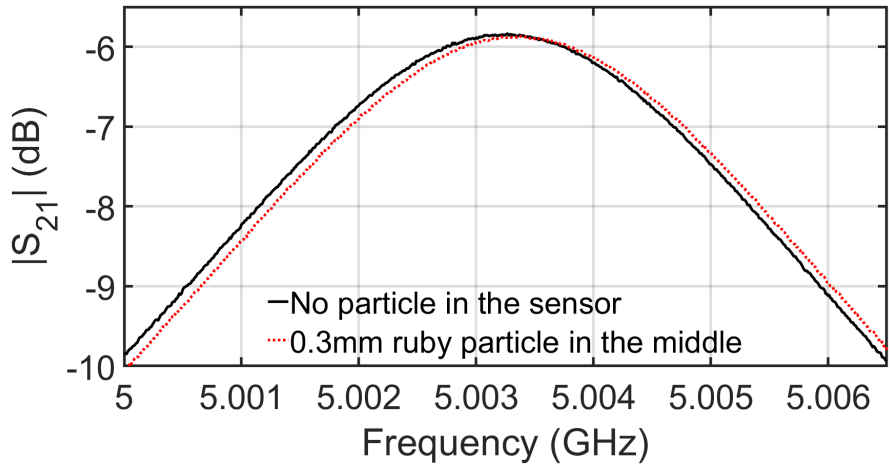

(a) Setup 2: $0.3\,\mathrm{mm}$ ruby particle.

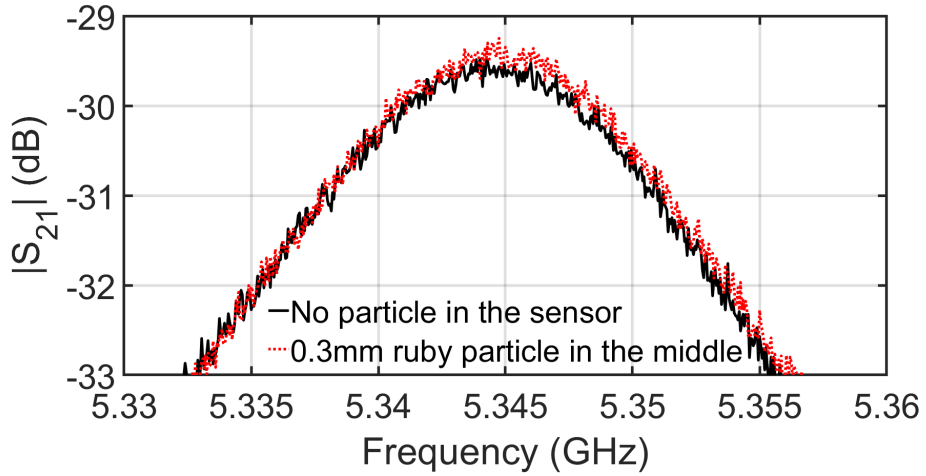

(b) Setup 3: $0.3\,\mathrm{mm}$ ruby particle.

FIGURE 3.15: Transmission measurements of particle in-flow in water in a glass tube at microwaves.

The S-parameters transmission measurement results with Setups 2 and 3 from a $0.3\,\mathrm{mm}$ ruby and a $0.48\,\mathrm{mm}$ silicon particle can be seen in Fig. 3.15 and Fig. 3.16.

As expected, the bigger particle does have a higher influence. Ruby and silicon have a dielectric loss close to zero and relative permittivity of circa 10 and 12, which is very similar compared to the permittivity of water with circa 73 at this frequency and room temperature. Therefore for these measurements, the main influence difference is the volume of the particle. Furthermore, in Fig. 3.15(a) and Fig. 3.15(b), the transmission amplitude with a lossless particle and therefore less volume of lossy water is higher than without a particle. There are other influences than just the loss of the MUT on the transmission amplitude, too, because in Fig. 3.16(a) and Fig. 3.16(b) the amplitude is less although the volume of lossy water is less because of the bigger particles. Also,

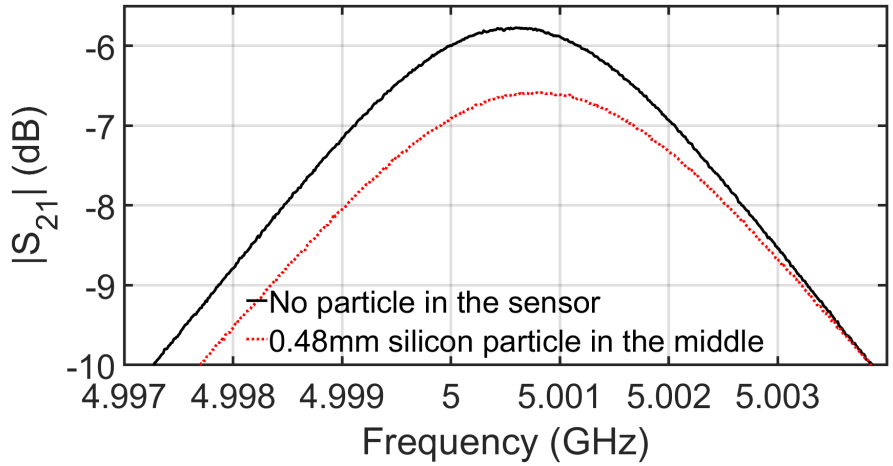

(a) Setup 2: 0.48 mm silicon particle.

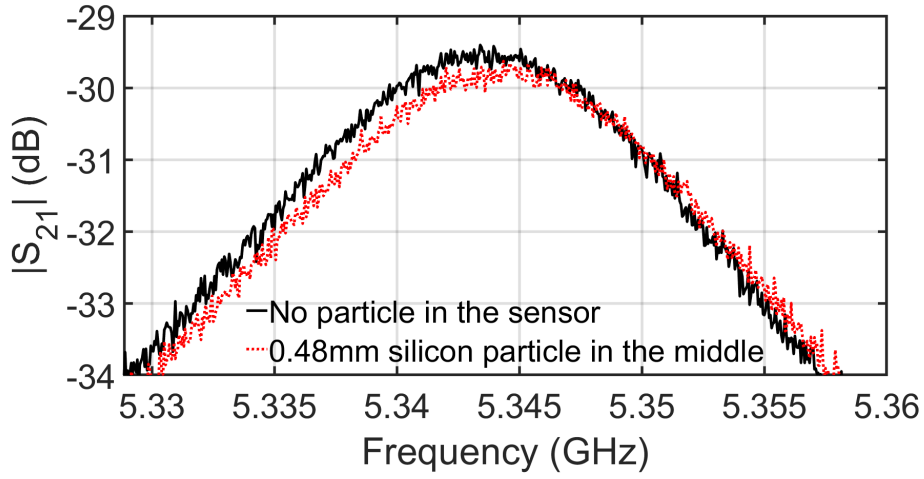

(b) Setup 3: 0.48 mm silicon particle.

FIGURE 3.16: Transmission measurements of silicon particle in-flow in water in a glass tube at microwaves.

there could be some changes in the silicon in the water which results in this not expected behavior of the transmission measurement.

Finally, the comparison of both setups: the resonance frequency changes are for both setups very similar. The amplitude changes are different. Setup 2 has five times more amplitude change than Setup 3 for the silicon particle.

3.3 mm-Wave-Measurement: Spectroscopy of MUT

Compared to the microwave spectrum at lower frequencies, as dealt with in the sections before, spectroscopy for liquids at mm-wave has the benefit of the range of permittivity variation restricted to a relatively low level. Another fact at mm-wave is that metal-based circuits such as ring resonators or coplanar-waveguides and metal full-cavity sensors will suffer because of conduction loss at high frequencies. Using a Vector Network Analyzer (VNA) with a high dynamic range and high sensitivity enables the measurement of lossy MUT under consideration of the MUT's volume, but is still limited. This leads to the limitation problem for on-chip applications, as the comparison in [59] shows. Instead, approaches with dielectric resonators provide more effective solutions at mm-wave and sub-THz frequencies.

The application for the spectroscopy with SDRS at microwaves is explained in the section before. Now follow the applications at mm-waves and sub-THz frequencies, which have even higher sensitivity and need less than fractions of volume as at microwaves for the MUT. In this section, the bottom metal board for sandwiching the spheres is a thin-film circuit board including the feed lines, and the top metal cover is (except for the $30\,\mathrm{GHz}$ setup,) an aluminum metal brick positioned with a micrometer positioner.

At mm-wave, there are four setups for spectroscopy: one is Setup 2 at $30\,\mathrm{GHz}$ for particle and temperature measurements, another setup at around $70\,\mathrm{GHz}$ named Setup 4, and two setups at around $190\,\mathrm{GHz}$ named Setup G1 and Setup G2. Setup 4 is Setup 1 scaled and adapted to circa $70\,\mathrm{GHz}$ and is shown in Fig. 3.17. The used board is a thin-film circuit. The $1.588\,\mathrm{mm}$ alumina sphere is placed on it by hand. The SDR is again fed by opposite open-ended MSTLs connected with the network analyzer through two opposite GSG wafer probes.

Setup G1 and G2 are also based on a coupled pair of dielectric spheres working as resonators. G1 is based on Setup 2, and G2 is based on Setup 3. Photos of G1 and G2 are shown in Fig. 3.19(b) and Fig. 3.19(c). The corresponding dimensions and material parameters are listed in Table 3.6. The used alumina spheres of $0.5\,\mathrm{mm}$ (at $190\,\mathrm{GHz}$) and $1.588\,\mathrm{mm}$ (at $70\,\mathrm{GHz}$) with $0.57\,\mathrm{mm}$ diameter drilled centered hole are shown compared

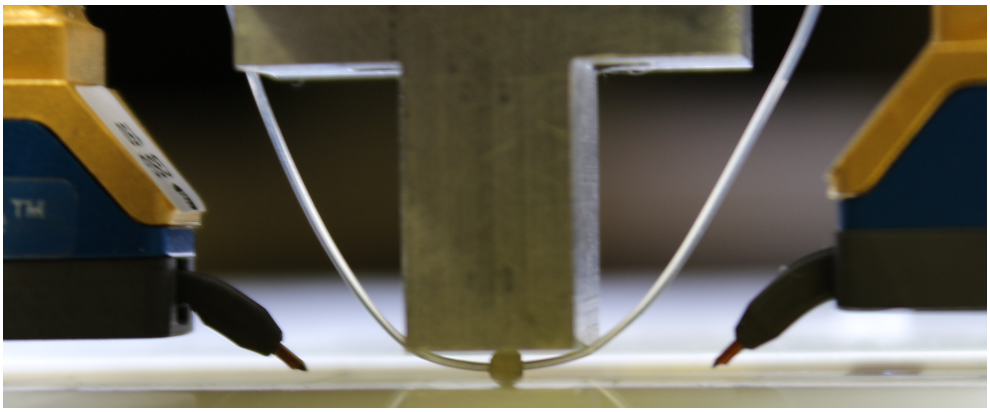

FIGURE 3.17: Photo of Setup 4 from the side. One $1.588\,\mathrm{mm}$ alumina sphere (with $0.56\,\mathrm{mm}$ drilled hole) sandwiched between the chip and top metal cover. PTFE tube is tightly pitched over the brick edges to the top.

TABLE 3.6: Dimensions and material parameters of the sensor circuit setup [12].

Parameter	Setup G1	Setup G2
polyimide substrate	thickness $18.5\,\mu\mathrm{m}$, $\epsilon_r = 3.5$, $\tan\delta = 0.0027$	
gold metal layer	$3.5\mu m$, $\sigma = 45.6MS/m$	
squared etched cavity in wafer for alumina sphere placement	$171\,\mu\mathrm{m}$ * $171\,\mu\mathrm{m}$	
alumina sphere	diameter $0.5\,\mathrm{mm}$, $\epsilon_r = 10$, $\tan\delta = 0.0013$	
distance spheres center-to-center	$1110\,\mu\mathrm{m}$	$1121\,\mu\mathrm{m}$
aluminium silicate glass tube	$\epsilon_r = 4.9$, $\tan\delta = 0.02$	
tube outer diameter	$77\,\mu\mathrm{m}$	$90\,\mu\mathrm{m}$
tube inner diameter	$27\,\mu\mathrm{m}$	$32\,\mu\mathrm{m}$

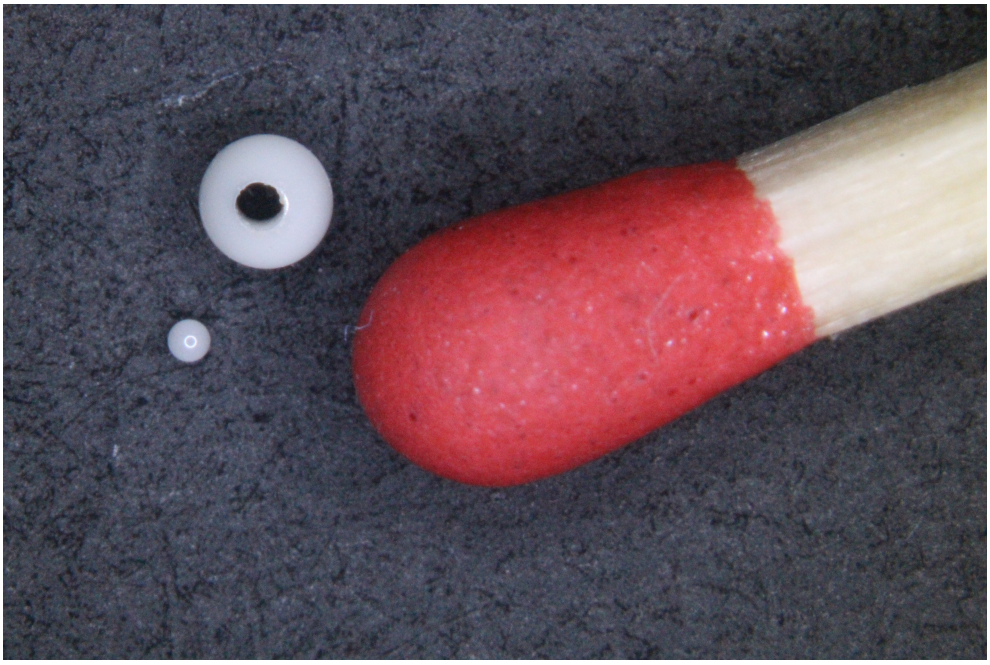

FIGURE 3.18: Photo of two spheres with diameter of $0.5\,\mathrm{mm}$ and $1.588\,\mathrm{mm}$ (with $0.56\,\mathrm{mm}$ drilled hole) in comparison with a match head.

with a match in Fig. 3.18. In Setup 4 is a PTFE tube inside the hole with $0.37\,\mathrm{mm}$ outer and $0.07\,\mathrm{mm}$ inner diameter.

Own simulations at sub-THz frequencies and the "FIG. 4" in [9] show that the sensitivity as defined in (3.1) needs to be expanded by the loss of the MUT. The reason is the noticeable influence of the loss on the resonance frequency because the imaginary part of the relative permittivity is now in the same magnitude as the real part for the used liquids at frequencies beyond $100\,\mathrm{GHz}$. This can be seen in Table 3.9 because $\tan\delta = [0.18;\ 1.45]$. At microwaves, the effect of the loss on the resonance frequency is negligibly small. Therefore the sensitivity at frequencies at W-band and higher is now called S_{THz} and is defined as in (3.2) [12]:

$$S_{THz} = \frac{(\Delta f_r/f_0)}{V/\lambda^3} \cdot \frac{1}{|\epsilon_r| - 1} \tag{3.2}$$

$|\epsilon_r|$, $\Delta f_r/f_0$, λ and V are the absolute value of the complex permittivity of the MUT, the resonance frequency shift from air to MUT, the free space wavelength and the active volume of the MUT.

As in Setup 2, in Setup G1 the first mode is also used for sensing. This mode with sensing region is shown in Fig. 3.19(d) (left). This mode has its E-field maxima in the middle between the spheres and is coupling mainly straight from one sphere to another. The MUT is penetrated perpendicular. On the other hand, Setup G2 also uses

the mode with the E-field penetrating the MUT parallel in the case of LUT in a tube shown in Fig. 3.19(d) (right). A picture diagonally above of this on-chip setup without top metal plate and the probes are up is in 3.19(a). The measurement is done with a network analyzer combined with a frequency extender for G-band (140 to $220\,\mathrm{GHz}$). To connect the thin-film board and network analyzer, Ground-Signal-Ground (GSG) probes with $75\,\mu\mathrm{m}$ are used. The transmission is measured, and therefore a Through-Reflect-Line (TRL) calibration is made on-board, and also the influence of the MSTLs feeding lines is removed with measurements of the long MSTL lines.

It has to be highlighted that Setups 4, G1, and G2 have a compact footprint and can be easily combined with integrated circuits because of the MSTLs. Therefore, these setups are ideal for on-chip applications. Another benefit of Setup G1 and G2 is that they could be scaled to even higher frequencies.

For the permittivity measurement of the mm-wave setups is the same procedure done as for the microwave setups, and also the CST Microwave Studio finite-element solver is used. A 3D model is geometrically corrected by comparing the simulation and measurement of the empty tube. More details follow in the next sections.

3.3.1 Constructions and handling (with difficulties)

As described in [10], a precisely manufactured sphere achieves the required mechanical accuracy for a mm-wave SDR. This is usually achieved with grinding. Also, it is essential to have shallow crates on the surface of the dielectric part of the board or in Back-End-Of-Line (BEOL) layers. These crates are etched in a standard thin-film process, so their dimensions and positions are very precise. The spheres can roll in the crate exactly and align themselves. Important therefore is, that the main emphasis has to be over the crate edge.

The build-up of the SDRS is more challenging than the SDR. As for the SDR, the probes are aligned to the probing pads. After this, they are held up again to avoid damage during the build-up of the sensor part. For Setup 4, the sphere was placed on the board by hand with a truncated syringe with its inner diameter smaller than the sphere linked via a tube with a vacuum pump for sucking. In this process, the sphere should be orientated so that the board does not cover the hole of the sphere. The next step is to sandwich the sphere with the top metal brick. After this, the PTFE tube can carefully be inserted in the hole. Now the tube is tightly pitched over the brick edge, and in this process, the sphere and the hole are automatically aligned in the wanted direction. The wanted direction – with the highest frequency shift and therefore the most accurate measurement – is the hole horizontal in extension to the ends of the MSTLs. See Fig. 3.17. Both tube sides are now fixed with tape on top of the metal brick.

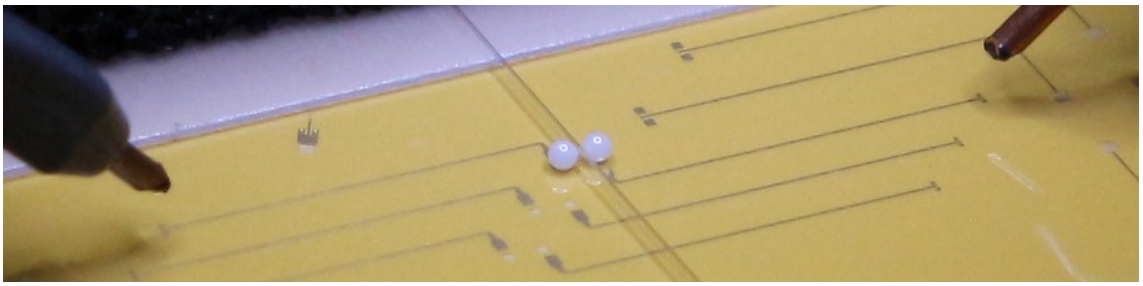

(a) Photo of Setup G2 with no top cover metal plate and lifted up GSG-probes

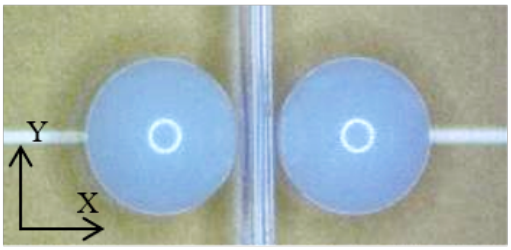

(b) Zoom-In top-view Setup G1

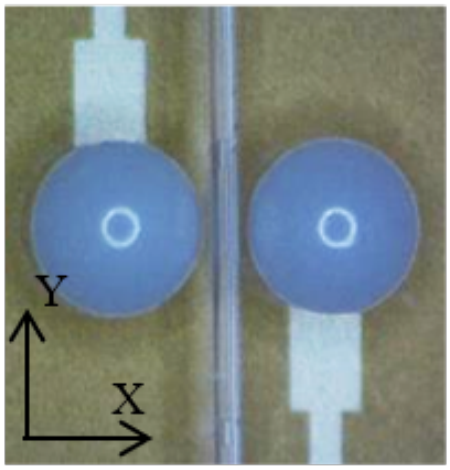

(c) Zoom-In top-view Setup G2

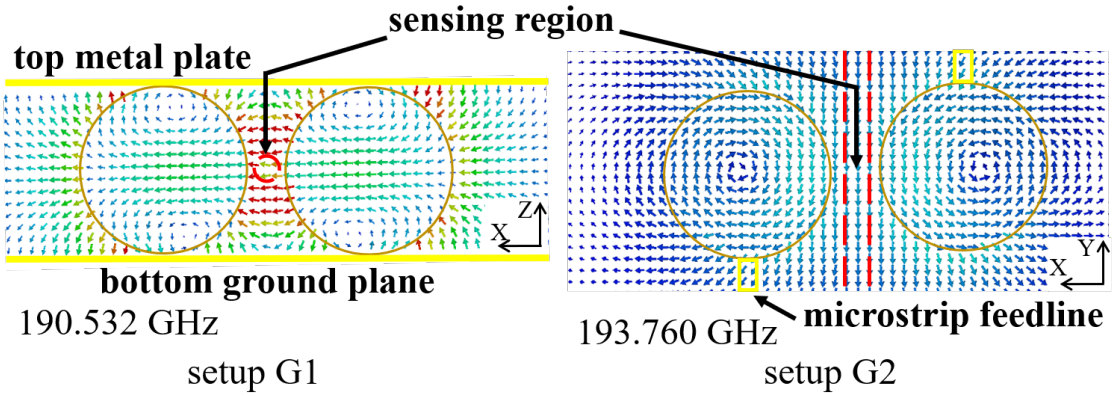

(d) Fieldplots of E-field at resonance frequency with sensing regions: (left) Setup G1 side view at $f_r = 190.532\,\mathrm{GHz}$ and in transverse cut symmetry plane and (right) G2 top view at $f_r = 193.760\,\mathrm{GHz}$ in horizontal symmetry plane

FIGURE 3.19: Setup G1 and G2: Photos from obliquely above and top (top metal cover plate is removed for the photos) and field plots [12]. Two alumina spheres with $0.5\,\mathrm{mm}$ diameter are placed self-aligned with a tube in between in an etched crate on a thin-film board. The signal is fed via open-ended MSTLs.

One end is linked in the bowl with the paper on top of the metal brick to absorb the pumped trough liquids, as shown in Fig. 3.20. The other end – the longer end – is connected to a syringe pump to inject the different liquids. After this build-up, the probes are placed on the circuit's probing pads for measurement.

The hole size of the sphere is more significant than the outer tube diameter. The reason is the difficulty of ultrasonic drilling a hole in the alumina ceramic. Alumina ceramic is a corundum and has $9\,\mathrm{MoshHardness(MH)}$. This is only one degree of hardness below a diamond with $10\,\mathrm{MH}$ [85]. This hole bigger than the tube diameter generates movement plays, especially with pump pressure on the tube, which also affects the measurement accuracy and repeatability of the measurement series.

An aluminum arm holds the metal brick. It is slowly approached with a micrometer positioner from the top to the sphere until it touches it. This is verified simultaneously with the transmission peak at the VNA. After touching, extra pressure can be adjusted until the resonance transmission peak reaches its maximum transmission and, therefore, the sharpest peak with the highest Q-factor.

Another problem with PTFE tubes and the most other tube material is their high wall thickness. This increases the gap between the spheres, which reduces the E-field focusing and, therefore, the sensitivity. Also, should the material be lossless so that the resonance is stable and enough of the E-field penetrates the LUT. Electronic beam melted, and elongated silicate glass tubes fulfill these conditions [86]. At microwave, quartz silicate glass is used; at sub-THz, it is aluminum silicate glass because it is available in smaller dimensions.

The dived screws between the holding arm and metal top cover brick have to be loose so that the metal cover brick is hanging under the extension of the positioner and has a few hundred micrometers scope/margin when placing the metal brick on top of the sphere.

The probes are sensitive to any mechanical movement and pressure. Therefore to avoid any damage to the probes or changes of the setup as a rotating sphere, the PTFE tube was tightly pitched over the edges of the top cover metal block (see Fig. 3.17) and one tube end was channeled in the paper of the bowl on top as shown in Fig. 3.20. The other end of the tube was directed away and used to inject the different LUT with a syringe manually.

The G1 and G2 setups needed an even smaller, more mechanically stable tube, especially considering the diameter changing with pressure. Aluminum silicate glass was used with the characteristics from Table 3.6. The measurement setup for all spectroscopy probing measurements is shown in Fig. 3.21. The sphere(s) are in the middle of the photo between the mm-Wave probes. The tube and LUT are between the

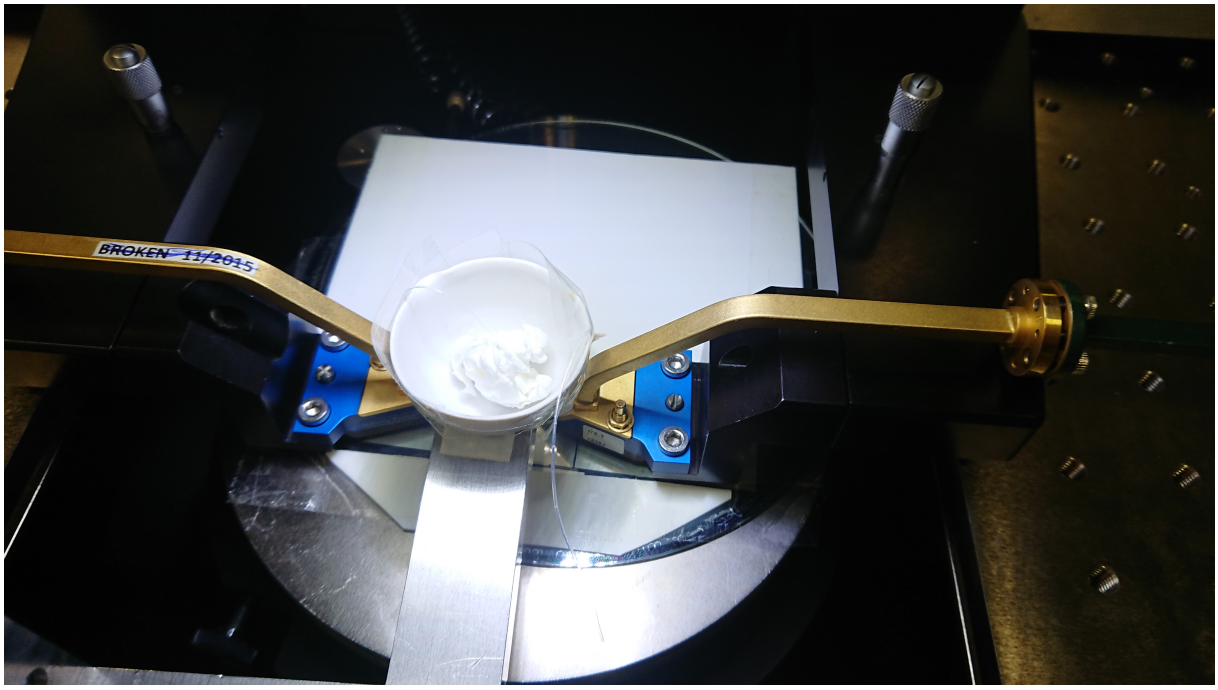

FIGURE 3.20: Top view measurement setup at mm-waves with $1.588\,\mathrm{mm}$ diameter spheres sandwiched on-chip and bowl with absorbing white paper on top for the LUT measurement [11].

spheres or in the sphere. On top of the sphere is the metal cover held by an aluminum arm. An electrical syringe pump is placed in front.

The tube system with holder and connection to pipe / tube from Fig. 3.21 is built up as in Fig. 3.22. The thick end of the tube system is shown in Fig. 3.22(a). A blunt syringe is glued in a PTFE tube. In Fig. 3.22(b) is the central part of the tube system. The PTFE tube is clasped by a twisted silicone lip. This silicone lip is an inner part of the transparent plastic piece. This plastic piece is attached to the grey holding structure. A short piece of a thinner PTFE tube is glued inside the hold PTFE tube. In this thinner tube, the glass tube is glued. Everything needs to be firmly glued and fixed to survive the high liquid pressures needed to counteract the capillary effect and also be able to change the LUTs. Additionally, the glass tube is glued in a metal sleeve which is also held with the same gray holding structure as the transparent twister. Therefore the most vibration-stable setup is built up. The plastic holder is linked via alumina holding structures with a micrometer mechanical positioner mounted on the probing table. Using a microscope, the glass tube is aligned between both spheres and then burdened on the open side with a piece of foam rubber placed with strings. This is shown in 3.19(a). After this, the tube is finely adjusted, and the LUT can be injected for measurement.

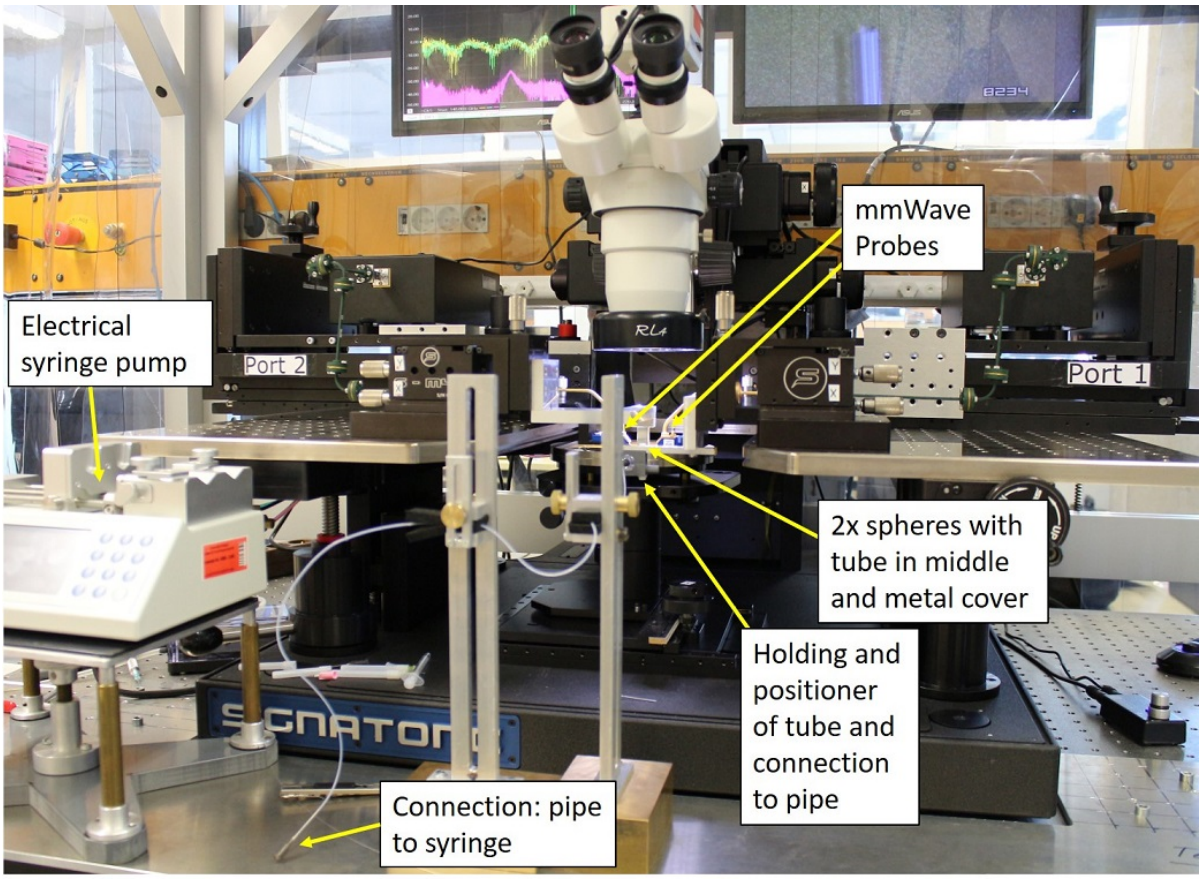

FIGURE 3.21: Photo of measurement setup for G1 and G2.

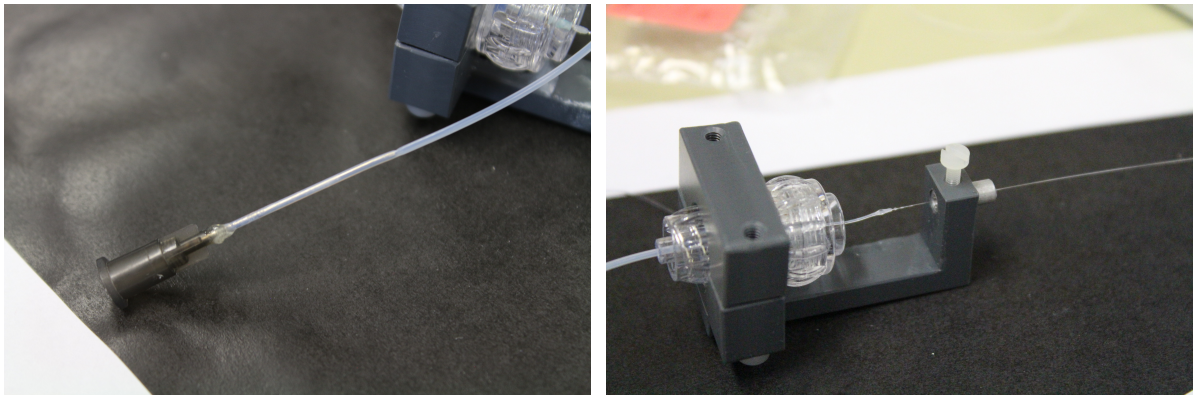

(a) (b)

FIGURE 3.22: a) Syringe glued in a flexible tube. b) holder of glued-together flexible and glass tubes. The glass tube is also glued in a metal sleeve fixed with a screw. A twisted silicone membrane holds the flexible tube.

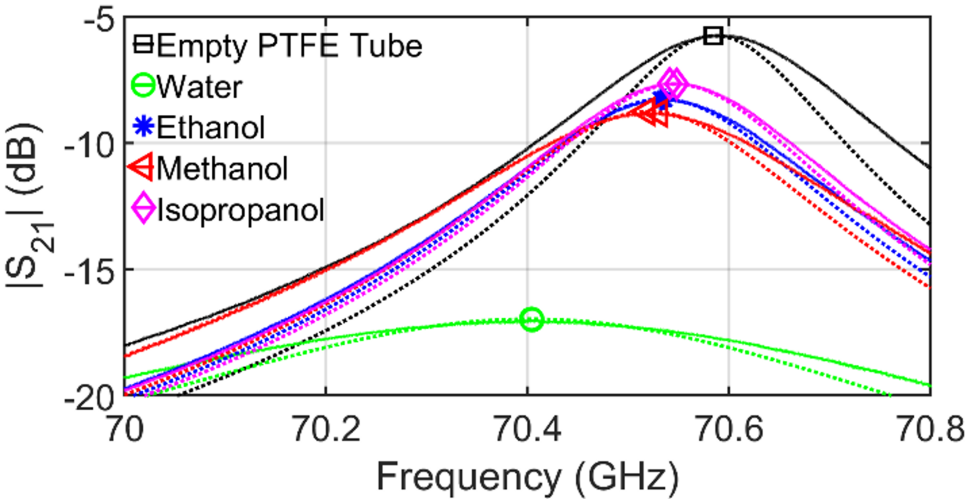

FIGURE 3.23: Measured resonant transmissions (solid) and the corresponding best-fit simulation (dotted) of Setup 4 [11].

3.3.2 Spectroscopy of LUT

Various liquids were measured at $70\,\mathrm{GHz}$ and with small liquid quantities as small as $10\,\mathrm{nanoliters}$ and around $190\,\mathrm{GHz}$ as small as $0.35\,\mathrm{nanoliters}$. The active volume length of the tubes as mentioned in section 3.1 is 1.5 times the diameter of the sphere for Setup 4. The active tube length is 1.2 and 2.6 times the sphere diameter for Setup G1 and G2. The active length is chosen in the way that the difference of the simulated resonance frequency shift of the sensor between an infinitely long tube and the chosen length is less than 1%. For the dielectric sensors in [7] working with whispering gallery modes, the active volume is the LUT in the tube with the length attached to the dielectric disk. For the photonic crystal resonator in [9], the active volume is the tube with the length of the thickness of the dielectric slab [11]. The measurement results (solid), together with the fitted simulation (dotted) curves, are shown in Fig. 3.23. The extracted permittivity values, the calculated Debye values, and the deviation error are listed in Table 3.7. In Table 3.8 are the sensitivities S listed for the state-of-art compared with the Setup 4 for high ($\epsilon_r \geq 8.5$) and low ($\epsilon_r \leq 3$) permittivity values for mm-wave at their resonance frequencies.

The measurements for Setup G1 and G2 at $190\,\mathrm{GHz}$ are more noisy than for Setup 4, which is at $70\,\mathrm{GHz}$. Therefore, extra data process steps are necessary to accurately extract the values of the LUT. In Fig. 3.24, there is the measured raw and the smooth data of the resonances of the already described modes to sense and the fitted simulation curve. It is the absolute transmission value $|S_{21}|$ at resonance in the case of air instead of LUT. At first, the influence of the long feeding MSTLs had to be subtracted. This raw data is the dark blue and red curve for Setup G1 and G2. After the influence is

TABLE 3.7: Calculated permittivity values of the measurement results of the LUT at $25\,^{\circ}\mathrm{C}$ with Setup 4 [11].

LUT	measured f_r (GHz)	textbook (Debye)		fitted in simulation		relative error (%)	
		ϵ_r	$\tan\delta$	ϵ_r	$\tan\delta$	$\Delta\epsilon_r$	$\Delta\tan\delta$
water	70.405	11.0	1.69	9.2	1.3	18	26
ethanol	70.535	3.40	0.29	3.4	0.46	0	45
meth.	70.520	4.94	0.45	4.0	0.48	21	6
prop.	70.549	2.78	0.17	2.8	0.42	0.7	85
air	70.591	1	0	1	0	–	–

TABLE 3.8: Sensitivity comparison for mm-waves and high permittivity [11].

setup	E-field direction	f_r (GHz)	ϵ_r	active length (mm)	active volume (μl)	sensitivity S
[7]	n.a.	35.4	22.5	12	0.33	0.014
[7]	n.a.	35.4	3.0	12	0.33	0.11
[9]	$\perp$	99.0	8.5	0.525	0.007	0.33
[9]	$\perp$	99.0	3.0	0.525	0.007	0.49
4	$\parallel$	70.4	9.2	2.38	0.009	2.7
4	$\parallel$	70.5	2.8	2.38	0.009	2.8

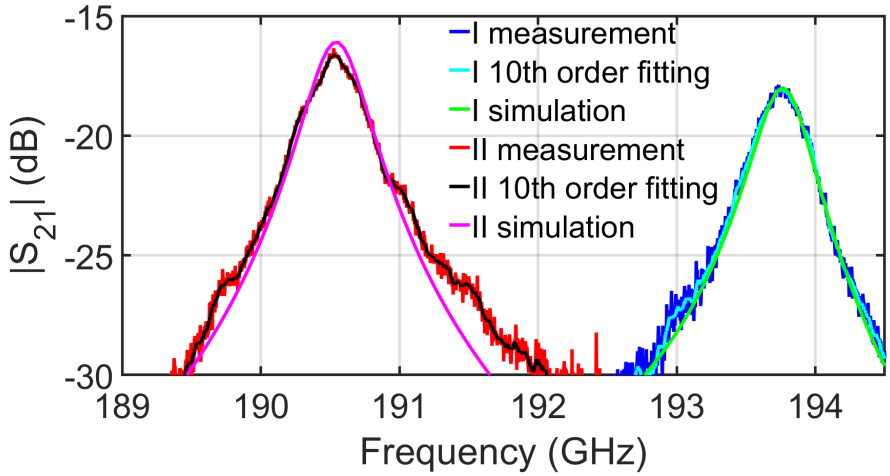

FIGURE 3.24: Raw and smoothed measured data and the simulated (fitted) transmission $|S_{21}|$ data of Setup G1 and G2 [12].

removed, the random variations in data are smoothed with a simple low pass Finite Impulse Response (FIR) in MATLAB with the "movmean" function [87]; see the light blue and black curve. The dimensions of the 3D models with no LUT in the tube are changed in the range of manufacturer datasheet tolerances and simulated in CST until the simulation result fits the smoothed curves. These air-filled Setup G1 and G2 simulation results are the pink and green curves in Fig. 3.24.

The last step to determine the permittivity of the LUT is to fit the simulation with liquid to the corresponding measurement and extract the real part of the permittivity and loss tangent of the LUT. These curves of the measurement (solid) and fitted simulation (dotted) of the LUTs: water, acetone, ethanol, methanol, isopropanol; are shown in Fig. 3.25 and Fig. 3.26. The best-fitted values for the dielectric constant ϵ_r and the loss tangent $\tan\delta$ of the LUTs are shown together with the corresponding Debye values calculated with the dipole-relaxation model from [88] in Table 3.9. It is differentiated between the perpendicular E-field penetration of the LUTs' flow in Setup G1 and the parallel penetration in Setup G2. ϵ_r and $\tan\delta$ influence the resonance frequency and the quality factor and therefore were used to fit the simulations. Table 3.9 also includes the resonance frequency shift $\Delta f = f_r - f_0$ and the quality factor shift $\Delta Q = Q_r - Q_0$ both caused by the LUT's perturbation. The 3D full-wave simulation fitted values agree very well with the calculated and expected Debye values. One reason for the differences is the problem with the temperature stability of the room and also the LUTs, which leads to a temperature uncertainty of $\pm 1°$ C at 25° C.

The classification of Setup G1 and G2 is done in Table 3.10. This table compares the needed volume of LUT absolute in nl and its relation to the resonance free-space wavelength λ_0 and the sensitivity S_{THz} with the state-of-art. It should be mentioned

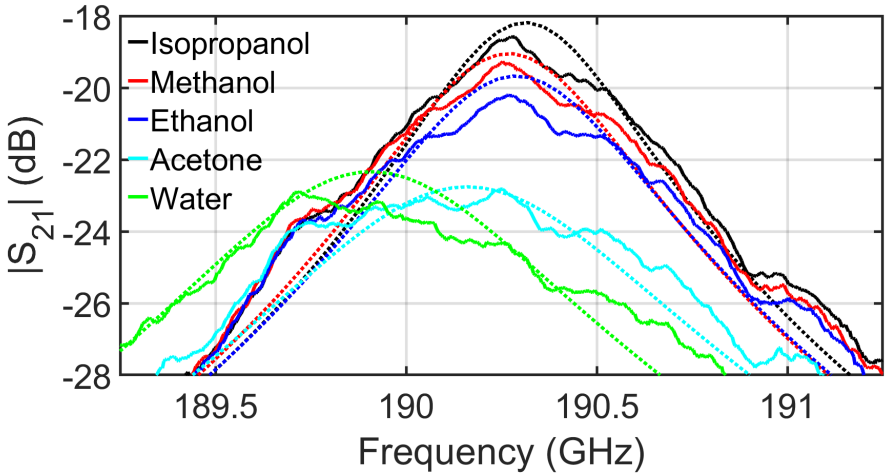

FIGURE 3.25: Measured resonant transmissions (solid) and the corresponding best-fit simulation (dotted) of Setup G1 [12].

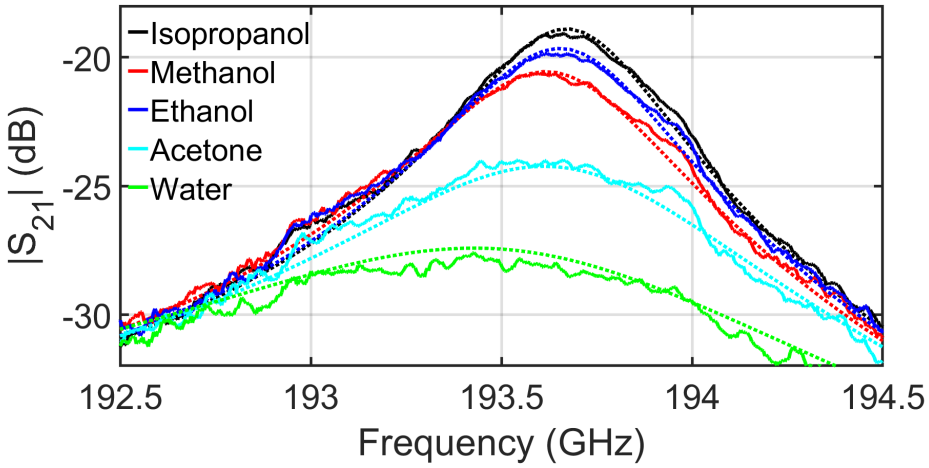

FIGURE 3.26: Measured resonant transmissions (solid) and the corresponding best-fit simulation (dotted) of Setup G2 [12].

that some values from Table 3.10 differ from the values in Table 3.8 because of different ways of looking at and interpreting cited works and a more accurate way of calculating the sensitivity with S_{THz} instead of S by including the imaginary part of the complex permittivity of the LUTs. It is necessary to mention that in [9], the active volume of LUT is given as $3.6\,\mathrm{nl}$ but without more detailed information about how the simulation was interpreted, especially as how long the active volume in the tube was assumed. If $3.6\,\mathrm{nl}$ would be taken, the responding sensitivity would be $S_{THz} = 0.92$.

TABLE 3.9: Setup G1 ($f_0 = 190.532\,\text{GHz}$) and G2 ($f_0 = 193.760\,\text{GHz}$) from measurements extracted results in comparison to Debye model data [12].

LUT	Δf (GHz)	ΔQ	Simulations fitted to measurements		Debye formulations [88]	
			ϵ_r	$\tan\delta$	ϵ_r	$\tan\delta$
Setup G1: E-field perpendicular to flow of LUT:						
Water	0.564	195.6	6.10	1.1	5.95	1.33
Ethanol	0.274	135.9	2.90	0.46	2.90	0.30
Methanol	0.284	116.4	3.20	0.36	3.57	0.44
Acetone	0.4	216.8	3.15	1.20	3.15	1.44
Isopropanol	0.24	86.0	2.80	0.25	2.52	0.11
Setup G2: E-field parallel to flow of LUT:						
Water	0.315	317.8	6.2	1.45	5.91	1.32
Ethanol	0.105	85.8	2.92	0.31	2.89	0.30
Methanol	0.14	125.2	3.52	0.42	3.55	0.44
Acetone	0.14	244.0	3.4	1.35	3.11	1.43
Isopropanol	0.07	49.8	2.65	0.18	2.51	0.11

TABLE 3.10: Comparison of Setup G1 and G2 with the state of art techniques [12].

resonator type [ref]	active length of LUT (mm)	volume V of LUT		sensitivity S_{THz}
		nl	λ_0^3	
WGM at 35.4 GHz [7]	12	333.1	0.00055	0.10
dielectric sphere at 70.6 GHz [11]	2.38	9.2	0.00012	2.47
metal cavity at 82.8 GHz [5]	2.54	13090	0.01	0.007
SIW cavity at 92.6 GHz [6]	N/A	N/A	N/A	-
photonic crystal 99 GHz [9]	0.525	4.1	0.00015	0.8
WGM at 167.3 GHz [8]	6.56	206	0.036	0.0006
this work, Setup G1, at 190.3 GHz [12]	0.6	0.35	0.00009	7.26
this work, Setup G2, at 193.7 GHz [12]	1.3	1.0	0.00027	1.04

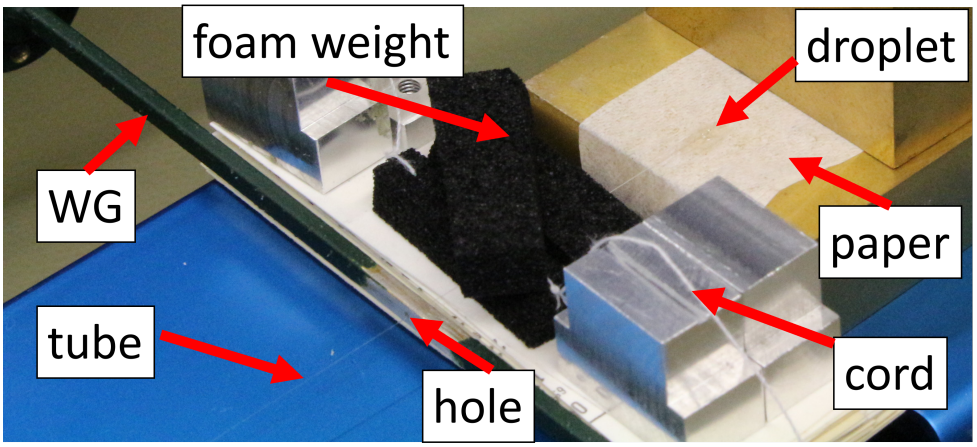

FIGURE 3.27: G-Band WG with hole and tube inside to measure LUT.

3.3.3 LUT measurement with G-band WG

S-parameters measurements of different LUTs at different temperatures were done with a G-band WG (from 140 GHz to 220 GHz) to determine the permittivity values of all LUT over the full G-band. These values should be used for comparison and evaluation with the measurement results with the resonator. This did not work well.

Setup G-band WG measurement assembling

The standard procedure to measure the permittivity with a WG is to fill a piece of the WG wholly or partly with the MUT. A filling was impossible because of the high loss of the LUTs and partially filling not because of the small dimensions. Therefore, the approach with a tube through the WG was tried. At first, a hole (diameter $\approx$ 200 µm) was drilled in the middle through both long sides in the middle of a 10 cm long 2:1 ratio standard WG and a glass tube (diameter $\approx$ 100 µm) inserted. See Fig. 3.27. Additionally, to prevent the tube to move, black foam weights were placed with the help of white cords on the back part of the tube. Then the tube was pulled back a little bit to get tension on the tube, straighten it and therefore reduce the tube movements. Under the open end of the tube with a small amount of space is a white paper to absorb the LUT droplets. During the measurement, LUT is pressed through the tube and collects itself at the open end of the tube in an increasing droplet. The tube bends down at some point due to the rising droplet's weight. The white paper absorbs the droplet, and the tube bends up again. Absorbing the droplets combined with the space between the open tube's end and the paper helps by changing the LUTs. For the LUTs change, the liquid is sucked back completely, and a new syringe pump with another liquid is connected to the system.

Results G-band WG

The S-parameters measurement results of phase and amplitude of different LUTs at 50°C are shown in Fig. 3.28, Fig. 3.29, Fig. 3.30 and Fig. 3.31.

The measurement set-up had room temperature, and the LUT was heated to 50°C before it was injected. The interference because of the drilled hole is the first thing that catches the eye. In Fig. 3.28(a) and Fig. 3.29(a) the defect caused by the hole in the WG is well visible at $210\,\mathrm{GHz}$ because of the transmission drop and reflection peak. The hole is a discontinuity, and therefore a resonance appears in the WG, which makes it impossible to estimate the permittivity of the LUT analytically over the full band. If it would be possible to calculate the permittivity despite the hole for frequency subsections, is not been researched yet. With full-wave simulations, the permittivity values of the LUTs could be estimated as Fig. 3.28(a) to Fig. 3.31 show but not in a useful duration if it has to be done for several frequency points (to determine the permittivity for the full G-band) and also several temperatures to create a permittivity overview table.

Another critical point with the measurement is the inconsistency of the results for different LUT. The permittivity of the measured LUT should change similarly, and there should not be a curve crossing for the different LUTs. Because of these reasons, these measurements seem not exploitable to determine the permittivity of the LUT.

3.3.4 Spectroscopy of single particle in flow in liquids

The spectroscopy of particle in-flow at microwave already showed that it is possible to detect and distinguish particles with the different setups of this work. At mm-wave the same glass tube with $0.7\,\mathrm{mm}$ outer diameter and $0.5\,\mathrm{mm}$ inner diameter, the same particles, and additional a $0.4\,\mathrm{mm}$ metal and a $0.4\,\mathrm{mm}$ Al2O3 particle are used together with Setup 2 at $30\,\mathrm{GHz}$. The spheres with a particle in the center in a tube filled with water are shown in Fig. 3.32. With this big diameter of the tube related to the wavelength and the increased loss of the carrying liquids because of the higher frequency, only Setup 2 is usable. Additional to water also, isopropanol was used as particle carrying liquid. The measurement results for water and isopropanol are shown in Fig. 3.33, Fig. 3.34, Fig. 3.35 and Fig. 3.36. The idea behind different carrier liquids is to see how a particle influences the resonance once in a medium such as water with a higher permittivity than the particle and once in a medium such as isopropanol with a lower permittivity than the particle.

To understand the resonance behavior, it is important to take a look at the permittivities of the particle and the carrying liquids. The real part of the relative permittivity and

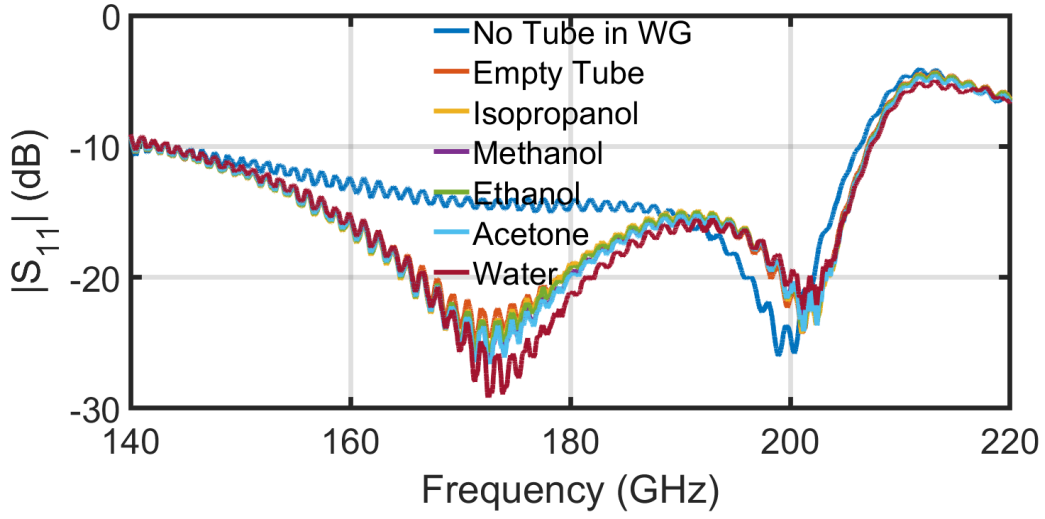

(a)

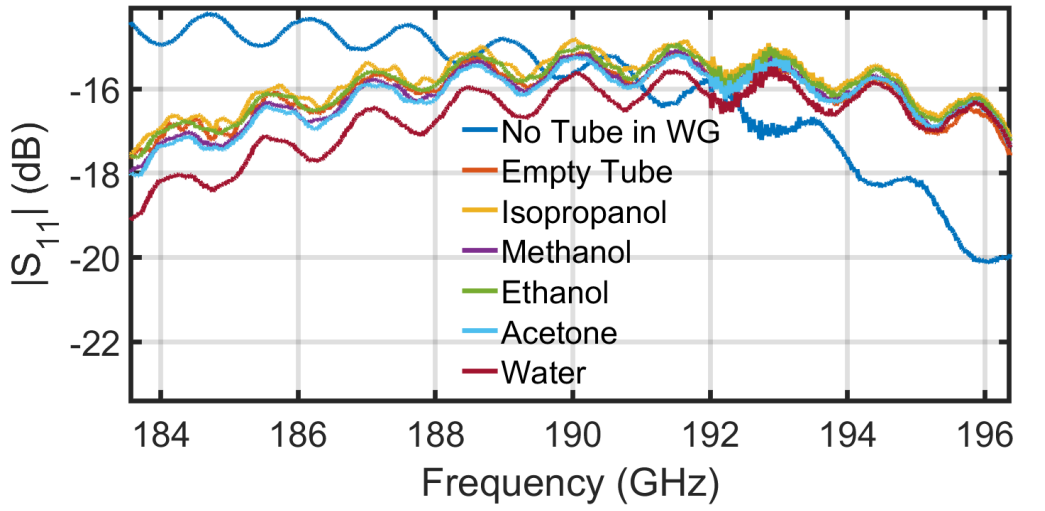

(b)

FIGURE 3.28: Measurement S_{11} amplitude results of a G-band WG with a hole and tube inside with different LUTs. (a) reflection S_{11} in dB. (b) zoom of reflection S_{11} in dB.

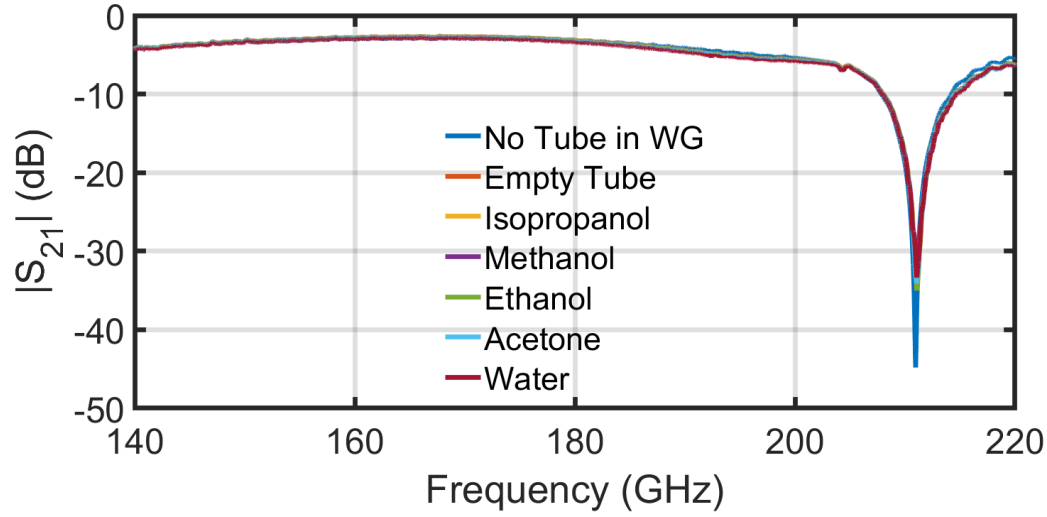

(a)

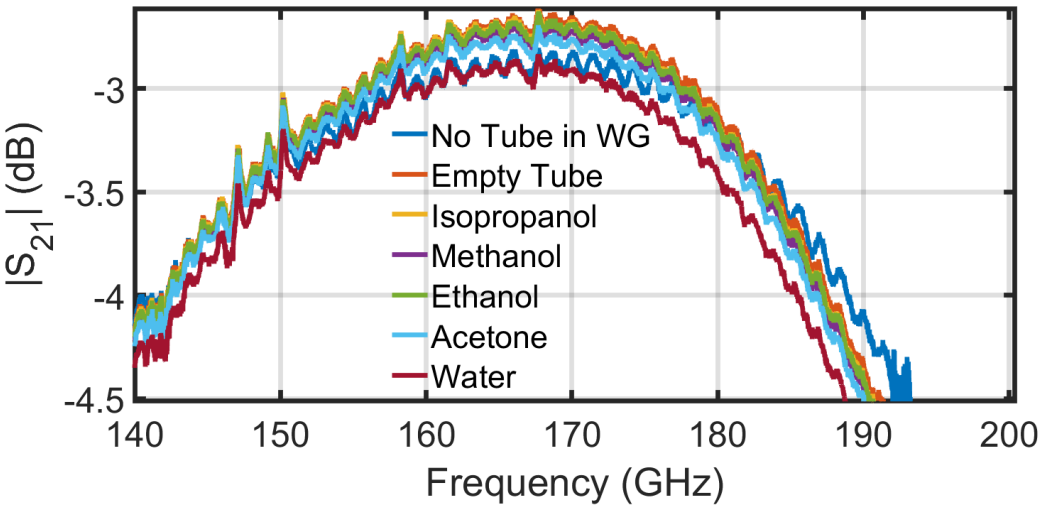

(b)

FIGURE 3.29: Measurement S_{21} amplitude results of a G-band WG with a hole and tube inside with different LUTs. (a) transmission S_{21} in dB. (b) zoom of transmission S_{21} in dB.

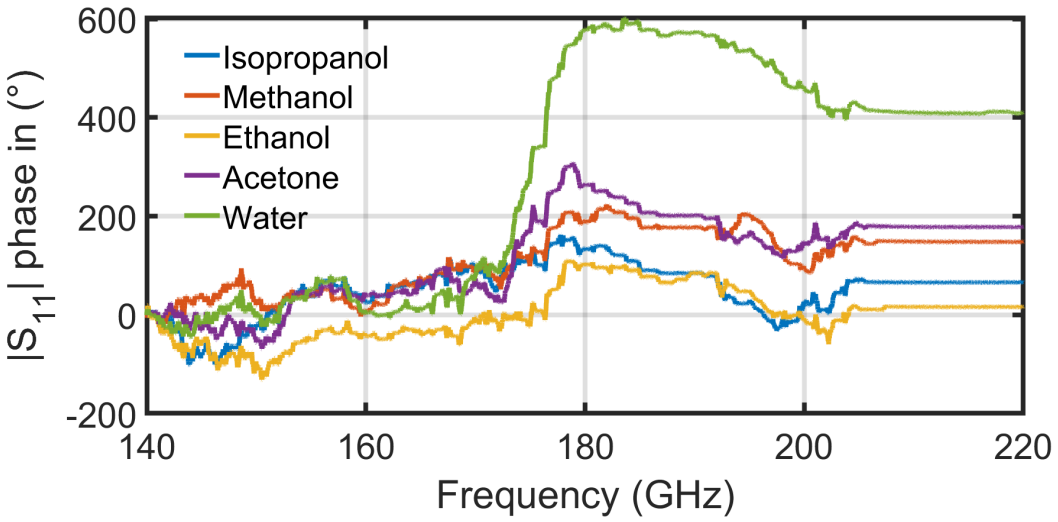

FIGURE 3.30: Measurement results of the reflection S_{11} phase of a G-band WG with a hole and tube inside with different LUTs. The phase of the measurement of the empty tube was subtracted from the measurements of LUT inside the tube

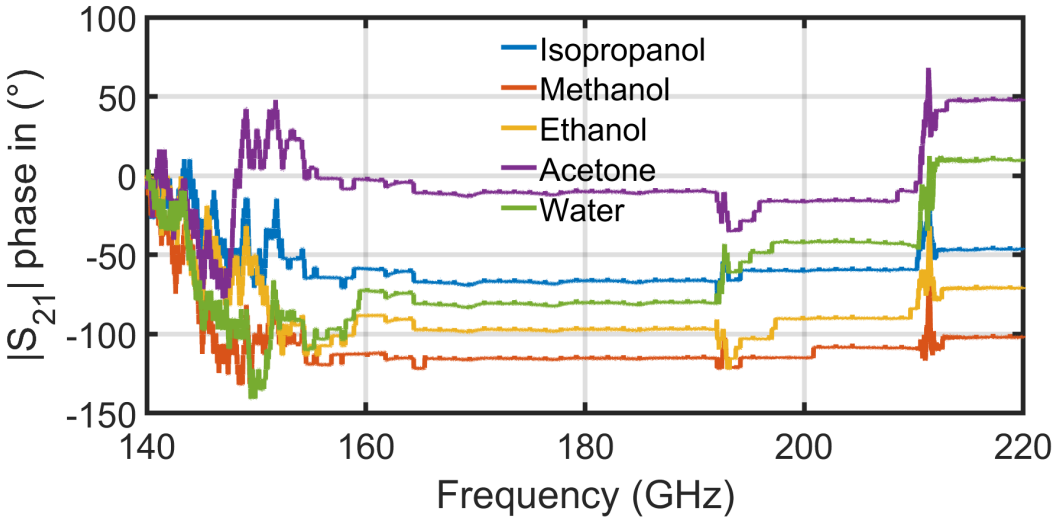

FIGURE 3.31: Measurement results of the transmission S_{21} phase of a G-band WG with a hole and tube inside with different LUTs. The phase of the measurement of the empty tube was subtracted from the measurements of LUT inside the tube

FIGURE 3.32: Setup 2 at 30 GHz 0.4 mm silicon particle in tube filled with water.

the $\tan\delta$ of water and isopropanol are $\epsilon_{r,water} = 26.20$, $\tan\delta_{water} = 1.24$; $\epsilon_{r,isoprop} = 3.01$, $\tan\delta_{isoprop} = 0.19$; at 30.7 GHz and $\epsilon_{r,water} = 25.46$, $\tan\delta_{water} = 1.26$; $\epsilon_{r,isoprop} = 3.01$, $\tan\delta_{isoprop} = 0.19$ at 31.5 GHz after Debye.

The ceramic particles have a permittivity and loss at 30 GHz of circa: $\epsilon_{r,ruby} \approx \epsilon_{rAl_2O_3} \approx 10$ and $\tan\delta_{ruby} \approx \tan\delta_{Al_2O_3} \approx 10^{-3}$.

The silicon and metal particle have the values: $\epsilon_{r,silicon} \approx 12$ and $\epsilon_{r,metal} \approx \infty$ and $\tan\delta_{silicon} \approx 10^{-4}$ [89]. The $\tan\delta$ of the metal particle is calculated with the equation $\tan\delta_{metal} = \frac{\sigma}{\omega\epsilon} \approx \frac{\sigma}{\omega\infty} = 0$.

At last, there is the evaluation. In Fig. 3.33(a) to Fig. 3.34(b) are the transmission measurement results of the particles surrounded by water, in Table 3.11 are the important determined values: the resonance frequency and amplitude of the different particles compared to no particle and the differences $\Delta f_r = f_{r,\text{particle}} - f_{r,\text{no particle}}$ and $\Delta|S21| = |S_{21,\text{particle}}| - |S_{21,\text{no particle}}|$. Ruby, alumina, and silicon have a lower permittivity than water. Therefore the upwards frequency shift is as expected, and also for metal with a higher permittivity to a lower frequency. The reduction of the amplitude for the three dielectric particles, although they are less lossy than water, depends on the behavior of Setup 2. As the LUT measurements results in Fig. 3.11 show, the amplitude is also linked with the real part of the permittivity and not only with the loss.

In Fig. 3.35 and Fig. 3.36, the influence of the particles on the transmission resonance in the surrounding medium isopropanol is shown, and in Table 3.12 the corresponding determined values. Isopropanol has a lower permittivity than all of the particles. Therefore, the particles reduce the resonance frequency.

With isopropanol, the particles create a more significant change in frequency and amplitude than water. There are two reasons for this. The first: Setup 2 is more sensitive to low permittivities, as we know from the measurement results of Setup G1. The second: the permittivity of ruby and silicon is circa three times and four times the values of the isopropanol, and the permittivity of water is only circa 2.6 and 2.2 times the value of ruby and silicon.

This work measured the particles in the middle and then pumped them away. Later, they should be measured in flow. Therefore a fast measuring and saving VNA is

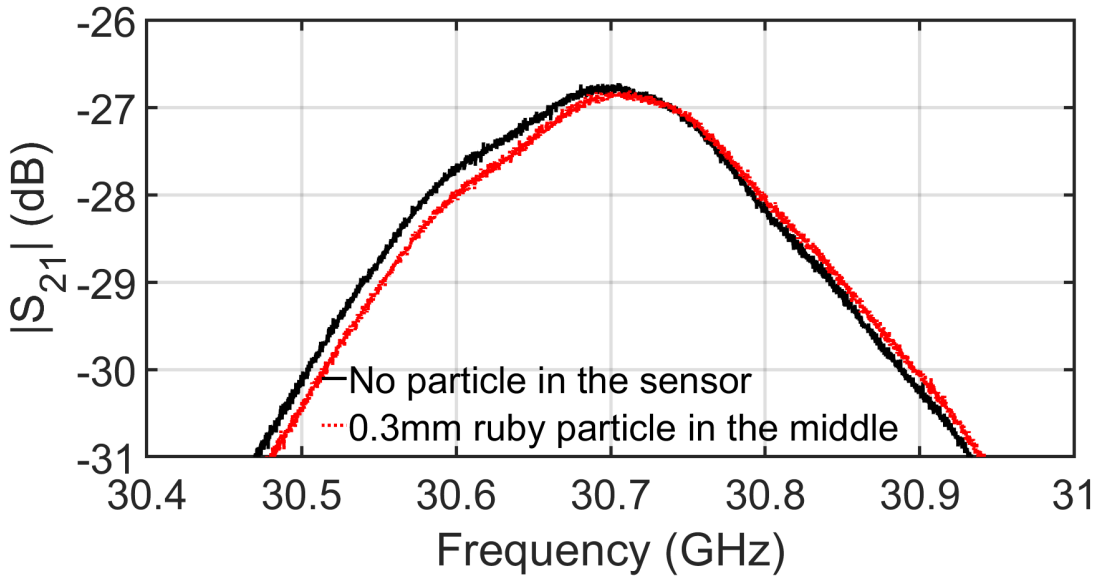

(a) Setup 2 at 30 GHz: 0.3 mm ruby particle.

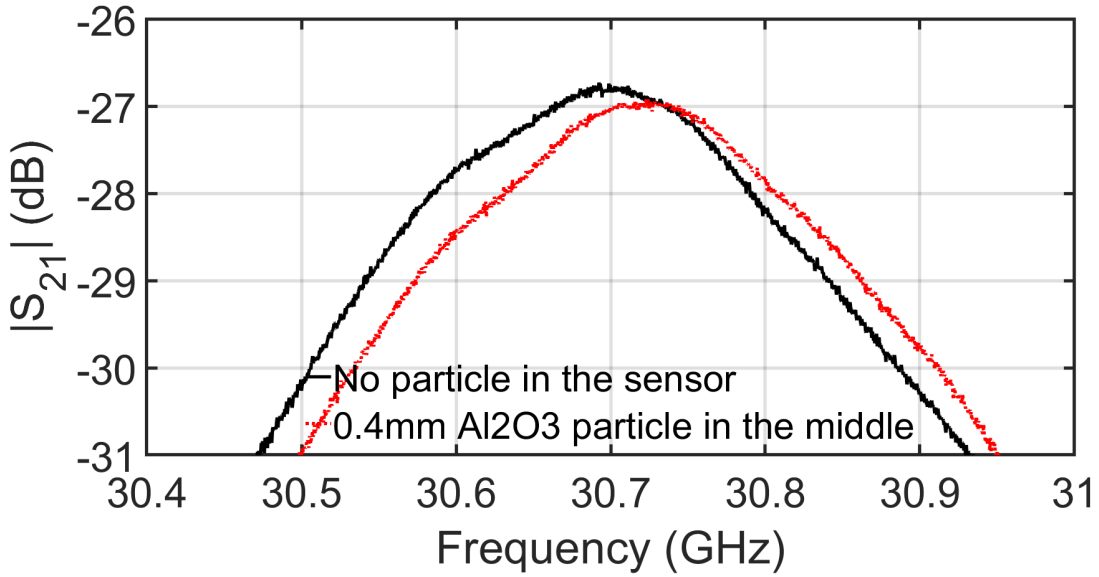

(b) Setup 2 at 30 GHz: 0.4 mm Al_2O_3 particle.

FIGURE 3.33: Transmission measurements of ceramic particle in-flow in water in a glass tube at mm-waves.

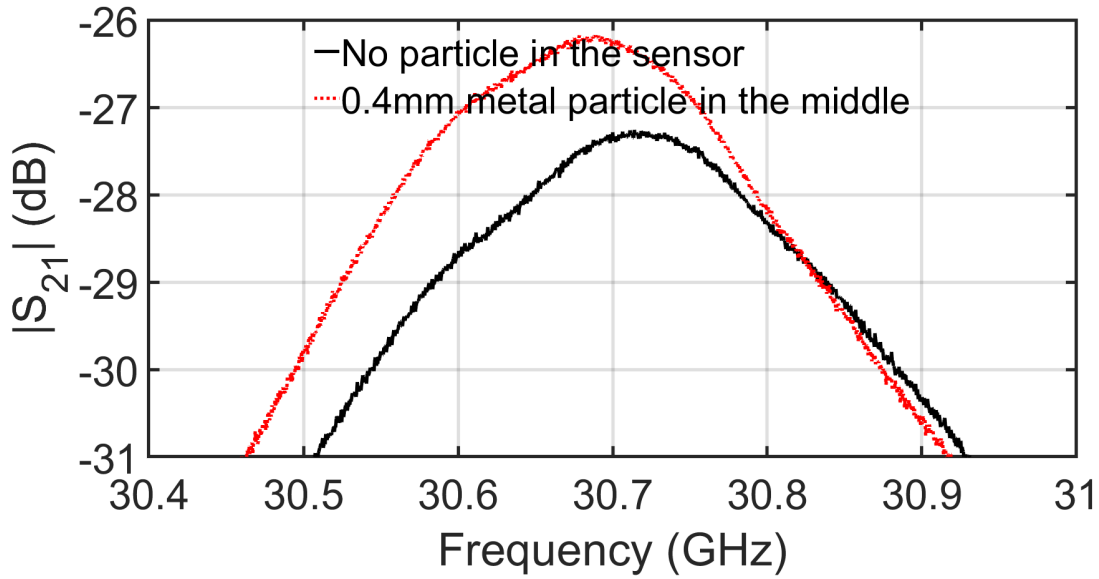

(a) Setup 2 at 30 GHz: 0.4 mm metal particle.

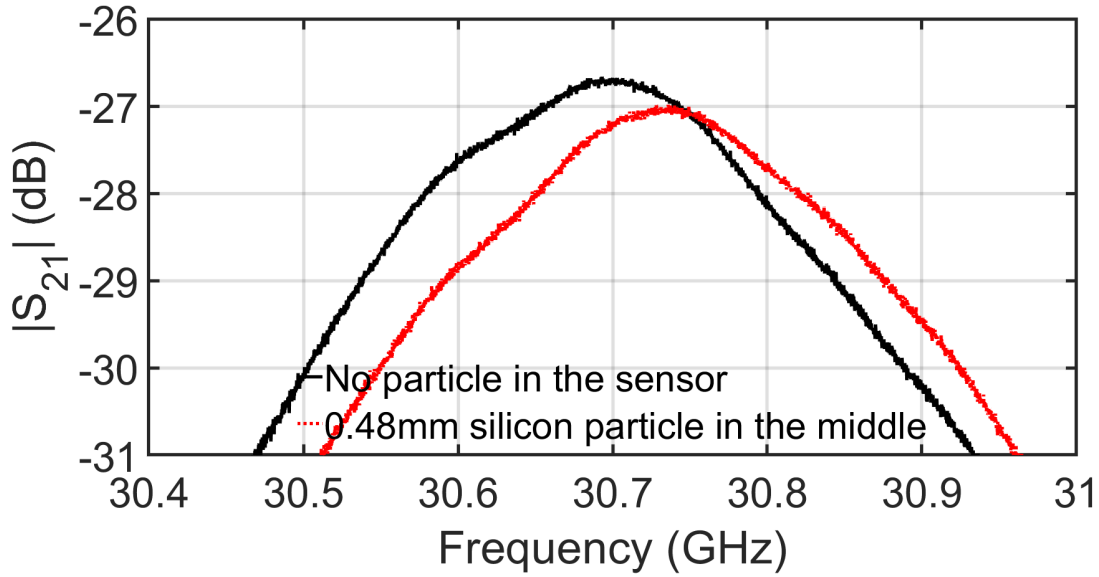

(b) Setup 2 at 30 GHz: 0.48 mm silicon particle.

FIGURE 3.34: Transmission measurements of (semi-)conductor particle in-flow in water in a glass tube at mm-waves.

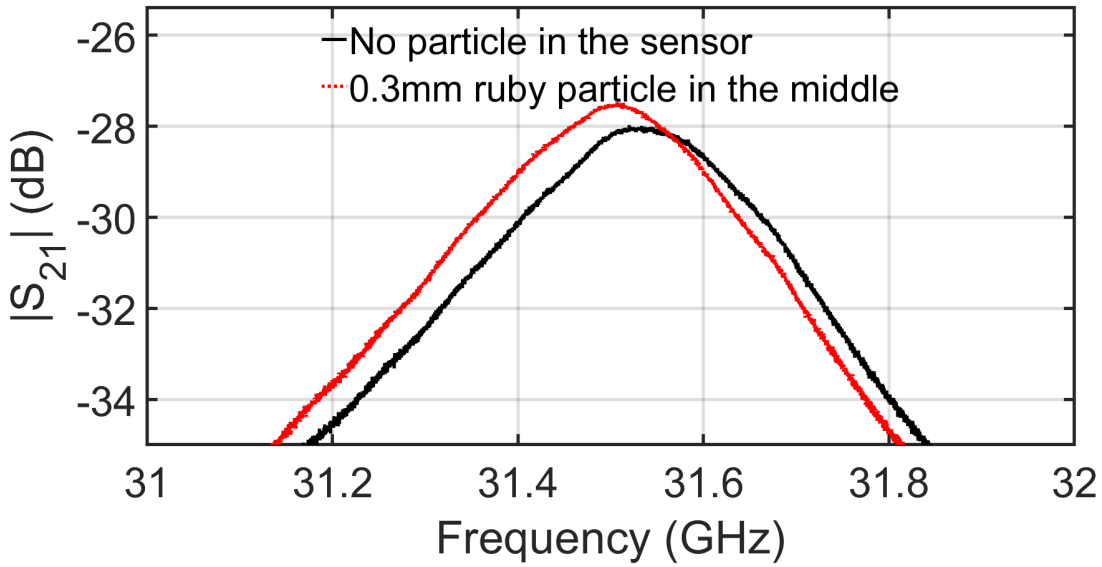

(a) Setup 2 at 30 GHz: 0.3 mm ruby particle.

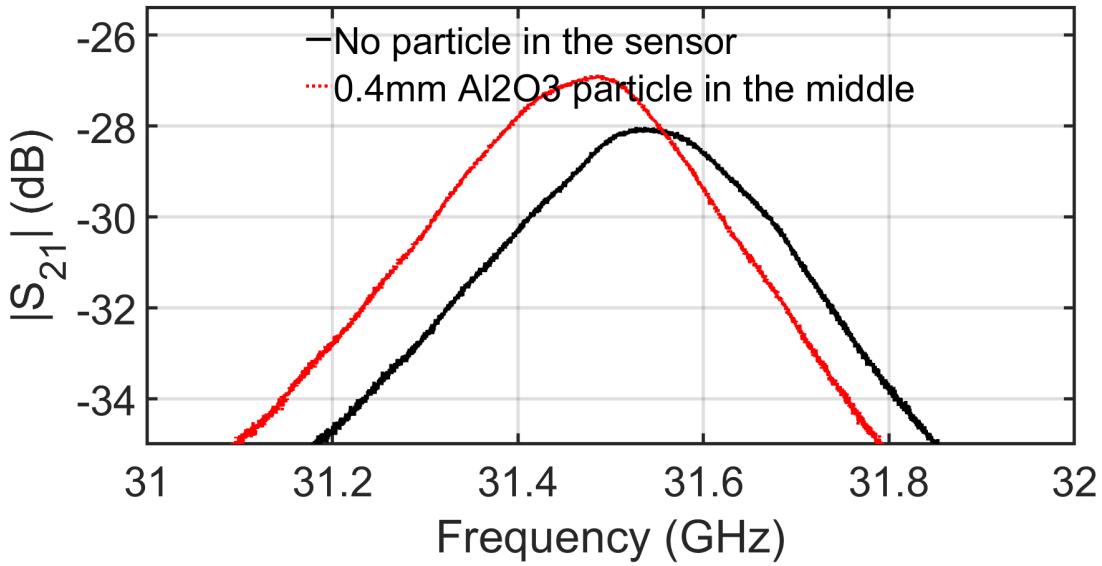

(b) Setup 2 at 30 GHz: 0.4 mm Al_2O_3 particle.

FIGURE 3.35: Transmission measurements of ceramic particle in-flow in isopropanol in a glass tube at mm-waves.

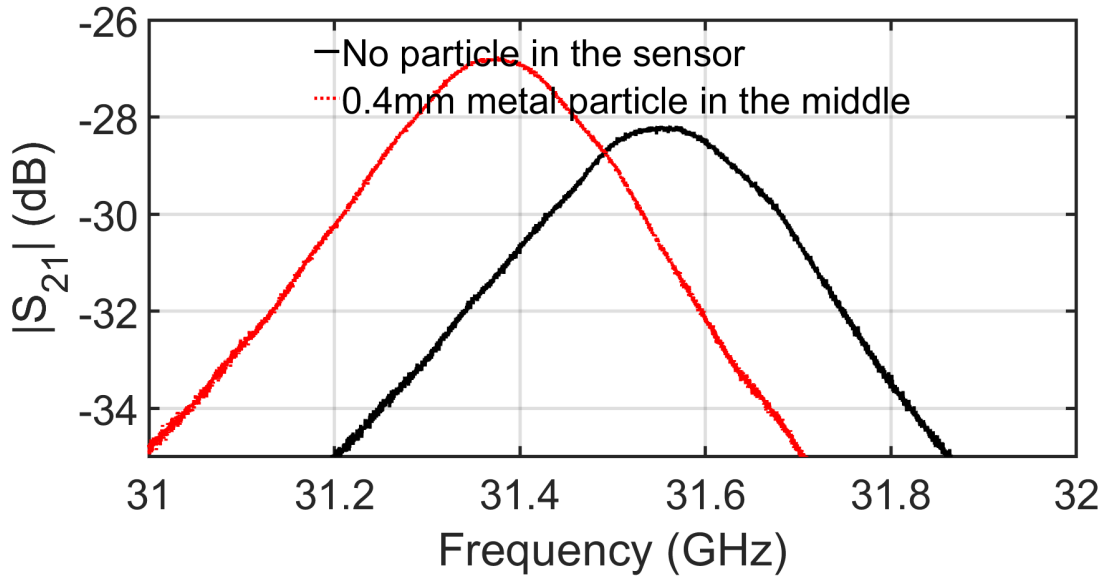

(a) Setup 2 at 30 GHz: 0.4 mm metal particle.

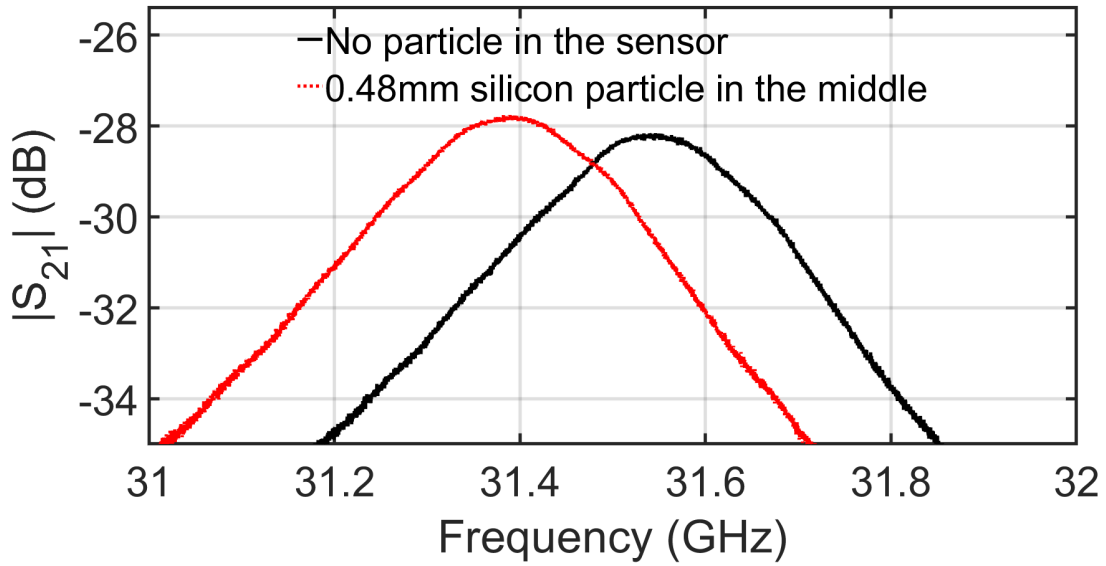

(b) Setup 2 at 30 GHz: 0.48 mm silicon particle.

FIGURE 3.36: Transmission measurements of (semi-)conductor particle in-flow in isopropanol in a glass tube at mm-waves.

TABLE 3.11: Evaluation of particles measured in water at 30 GHz with Setup 2.

particle type	f_r (GHz)			$\lvert S_{21}\rvert$ (dB)		
	no particle	with particle	Δf_r	no particle	with particle	$\Delta\lvert S_{21}\rvert$
0.3 mm ruby	30.698	30.706	0.008	-26.76	-26.84	-0.08
0.4 mm Al_2O_3	30.698	30.724	0.026	-26.80	-26.98	-0.18
0.4 mm metal	30.718	30.686	-0.032	-27.3	-26.2	1.1
0.48 mm silicon	30.699	30.736	0.037	-26.72	-27.04	-0.32

TABLE 3.12: Evaluation of particles measured in isopropanol at 30 GHz with Setup 2

particle type	f_r (GHz)			$\lvert S_{21}\rvert$ (dB)		
	no particle	with particle	Δf_r	no particle	with particle	$\Delta\lvert S_{21}\rvert$
0.3 mm ruby	31.534	31.506	-0.028	-28.06	-27.53	0.53
0.4 mm Al_2O_3	31.536	31.488	-0.048	-28.08	-26.92	1.16
0.4 mm metal	31.556	31.372	-0.184	-28.22	-26.82	1.4
0.48 mm silicon	31.544	31.394	-0.15	-28.22	-27.82	0.4

needed, or the LUT flow speed has to be ideally controlled and should be slow enough to track the particle when the particle is in the center and causes the highest influence on the sensor.

3.4 Resonance frequency stability

A main requirement for material characterization with perturbation is a stable resonance frequency for the unloaded resonator. The only exception is the exact tracking and de-embedding of any other influence than the MUT. The main influences happen because of changing the set-up or the material values of the set-up, such as mechanically or by a changed temperature or pressure.

3.4.1 Temperature and pressure influence

In this section, the ideas behind the temperature influence, and one way to compensate for the temperature with a second mode are explained. The second mode can compensate the temperature influence on the first mode and increase the accuracy of the spectroscopy.

Temperature is a critical factor for permittivity measurements. At first, the temperature is directly influencing the complex permittivity value of every MUT and

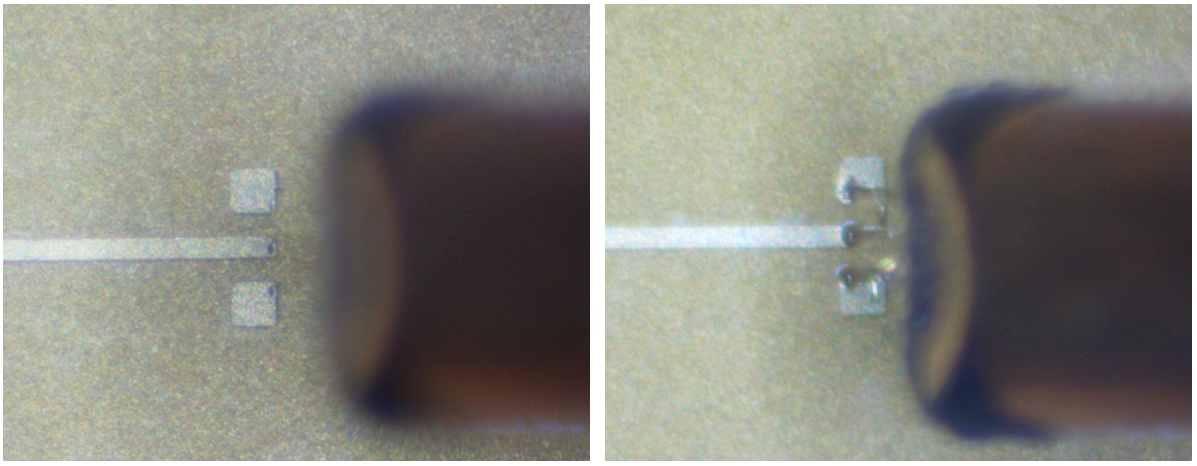

(a) (b)

FIGURE 3.37: Pad and lifted GSG $75\,\mu\mathrm{m}$ probe for determining the temperature influence on the transmission measurement at $190\,\mathrm{GHz}$ with Setup G1 and G2. (a) intact patch with puncture marks of probe. (b) completely scratched and destroyed patch.

significantly of liquids. Second, the temperature changes detune the resonator because of the ceramic's permittivity change and the changed resonator dimensions. Especially the dimensions of the metal parts of the resonator change a lot with the temperature. The ceramic is less affected by dimension changes because of temperature changes [90]. Also, the probes are affected. The results of the dimension change of a probe can be seen in Fig. 3.37.

In Fig. 3.37(a), the pads have only small marks because of the probing of the first S-parameters measurement. The complete pads are scratched and destroyed in the Fig. 3.37(b). The probes increased their length because of the increasing temperature in the labor in the summer from night temperature to midday temperature and scratched with the pins over the whole pads. The transmission measurement results before the pads got destroyed are shown in Fig. 3.38. The transmission results for first mode, which is used for the spectroscopy, are shown in Fig. 3.38(a) and for the second mode in Fig. 3.38(b). Over the day the room temperature change was from $22\,^{\circ}\mathrm{C}$ to $26.4\,^{\circ}\mathrm{C}$. The first mode resonance change is circa $3\,\mathrm{GHz}$ and the second one circa $1.5\,\mathrm{GHz}$ at $|S_{21}| = -30\,\mathrm{dB}$ for only $4\,^{\circ}\mathrm{C}$ temperature change. This frequency shift because of temperature change is bigger than the one caused by variations from MUTs with less than $1\,\mathrm{GHz}$ as in Fig. 3.25. Therefore, temperature control is important for accurate measurements, never mind the danger of destroying the pads or even breaking the probes.

A solution for the inability to control the temperature perfectly, resulting in temperature frequency shift, is to compensate for or calculate the temperature influence.

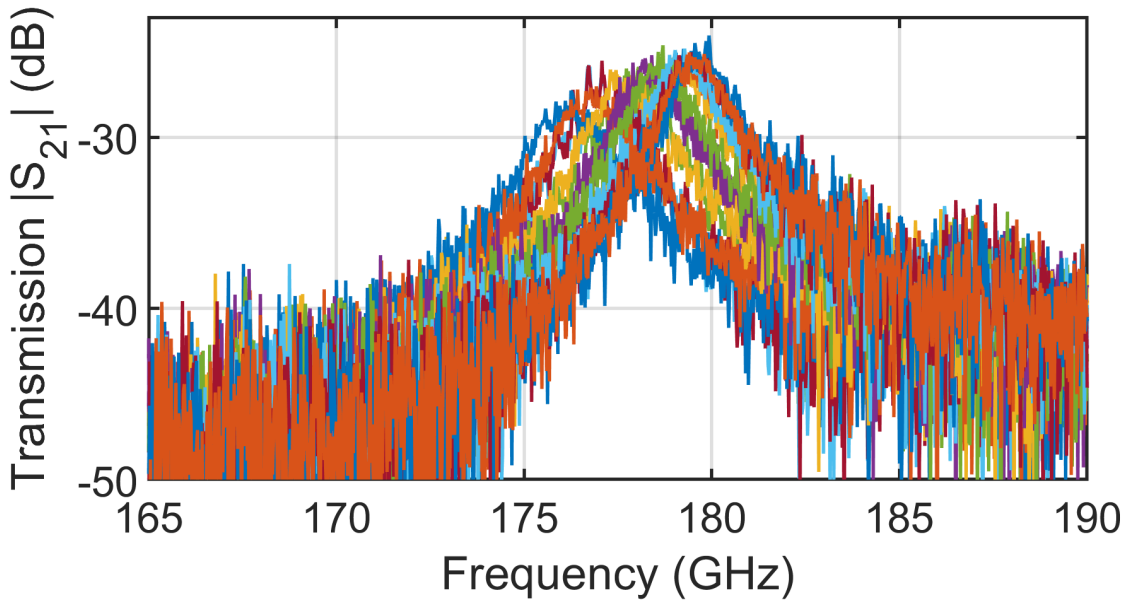

(a)

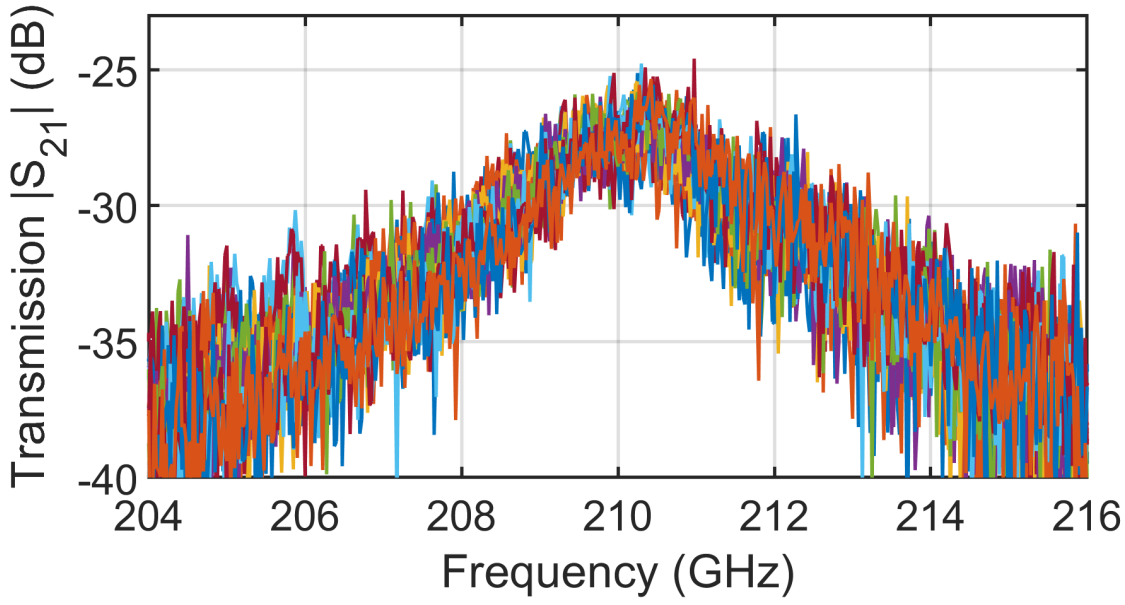

(b)

FIGURE 3.38: Transmission measurement result of Setup G1 with ruby spheres instead of pure alumina for room temperatures from 22 °C to 26.4 °C. (a) first mode. (b) second mode.

A second mode, which has less until no E-field penetrating the MUT and therefore less influenced by the MUT disturbing, can compensate for the frequency shift by temperature change. The E-field modes for Setup 2 as example can be seen in Fig. 3.39 with the same E-field scale. The mode with one E-field maximum penetrating the MUT in the center between the spheres can bee seen in picture Fig. 3.39(a). A second mode with nearly no E-field in the MUT is shown in Fig. 3.39(b).

An approach for this compensation is explained in the following: In Fig. 3.40 Setup 2 scaled to $30\,\mathrm{GHz}$ with $3\,\mathrm{mm}$ diameter alumina spheres is placed in an air-conditioning cabinet. Inside the cabinet, this setup was heated up until $80\,^{\circ}\mathrm{C}$ and tempered at this temperature for at least $1\,\mathrm{h}$ so that all parts of the setup have reached this temperature. Afterward, the cabinet and the setup inside were cooling down passively just by the slow fluctuation of the temperature out of the closed cabinet. This took around $24\,\mathrm{h}$ until room temperature was reached again. Active temperature regulation was not possible because of the cooling compressor of the cabinet. The vibrations of the compressor shake the spheres and detune the resonator. The S-parameters transmission results for Setup 2 at $30\,\mathrm{GHz}$ without tube are shown in Fig. 3.41. In Fig. 3.41(a), there is the full spectrum shown in Fig. 3.41(b) and Fig. 3.41(c) the zoom in for both dominant modes. These results could now be used to correct the temperature influence. The corresponding important values for both modes are in Fig. 3.42, Fig. 3.43 and Fig. 3.44.
At first, the resonance changes of frequency and amplitude over temperature change are analyzed. The frequency shifts over the temperature of both modes are shown in Fig. 3.42(a) and Fig. 3.42(b). The amplitude change at the resonance frequency over the temperature of both modes is shown in Fig. 3.43(a) and Fig. 3.43(b). Last, the corresponding Q-factors over temperature change are shown for both modes in Fig. 3.44(a) and Fig. 3.44(b). Some kinds of trends are recognizable with little deviations or uncertainties. The shape of the first resonance Fig. 3.41(b) is undulating and causes the inaccuracies in Fig. 3.42(a). This shape problem could be solved by using an emulating function fitted on the transmission measurement instead of the transmission by itself to obtain the resonance frequency and amplitude and calculate the Q-factor. Possible models with functions are Debye, Cole-Cole, Cole-Davidson, or Havriliak-Negami model [88, 91, 92].

The outliers in 3.43(a) and 3.44(b) are caused by the different amplitudes of the second mode resonances. What causes or solution for this uncertainty is unclear, or if it should be like this. A small measurement error is always included, too. Further processing steps would be now also to check the transmission results for a setup with a tube and after it with a tube filled with a well-known liquid. Then also, the changes in dimensions of the setup, especially the position of the sphere and tube and the

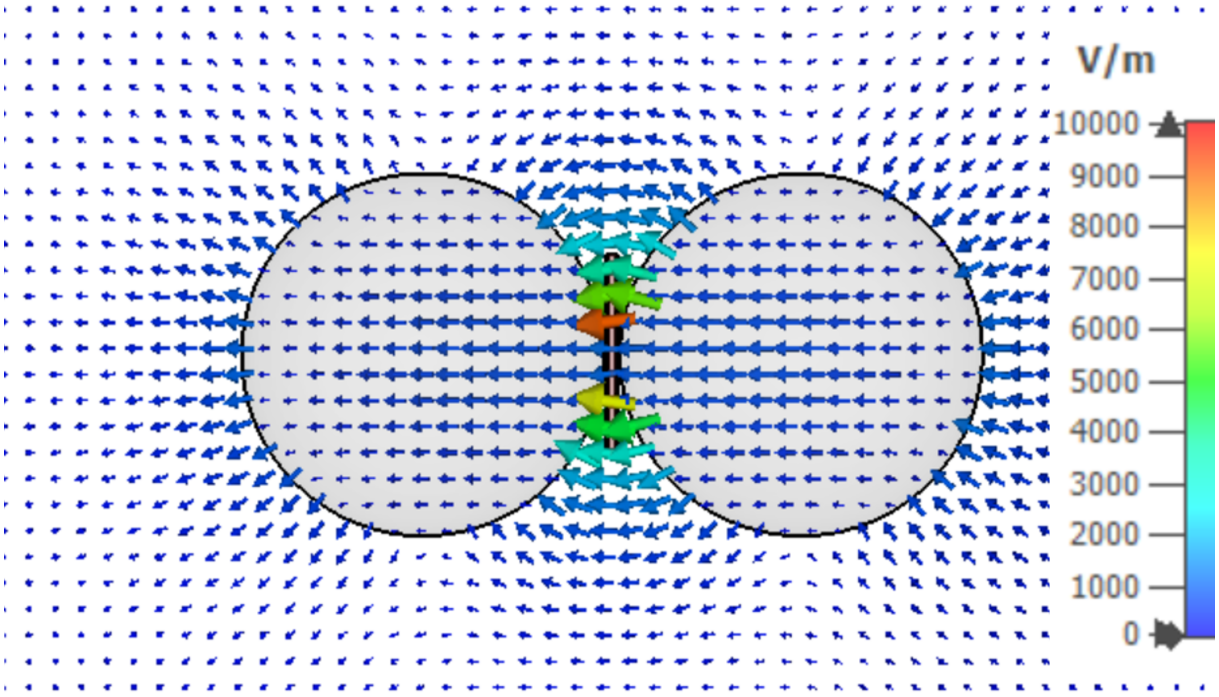

(a)

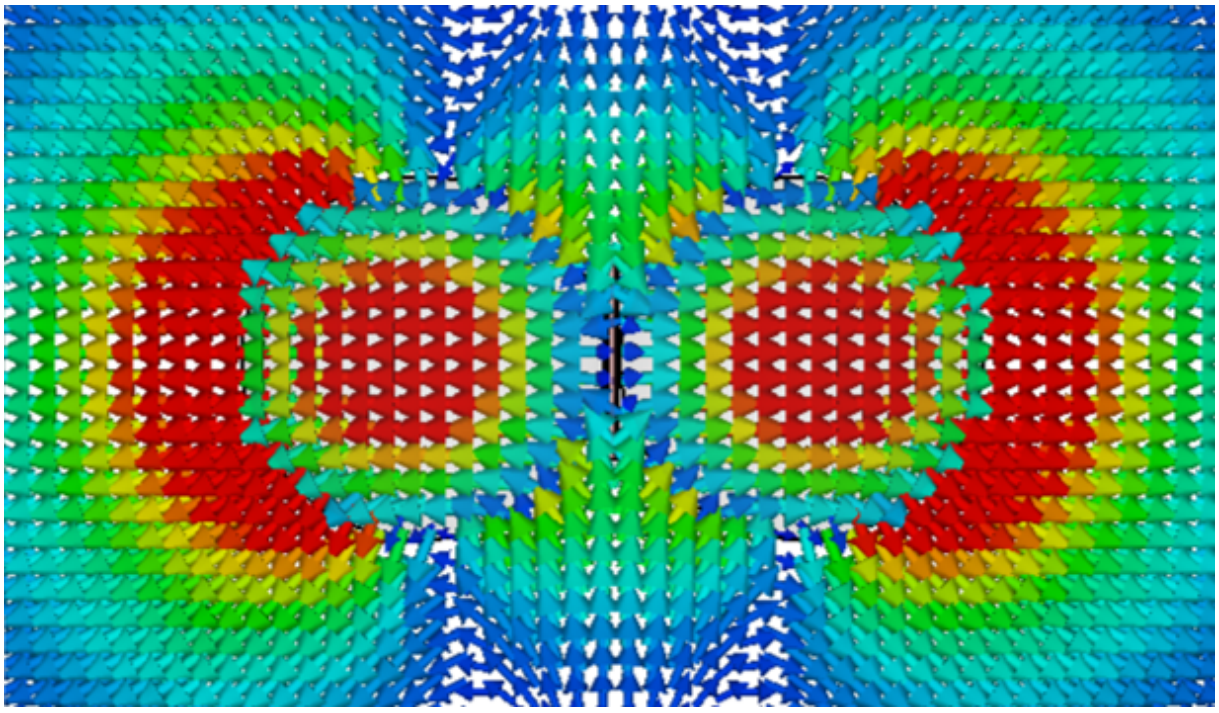

(b)

FIGURE 3.39: Simulated E-field modes of Setup 2 tube filled with air as MUT. Cut parallel to the ground plane at the spheres' center. (a) first mode with E-field maximum in the MUT in the center. (b) second mode with nearly no E-field in the MUT in the center.

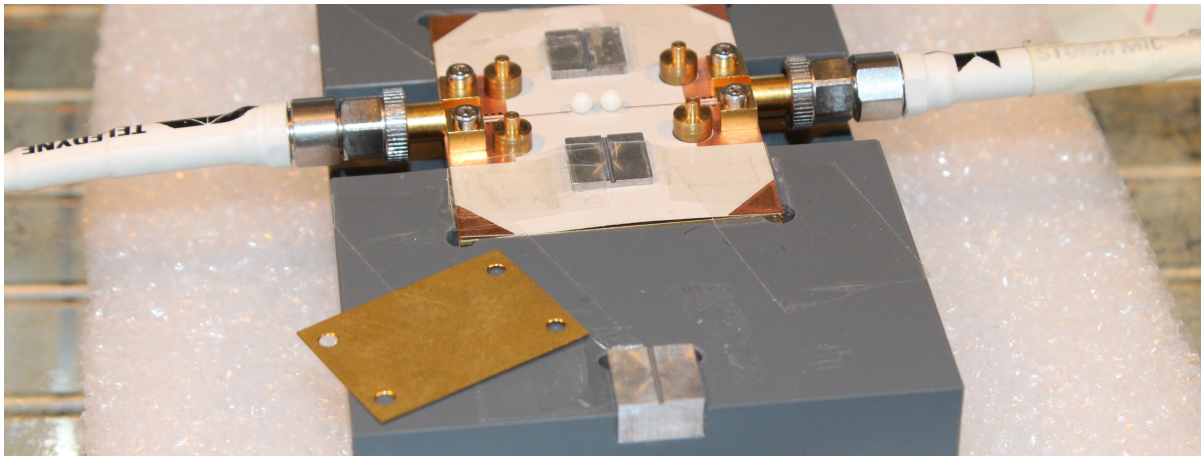

FIGURE 3.40: Setup 2 at 30 GHz without tube inside an air-conditioning cabinet. The top metal plate was removed and positioned in front of the photo.

tube's inner and outer diameter, can be analyzed. These factors significantly impact the resonance, and the inner diameter also influences the active volume of the LUT.

Additionally to the temperature relation between both modes, a MUT relation between both modes is needed. Temperature relation means how much each resonance (frequency, amplitude, and Q-factor) of a mode increased or decreased with which temperature change of the setup compared to the other mode. MUT relation is how much influence the MUT has on each mode compared to the other one. If the temperature relation and MUT relation is different, the second mode can compensate for the temperature influence on the first mode and increase the accuracy of the spectroscopy.

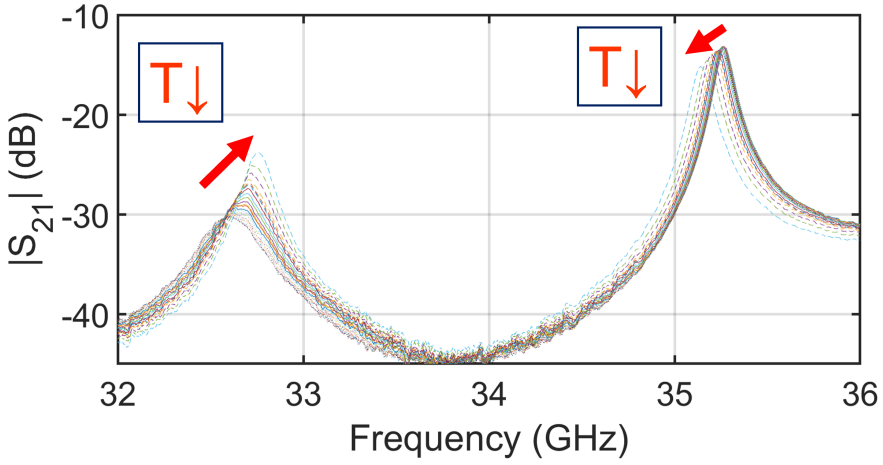

(a)

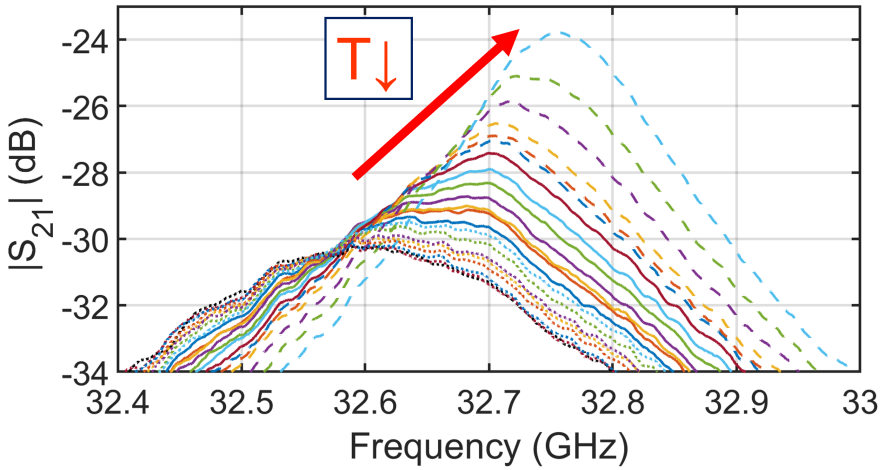

(b)

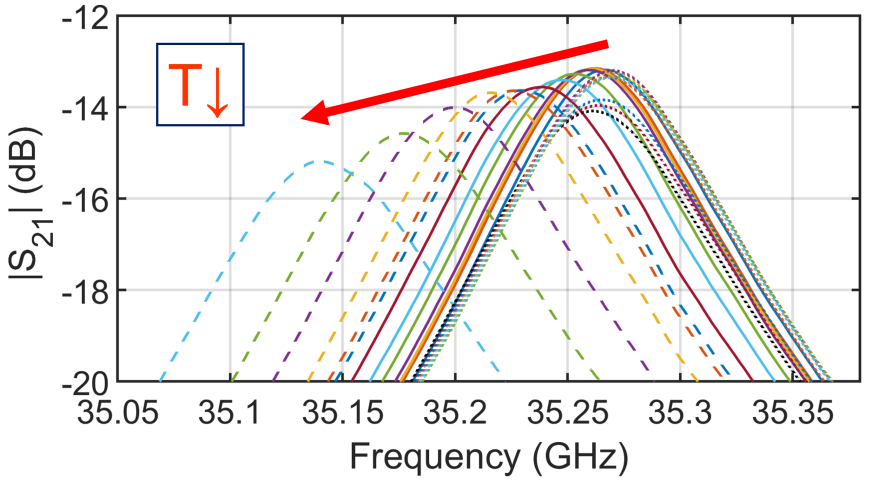

(c)

FIGURE 3.41: Transmission S-parameters measurement result of Setup 2 at 30 GHz for temperatures changes from 80 °C to 29.9 °C. (a) full spectrum. (b) zoom in of first mode. (c) zoom in of second mode.

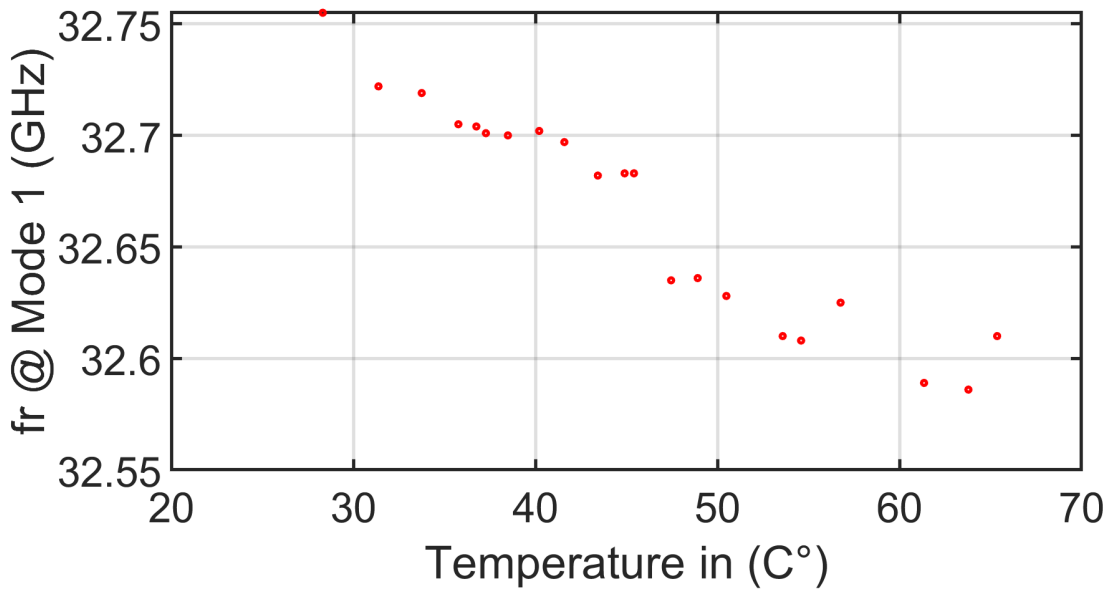

(a)

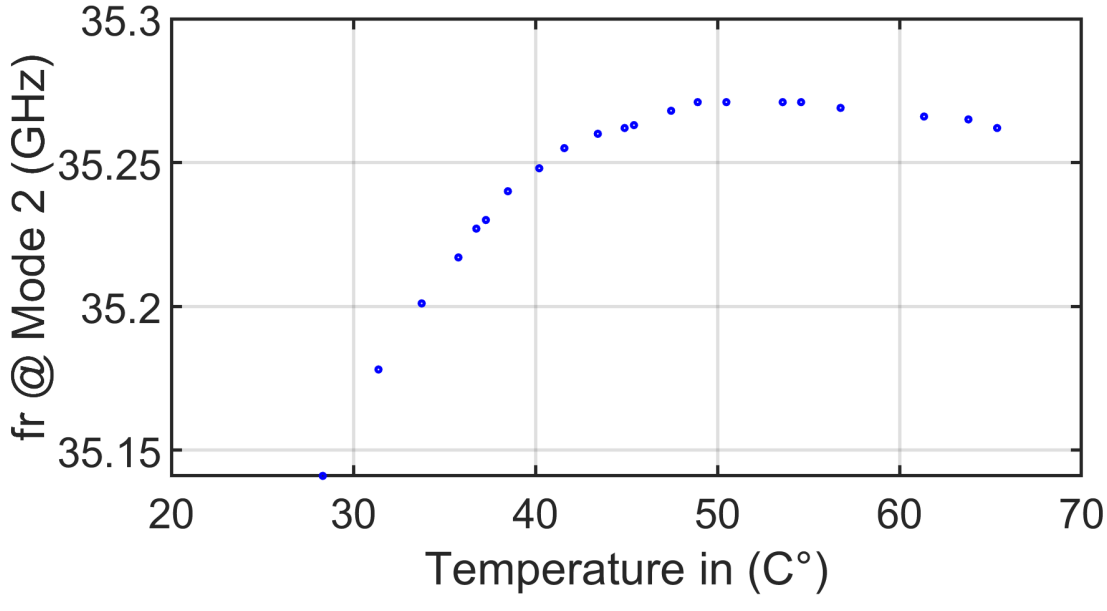

(b)

FIGURE 3.42: Extracted resonance frequency from 3.41 and allocation of exact temperature. (a) resonance frequency of mode 1 over temperature. (b) resonance frequency of mode 2 over temperature.

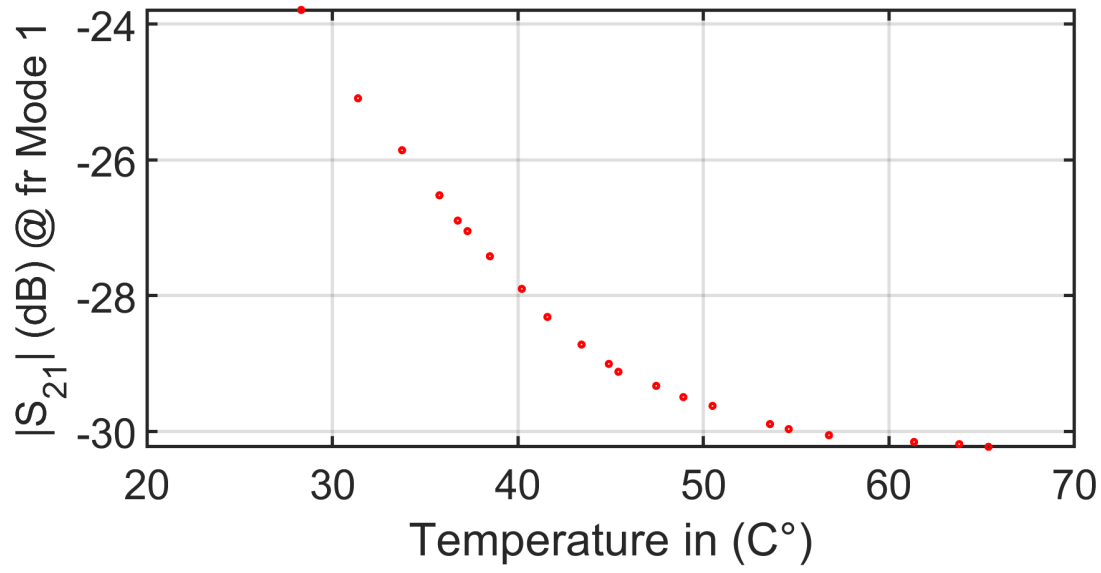

(a)

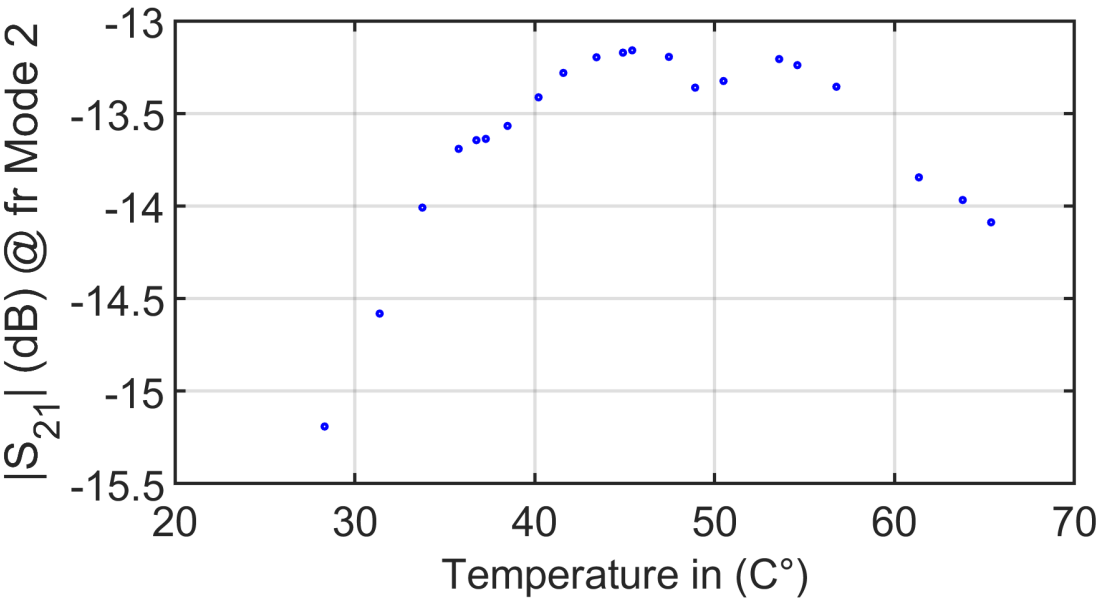

(b)

FIGURE 3.43: Extracted amplitude at resonance frequency from 3.41 and allocation of exact temperature. (a) amplitude at resonance frequency of mode 1 over temperature. (b) amplitude at resonance frequency of mode 2 over temperature.

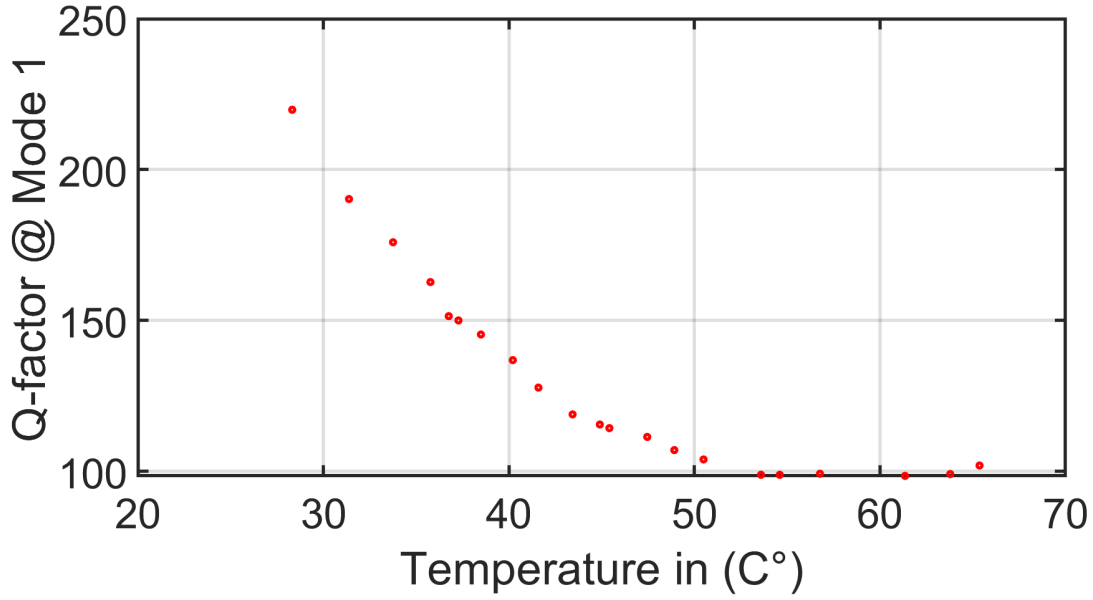

(a)

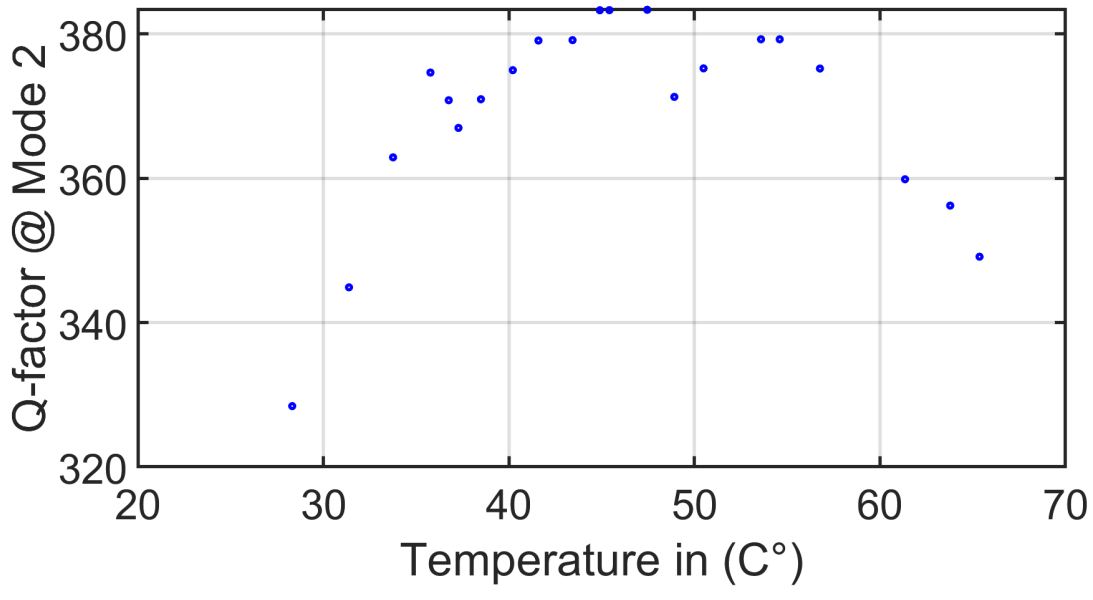

(b)

FIGURE 3.44: Extracted Q-factor at resonance frequency from 3.41 and allocation of exact temperature. (a) Q-factor at resonance frequency of mode 1 over temperature. (b) Q-factor at resonance frequency of mode 2 over temperature.

3.4.2 Comparisons of different sphere feeding methods

The signal coupled in the sphere from an open-end MSTL. There are also other options on how to couple the signal from a cable or WG in the sphere. It can be done with an antenna such as a dipole or horn antenna. Also, it can be done with an open-ended coax cable with a straight extended or looped inner conductor. Also, a resonating patch can be used instead of an open-end MSTL [37].

The reason to use MSTL technology is the simplicity and integrity in a system as on-chip applications and accuracy. Lithography is the most accurate manufacturing process. Therefore the spheres and the feeding are in perfect distance and positions. The reason to use the single line and not the patch is also the sharpness of the transmission resonance peak. It is not necessary to have that strong coupling as it can be obtained with the patch or bandwidth, which can be obtained because of the second resonance of the patch. Instead, it is better for accurate spectroscopy measurements to have the sharpest peak and just enough transmission amplitude so that the resonance peak of the with the lossy LUT filled sensor recognizable to determine the permittivity.

In Setup G2, the open-ended MSTL width was increased because a stronger coupling was needed to be able to sense the used LUTs. A patch was not necessary because enough coupling was created with the increased MSTL width.

3.5 Error estimation, accuracy, and clarity

SDR do have different modes, as we know from the previous section. As long as they do not overlap during the measurement of various MUT there is no problem of unclarity which mode created which resonance peak. A measurement of Setup 1 at microwave over wider frequency range from $5\,\mathrm{GHz}$ to $6\,\mathrm{GHz}$ is shown in Fig. 3.45. Now there are three dominant modes visible. The first at $5.63\,\mathrm{GHz}$, second at $5.83\,\mathrm{GHz}$ and third at $5.85\,\mathrm{GHz}$ for the empty tube. As long as the frequency ranges of the modes do not overlap for different MUTs, we can determine the permittivity of the MUT as before. The problem of overlapping could occur for extremely high permittivity $>> 100$. This would mean we do not know if the resonance peak in the observed frequency range is caused by the second mode, which determines the permittivity, or the third mode. In Fig. 3.45, this observed range in which we expect that the second mode, which is for sensing, should appear is between $5.7\,\mathrm{GHz}$ and $5.84\,\mathrm{GHz}$.

If some extremely high permittivities should be measured or other frequency shifts such as temperature changes could appear and overlapping can not be excluded, there is the option to cut a thin slot in the top metal plate as a mode filter as shown in

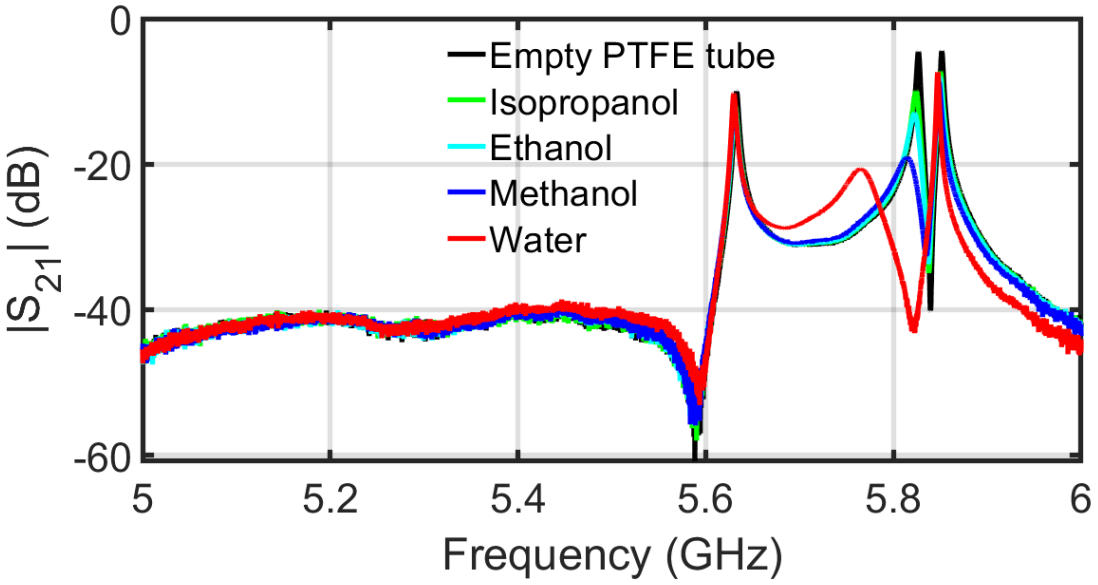

FIGURE 3.45: Measurement results at microwaves with full top metal cover.

Fig. 5.21 in [37]. The position is in the center of the plate over the sphere parallel to the open-ended MSTL feeds with a length of multiple sphere diameters. Fig. 3.46 shows measurement with this cut top metal plate. Now the first and third modes disappeared, and overlapping can be excluded.

3.6 Electrical particle trapping with dielectrophoresis or electrophoresis

During the measurements of the particles with the microwave setups and the mm-wave setups, the particles aligned themselves in the center between the spheres after they were pumped close to the center. This phenomenon also appeared with the opened resonator. There is also a very weak transmission without a metal cover, which was strong enough to create enough force on the perceptible particle. The perfect center alignment of the particle in Setup 3 can be seen in Fig. 3.47. In Fig. 3.47(a) a silicon sphere with $0.48\,\mathrm{mm}$ diameter and in Fig. 3.47(b) a ruby sphere with $0.3\,\mathrm{mm}$ diameter are held in the center between the resonator spheres. Also, pumping the particles away from the center took more pressure than just pumping them through the tube at any other position. The particles seem to be held in position by force, some electrical force created by the E-field. It seems that is dielectrophoretic force [73, 93]. Whether the particle also changed its z-position in the tube to be in the center from all three axes was not seeable. Most works use strong electrical fields with a few Volts to a

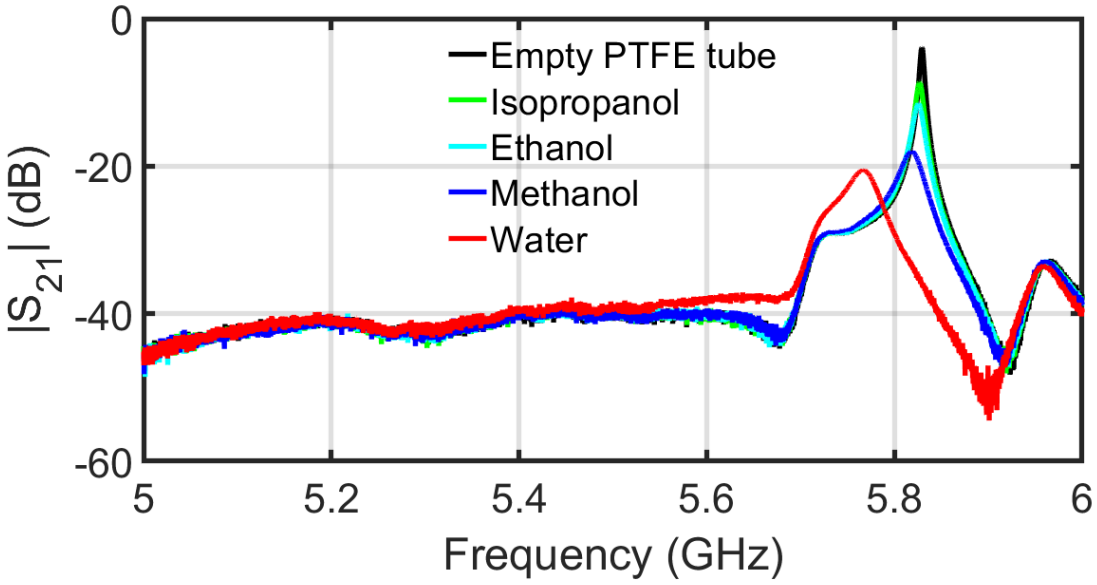

FIGURE 3.46: Measurement results at microwaves with a cut slot in the top metal cover.

few hundred Volts and static fields or alternating E-field with kHz to MHz range, but not in the GHz range as in this work [93–96]. A good overview of this topic gives the research paper [93].

In Setup 2, it is just a relatively weak changing E-field created by the VNA, but it is still working to trap particles. Further investigations have to be done about which mode is responsible for the trapping, which role the water has as a medium, or which other carrying liquid could be used. Especially concerning measurement of living cells in liquid or the particle size compared with the wavelength. Also it has to be considered which field strength causes which liquid pressure resistance, or is there also another mode which could be used to push the particles away from the center, or for which applications could this kind of electric force also be used.

(a)

(b)

FIGURE 3.47: Electrical trapped spheres in Setup 3 with opened metal cover plate and glass tube. (a) ruby sphere with $0.3\,\mathrm{mm}$ diameter. (b) silicon sphere with $0.48\,\mathrm{mm}$ diameter.

Chapter 4

State of the art: silicon chip application

[1] In this chapter the spherical dielectric resonators at millimeter-wave frequency in and on the BEOL of silicon chips is explained. MMICs have the significant advantage of being compact and having less loss than circuits on different boards linked together because everything was on the same board, and no transition to another board is needed. The tricky part is now to use silicon for MMIC.

The most commonly used material for chips is silicon. For most applications, it is a good choice. For mm-wave systems, silicon technology does have a few problems. A big one is the high loss for circuits with integrated passive components. The loss-creating points are the thin BEOL, dielectric as metal layers, and high lossy doped silicon under the BEOL. Therefore, creating high Q resonators is challenging. High Q resonators are essential to building oscillators with low Phase Noise (PN). Antennas also suffer from these substrate conditions.

In Fig. 4.1 is the idea of combining a dielectric sphere with silicon chips illustrated using the example of an antenna. The most straightforward antenna realization is to use the thin BEOL in blue, the SiO_2 with a stack of metal layers inside, and ignore the thick doped silicon. One solution to increase the antenna efficiency was to use LBE to remove the lossy doped silicon under the antenna (see middle illustration). With the now generated thick substrate, the antenna radiation efficiency improves. This is state of the art of silicon on-chip application with $130\,\mathrm{nm}$ especially SiGe. The new method in the right illustration to use a dielectric sphere instead of LBE to increase the radiation will be explained in the chapter 5. This section presents how the state of the art tries to solve these challenges, starting with filters.

4.1 Filters

In this section, the state of the art of MMIC filters on a silicon chip is lightened.

[1] The content of this section refers to the paper [25].

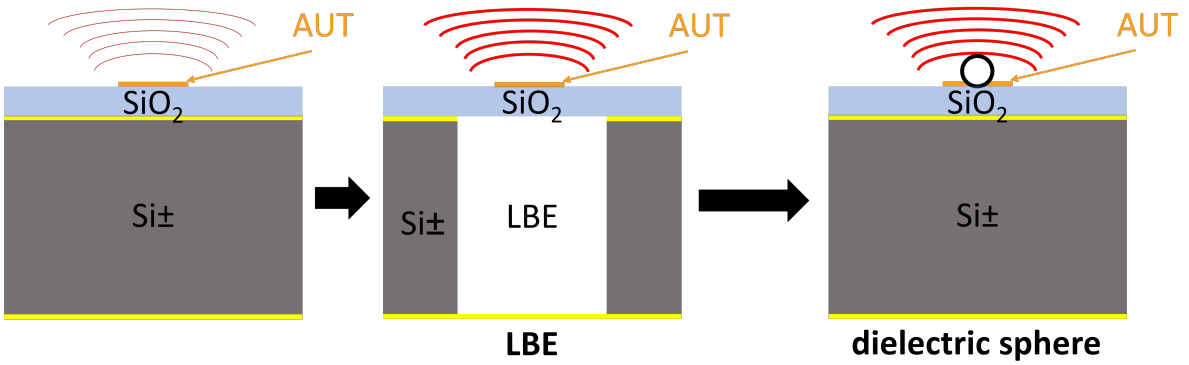

FIGURE 4.1: Illustration of solutions for on-silicon-chip antennas not to scale: LBE compared to a dielectric sphere. Metal layers are golden; the BEOL is the blue SiO_2. Grey is the doped silicon. The radiating element is on top of the SiO_2, and the red curved lines indicate the radiation. The black-surrounded white circle is a dielectric sphere.

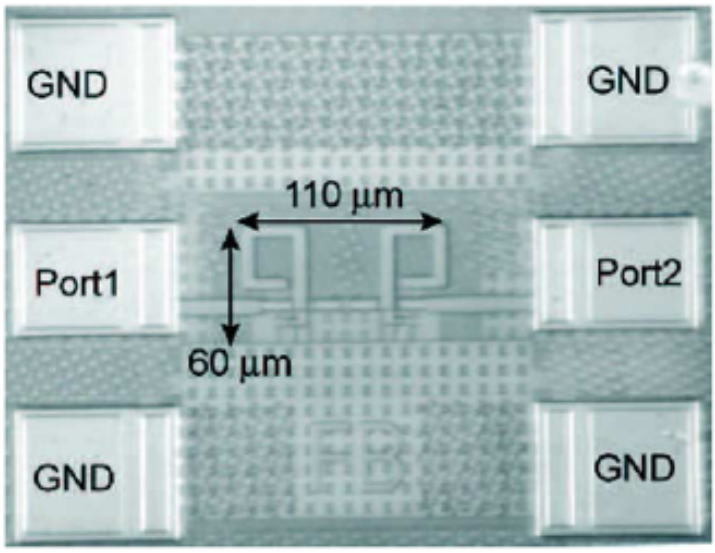

FIGURE 4.2: Photo of lumped element filter on SiGe chip [13].

Lumped element filter

The most straightforward filter type is with lumped elements, as in Fig. 4.2 [13]. The lumped elements are integrated inductors realized with spirals and capacitors realized with metal-insulator-metal capacitors. The center frequency is at $77.3\,\mathrm{GHz}$ with $12\,\mathrm{GHz}$ bandwidth. The filter consists of a serial connection of MSTL recess as capacitance, a loop as inductance to ground, MSTL recess, another loop, and MSTL recess.

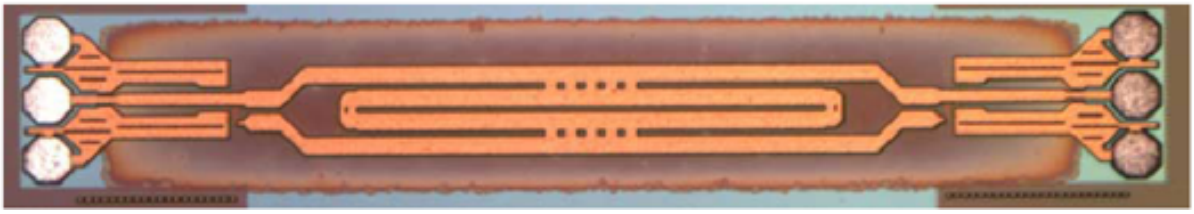

FIGURE 4.3: Planar filter using edge coupled lines with LBE [14].

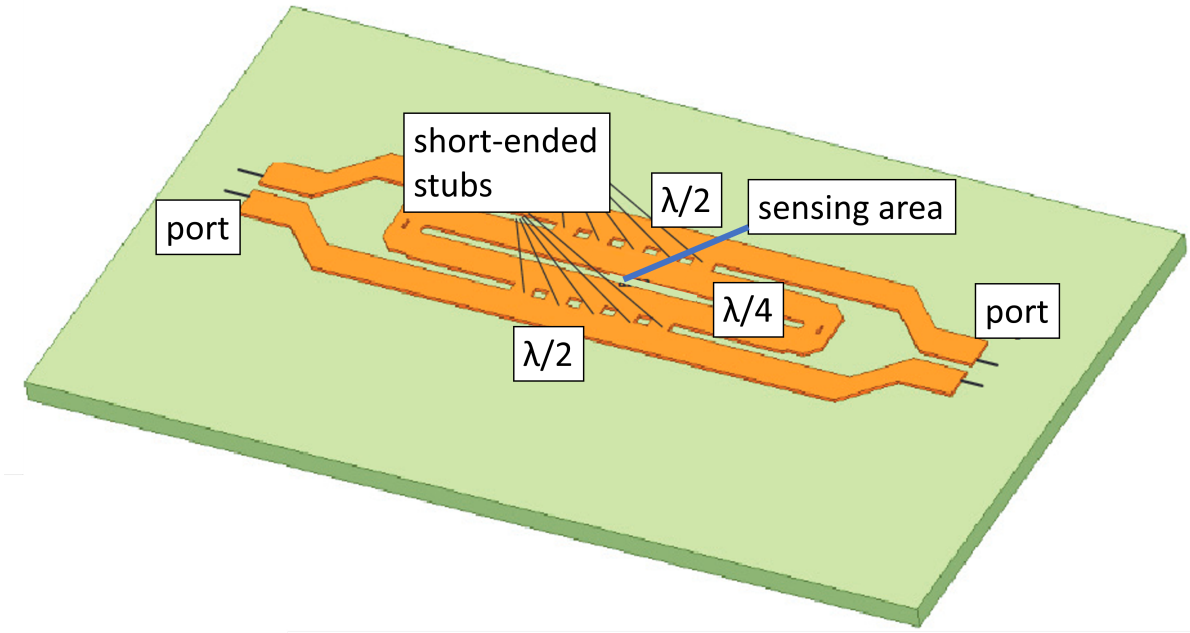

FIGURE 4.4: Planar filter with edge coupling lines on-chip adapted after [15].

Planar filter with edge coupled lines

The next filters are planar resonators with edge coupling lines, as in Fig. 4.3 and Fig. 4.4 [14, 15].

The filter in Fig. 4.3 uses LBE. The length of the lines and the gaps are responsible for the filter characteristics. The center frequency is 120 GHz with 11 GHz bandwidth. The loaded Q-factor is 11 for the simulation without silicon and 7 for the measured filter with LBE at 130 GHz [14].

The filter in Fig. 4.4 is working similarly as in Fig. 4.3 and is without LBE. The working frequency is at 240 GHz, and the filter has more than 80 GHz bandwidth resulting in a Q less than 3.

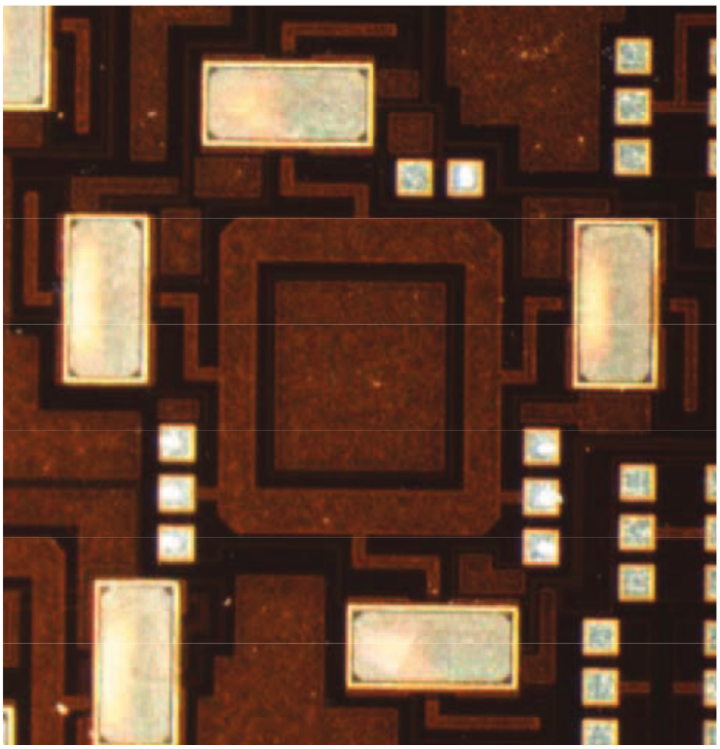

FIGURE 4.5: Photo of ring-based filter with tunable capacitive MEMS on SiGe chip [16].

Ring-based filter tunable with MEMS

In Fig. 4.5, a ring-based filter tunable with capacitive changing MicroElectroMechanical System (MEMS) is presented. The line lengths of each side are $90°$ transmission lines and create the filter characteristics [16]. The measured center frequency is $74\,\mathrm{GHz}$ with circa $8\,\mathrm{GHz}$ resulting in a Q of 9 [16].

4.2 Antennas

The collection of the different types and varieties of Dielectric Resonator Antenna (DRA) is presented in [97] until the year 2010 and in [98] until 1994, including rules for design relations to adjust resonance frequency and bandwidth. A work that explores the limits of the aesthetic possibilities of DRA with a glass swan and apple as a radiating element is [99].

The first dielectric resonator antenna on-chip with a high conducting silicon substrate was presented for the IBM SiGeHP5 process with a ceramic cylinder as a resonator and is working at $28\,\mathrm{GHz}$ [100].

There are already many different types of antennas on silicon chips presented. In [101] and [102], there are overviews about the state-of-art of the on-chip antennas at the mm-wave frequencies. In this chapter, the state of art antennas on silicon chips

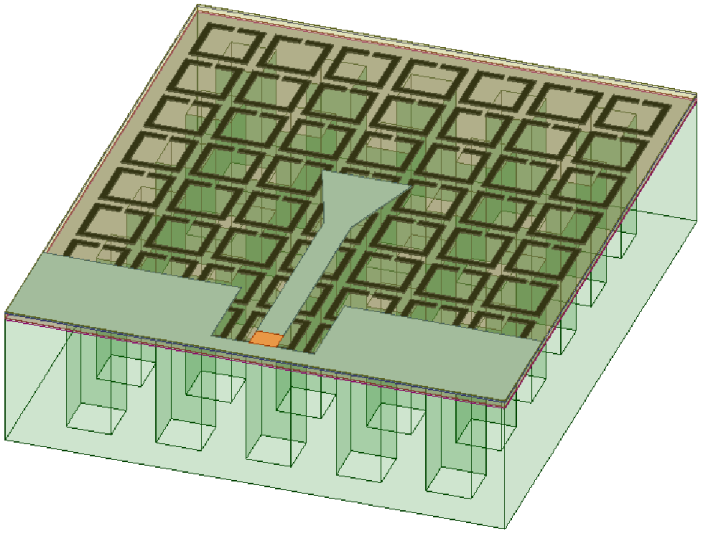

FIGURE 4.6: Simulation model of on-chip monopole with AMC and LBE [17].

with similar conditions such as substrate height and frequency as the SDRAs produced with the $130\,\mathrm{nm}$ BiCMOS SiGe process SG13G2 at $\approx 100\,\mathrm{GHz}$ are presented.

Monopole antenna

The first antenna to present is a monopole in Fig. 4.6 [17]. In Fig. 4.6 are the split rings on metal layer TM1 visible. This is the Artificial Magnetic Conductor (AMC) and reduces the substrate loss with constructive reflections. The AMC is combined with the LBE to maximize the radiation efficiency. This results in a peak gain of $2.29\,\mathrm{dBi}$ at $83\,\mathrm{GHz}$ [17].

Bowtie-slot antenna

The second antenna to consider is the bowtie-slot antenna shown in Fig. 4.7 [18]. This bowtie-slot antenna has used an array of back-to-back E-shaped Frequency Selective Surface (FSS) instead of AMC. This results in a peak gain of $-1.94\,\mathrm{dBi}$ at $94\,\mathrm{GHz}$ [18].

A slot bowtie, a fractal bowtie, and a half-cloverleaf stacked Vivaldi antenna are compared in. The highest gain antenna of these is the bowtie-slot antenna shown in Fig. 4.8 [19]. The operating frequency is $180\,\mathrm{GHz}$ with a peak gain of $<5\,\mathrm{dBi}$.

Folded-dipole antenna

In Fig. 4.9 a folded dipole with LBE that do not reduce the mechanical stability is presented [20]. Therefore, a trade-off was made by not reaching the maximum gain

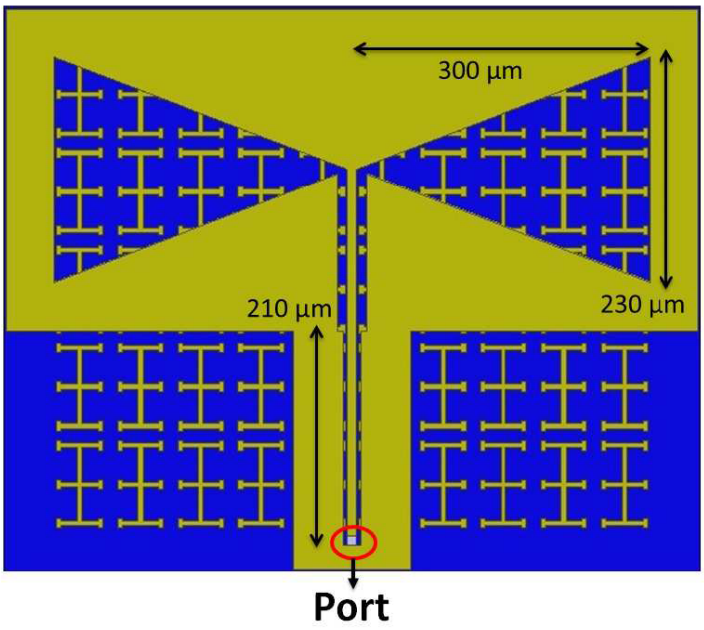

FIGURE 4.7: Simulation model of on-chip bowtie-slot antenna with FSS [18].

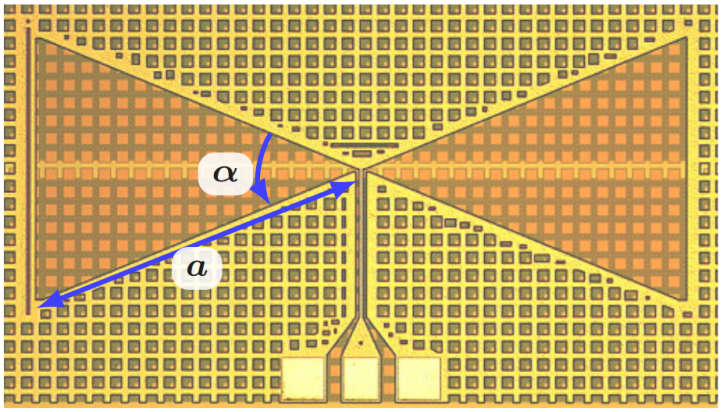

FIGURE 4.8: Photo of on-chip bowtie-slot antenna [19].

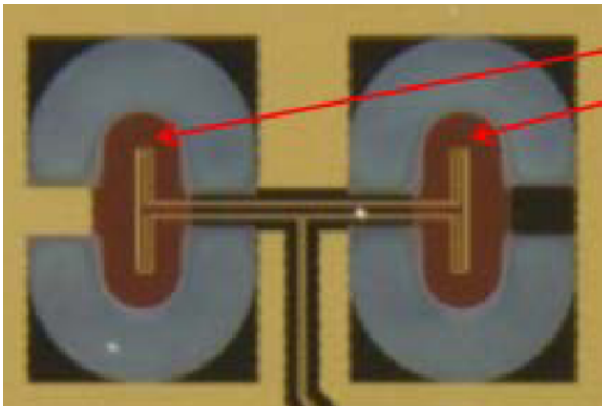

FIGURE 4.9: Photo of on-chip folded-dipole antenna with LBE [20].

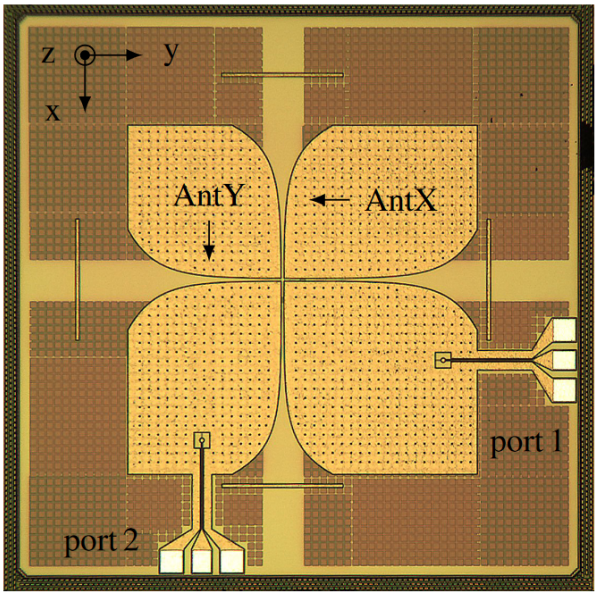

FIGURE 4.10: Photo of on-chip Vivaldi antenna with LBE [21].

and bandwidth but having higher mechanical stability by removing just a small silicon area under the antenna. The folded dipole is working at 122 GHz and has a peak gain of 6 dBi.

Vivaldi antenna

A dual-polarized on-chip Vivaldi antenna from [21] is depicted in Fig. 4.10. The simulated peak gain is 5 dBi at 180 GHz [21].

Patch antenna

One of the most commonly used antennas is the patch antenna. A rectangular BEOL on-chip version is shown in Fig. 4.11 [22]. This patch antenna was compared with the state of art literature until the publishing of the antenna with the smallest radiating element area for on-chip antennas at similar frequencies. It has a peak gain of 2.6 dBi and its resonance frequency is at 192.3 GHz [22].

Dielectric resonator antenna

Last, there is the dielectric resonator antenna [23]. A Yagi-Uda-like antenna with a resonance frequency at 340 GHz is shown in Fig. 4.12. The antenna is built up as a stack. At the bottom is a SIW resonator in the BEOL. The next layer is a low permittivity supporter topped with a cubic dielectric resonator as director. The peak gain is ≈10 dBi [23].

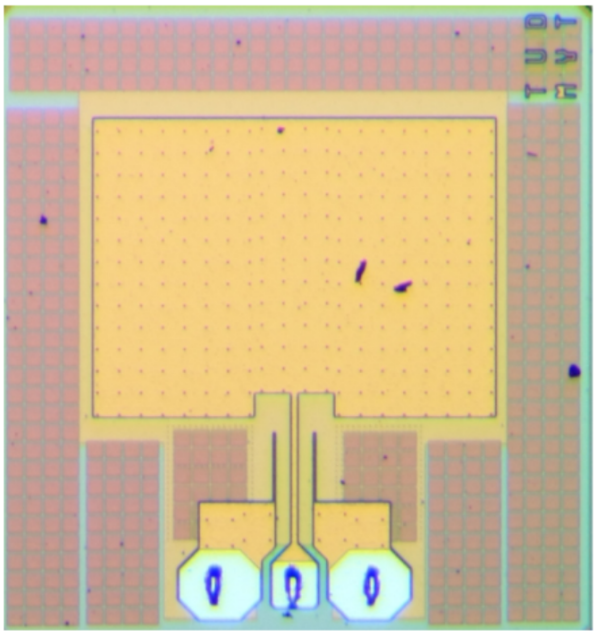

FIGURE 4.11: Photo of on-chip patch antenna with [22].

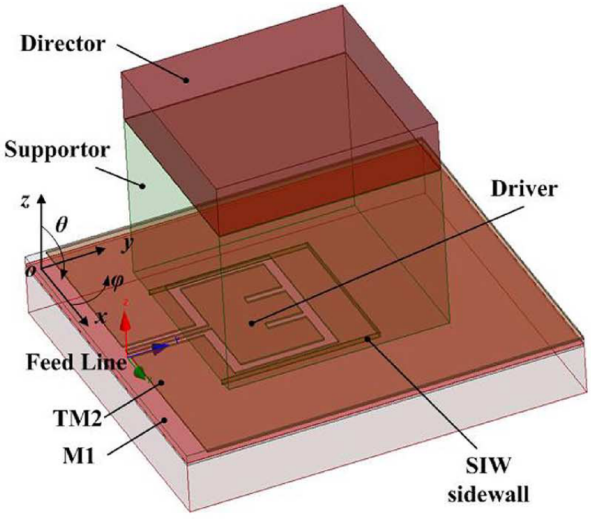

FIGURE 4.12: Photo of on-chip dielectric resonator antenna [23].

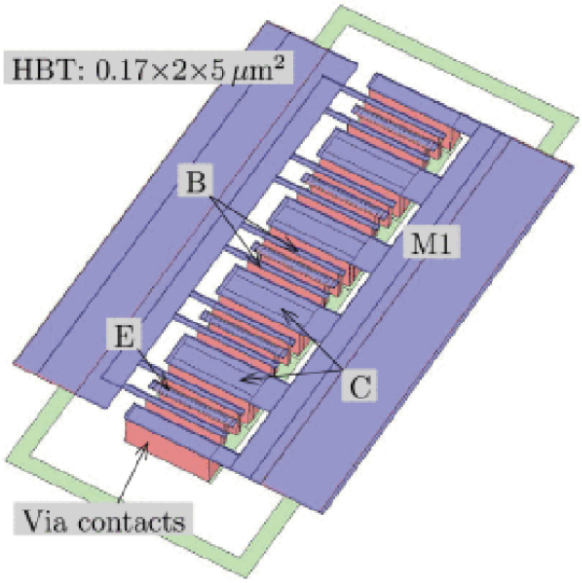

FIGURE 4.13: Core details of the heterojunction bipolar transistor contacts of the voltage controllable Colpitts oscillator [103].

4.3 Oscillators

Oscillators especially dielectric ones are used to generate high-frequency signals. In this thesis, the focus is on the passive parts, especially the filter. The active parts corresponding to the presented VCO with dielectric spheres in section 5.3 are explained in detail in publications by Yu Zhu from the Chair of Circuit Design and Network Theory at the University of Dresden. A comparison of different design methods and architectures for VCOs at subTHz frequencies is given in [103]. The picture of the corresponding resonator is shown in Fig. 4.13 [103]. One of the first ones, who put a DR on a silicon chip as a filter for an oscillator and is working at mm-wave with circa 55 GHz was [104]. Associated works are [105–109]. The first one who used a sphere as DR for a VCO and tuned the resonance of the dielectric resonator and not just the circuit is [110]. In this thesis, the results and the build-up of a VCO with a SDR at 100 GHz are enlightened.

Chapter 5

SiGe applications

This chapter explains why to use a sphere instead of LBE and how this was done as illustrated in Fig. 4.1. One way to solve the problem with the thin substrate height and the high lossy doped silicon under the BEOL is LBE. At LBE, the doped silicon under the structure is removed. Therefore, a thin, air-filled, perfect low-loss substrate is received. The problem with the LBE is an elaborate and time-consuming process. Another solution is to build silicon on-chip applications such as antennas, filters, and oscillators with good performance. The solution is to use a dielectric sphere as a resonator. It is already proved that these SDR antennas, filters, and oscillators perform very well for mm-wave [10, 28, 110].

[1] The used standard silicon technology for the circuits is SG13G2 of IHP (IHP GmbH, Frankfurt (Oder), Germany) [24]. The BEOL definition is shown in Fig. 5.1. The BEOL consists of 7 metal layers in SiO_2. Under the SiO_2 is the doped silicon, which has low resistivity. The metal layer between doped silicon and oxide is M1. M1 is used as ground and shielding for the silicon bulk. The distance from M1 top side to the highest layer TM2 top side is $12.8\,\mu\mathrm{m}$ [24]. A new process step has been added now. A crate was etched in the BEOL to the top of M1. This crate for the SDRA is shown in Fig. 5.2. The chip is only partially planarized [7]. Therefore the crate depth is about $11\,\mu\mathrm{m}$. This is the distance between the transparent top surface, when TM2 is not present, and M1. In this crate, the dielectric spheres for the antenna, resonator, and oscillator are placed.

At first, the SDR as antenna passive as 1-port and active 4-port with four patches each feed from an own amplifier is explained and evaluated. After it follows SDR filter and tunable filter. At last, the VCO is presented.

[1] The content of this section refers to the paper [25].

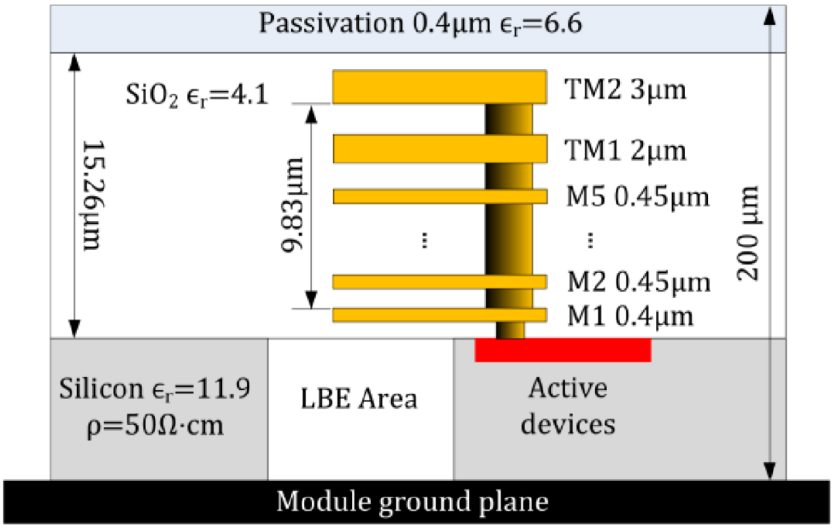

FIGURE 5.1: BEOL of SG13G2 layer description [24]. The chips in this work are not planarized, are thicker than 200 um, and do not have LBE.

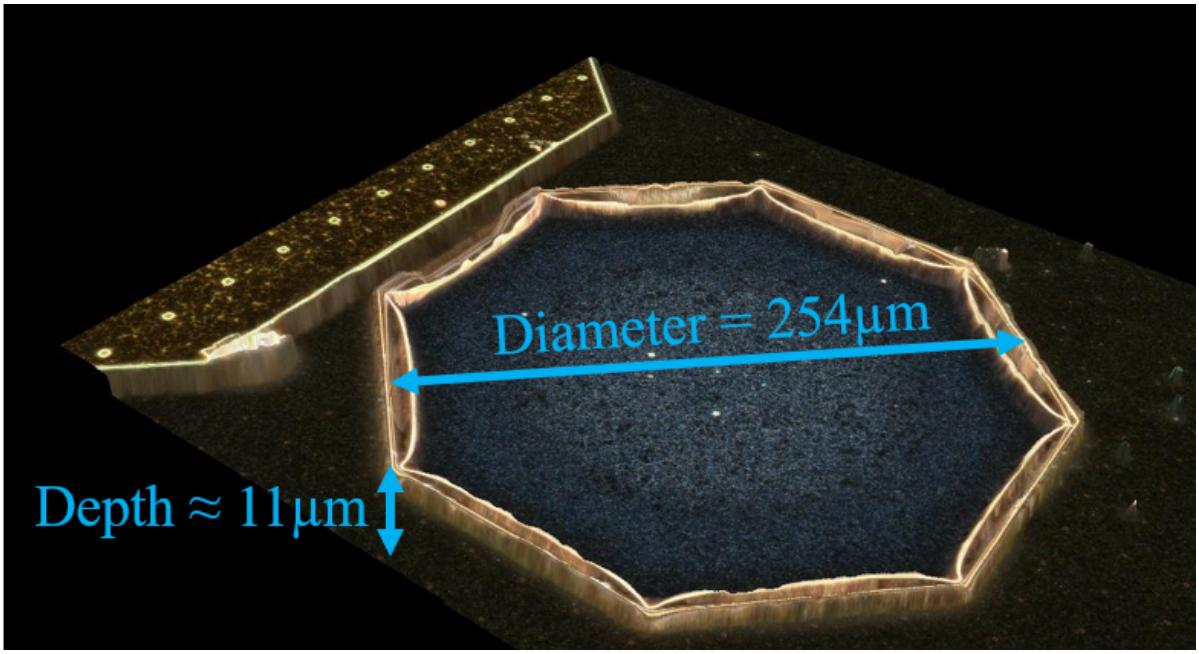

FIGURE 5.2: Photo of crate in BEOL of the SiGe chip for a 1.1 mm sphere.

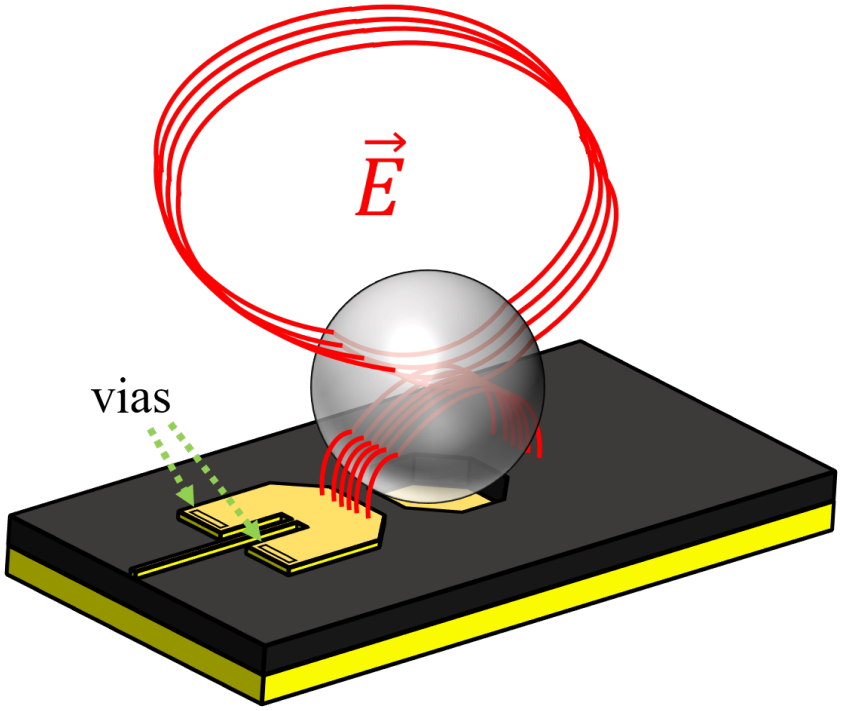

FIGURE 5.3: Illustration of working principal of on-chip SDRA [25]. Ground and MSTL metal is golden; the substrate is black. In the crate in the middle is a gray ceramic sphere placed as a resonator. A quarter-wave patch is used instead of an open-ended line because of stronger coupling. The important E-field lines are visualized with red lines.

5.1 SDR antenna on SiGe

There are different kinds of on-chip antennas for silicon, also dielectric resonator antennas [100]. They all have problems related to a lossy substrate or extra LBE process and need a lot of chip area or mechanical alignment precision. The solution is the SDRA normally operating in a higher-order mode. This was first presented operating at mm-wave in [28]. In Fig. 5.3, the working principle of the on-chip SDRA is illustrated [25].

The radiation essential electric fields are illustrated with red lines. The E-field couples from the open end edge of the MSTL quarter-wave patch resonator to the sphere. The quarter-wave resonator increases the bandwidth and strength of the coupling compared to a single line. The E-field detaches perpendicular to the top surface and is linearly polarized in extension to the MSTL.

An important detail is the final stage of the back-end-of-line process etched crate shown in Fig. 5.2. Precise and safe positioning is possible only if the crate fits the sphere diameter and the BEOL height. The alumina ceramic sphere used for the antennas has a diameter of $1.1\,\mathrm{mm}$ and a permittivity of $\epsilon_r = 9.8$. The dimensions of the corresponding octagon-shaped crate were measured with a laser microscope. The depth is circa $11\,\mu\mathrm{m}$,

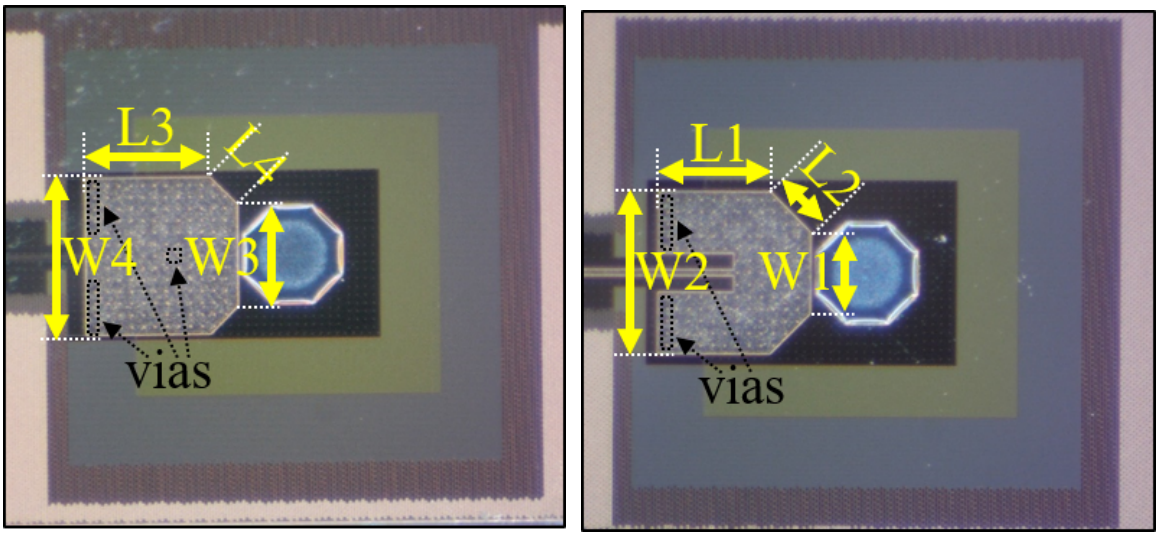

(a) (b) [25]

FIGURE 5.4: Photo of the two one side fed SDRA with a patch, octagon-shaped crate, and no sphere. The left side of the patches is grounded with vias. (a) feed on TM1 with vias. $L3 \approx 317.865\,\mu\text{m}$, $L4 = 98.995\,\mu\text{m}$, $W3 = 260\,\mu\text{m}$, $W4 = 400\,\mu\text{m}$. The width of MSTL is $6\,\mu\text{m}$ and the four vias as feed are at $339.865\,\mu\text{m}$ measured from the edge next to W4 in direction to the crate. (b) feed on TM2. $L1 = 278\,\mu\text{m}$, $L2 = 141.421\,\mu\text{m}$, $W1 = 200\,\mu\text{m}$, $W2 = 400\,\mu\text{m}$. Width of MSTL is $14\,\mu\text{m}$.

the top diameter is $254\,\mu\text{m}$, the bottom diameter is $230\,\mu\text{m}$, which results in a slope angle of the wall of circa $45°$ [25, 111].

There are now three SDRAs. Two with a patch feed from one side and one with a feed from all four sides. The two single side fed antenna without spheres are shown in Fig. 5.4. The patch in Fig. 5.4(a) is fed with a via from the bottom between TM1 (MSTL) and TM2 (patch). The patch in Fig. 5.4(b) is fed with a MSTL, and the patch is cut for impedance match. The signal is transmitted from the VNA over a GSG probe with $100\,\mu\text{m}$ pitch to the antenna and received with an open-ended rectangular WG placed $16\,\text{mm}$ above the chip surface in the center of the sphere. This setup is used for the free-space transmission measurement of the antennas. The transmission measurements and the reflection results are shown in Fig. 5.5. The fitting simulations are also included. Simulations and measurements of the transmission and reflection behave similarly and fit together. The probes are calibrated at the touching point for the reflection S_{11} measurement. This means the $990\,\mu\text{m}$ long feeding line for the TM2 antenna from the line end touching the patch to the probe tips and $1140\,\mu\text{m}$ long line from probe pads to the via for TM1 is included in the measurement. The transmission measurement is without any calibration and includes the signal path from VNA, WGs, probe, MSTL feeding, antenna, free space path, receiving open WG, WGs and back in the VNA.

There are two measurements for every antenna to distinguish. The first measurement is with a sphere, which means the antenna is SDRA and gives the blue and black curve. For the second measurement, the sphere is removed, meaning the antenna is now just a patch antenna. Patch and SDRA have the same linear polarization and similar vertical beam direction. This measurement and simulation results are the red and purple curves. The difference of the transmission of the TM2 antenna in Fig. 5.5(b) is as expected. The transmission with the sphere is higher than without. The difference is the gain difference of $5.8\,\mathrm{dB}$ at $100\,\mathrm{GHz}$, between SDRA and a patch antenna. The simulated directivity of just the quarter-wavelength patch is $6.5\,\mathrm{dBi}$ with $7\,\%$ efficiency at $100\,\mathrm{GHz}$ (resulting in $-5.05\,\mathrm{dBi}$) when a feed with 0 length is assumed. The simulated directivity of the SDRA is $9.9\,\mathrm{dBi}$ with an efficiency of $33\,\%$ (resulting in $3.22\,\mathrm{dBi}$). This means the gain difference with and without a sphere is approximately $8.8\,\mathrm{dB}$. This $8.8\,\mathrm{dB}$ simulated gain difference are $3\,\mathrm{dB}$ more than the measured difference. The reasons are that the SDRA is not radiating as well as simulated because of mismatch, as not perfectly aligned spheres, and sphere size variations Additionally, the positioning of the receiving open-ended rectangular WG antenna during the measurement was not accurate enough to hit the gain maximum and the right orientation. These are the main reasons for the gain difference differences between simulation and measurement.

Now for the TM1 antenna transmission in Fig. 5.5(a) from $97\,\mathrm{GHz}$ to $100\,\mathrm{GHz}$ is the behavior not as expected. The transmission with and without a sphere is nearly the same, and at $99\,\mathrm{GHz}$, the transmission is even stronger without a sphere. One explanation could be a detuning of the patch, which means miss-matching of the antenna, which results in a worse transmission. Another explanation could be that the angle of the beam maxima has changed, and the receiving antenna has to be positioned differently. The minimum of the reflection can not be taken as the ideal working frequency of the antenna because of the high loss. This resonance minimum can also occur because of higher loss. Therefore the transmission difference between with and without spheres is more expressive.

The comparison of the SDRAs of this work (TM1) and TM2 from [25] and the state-of-art is in Table 5.1. The efficiency is calculated as the fraction of gain and directivity. TM2 gains nearly as much as the folded dipole with the extra process step of localized backside-etching [20]. It also reaches the gain of the Vivaldi antenna with an $44\,\%$ smaller wavelength [21]. How high the gain of the SDRA would foreshadow the DRA with tripled frequency and therefore relative triple substrate height [23].

The sphere could also be fed with two patches on opposite sides balanced fed [28] or also rotated 90° around the sphere center combined to a tilted linear or a circular polarization [111].

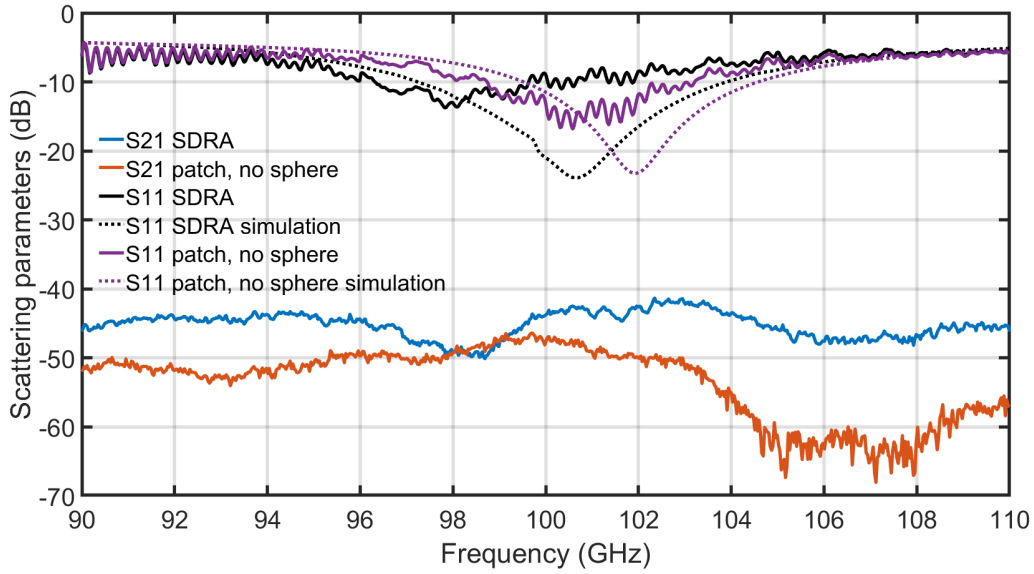

(a)

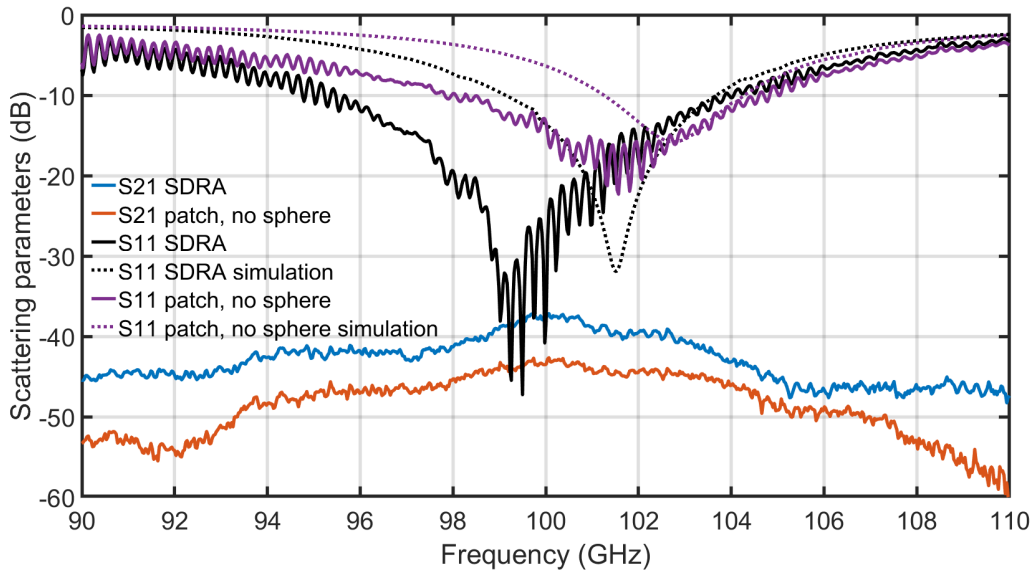

(b)

FIGURE 5.5: Measurements and simulations of the on-chip spherical dielectric resonator antenna. (a) TM1 (fed) antenna. (b) TM2 (fed) antenna.

TABLE 5.1: Comparison of state-of-the-art antennas on silicon chips in the range of 100 GHz with the SDRA.

Ref	Gain [dBi]	Efficiency	f [GHz]
Monopole (LBE) and (AMC) [17]	2.29 (sim)	/	83
Bowtie-Slot (FSS) [18]	-1.94 (sim)	/	94
Folded dipole [20] (LBE)	6	54%	122
Slot-Bowtie [19]	<5	/	180
Vivaldi-taper antenna [21]	5 (sim)	/	180
Patch [22]	2.6 (sim)	22%	192.3
DRA [23]	10	80%	340
This work: SDRA feed on TM1	4.5 (sim)	33%	100
This work: SDRA feed on TM2 [25]	4.7 (sim)	36%	100

The third antenna is the 4-port antenna with one sphere, four patches around the sphere, and an extra amplifier structure for each patch. This is one of the lowest-loss possibilities to create a 1:4 power divider or combiner. In Fig. 5.6, the phase shift between the antennas is 90° and leads to circular polarization. It can already be noted that this antenna is matched directly to a complex input impedance to reduce the ohmic loss because of an extra matching network structure and is also working at circa 100 GHz.

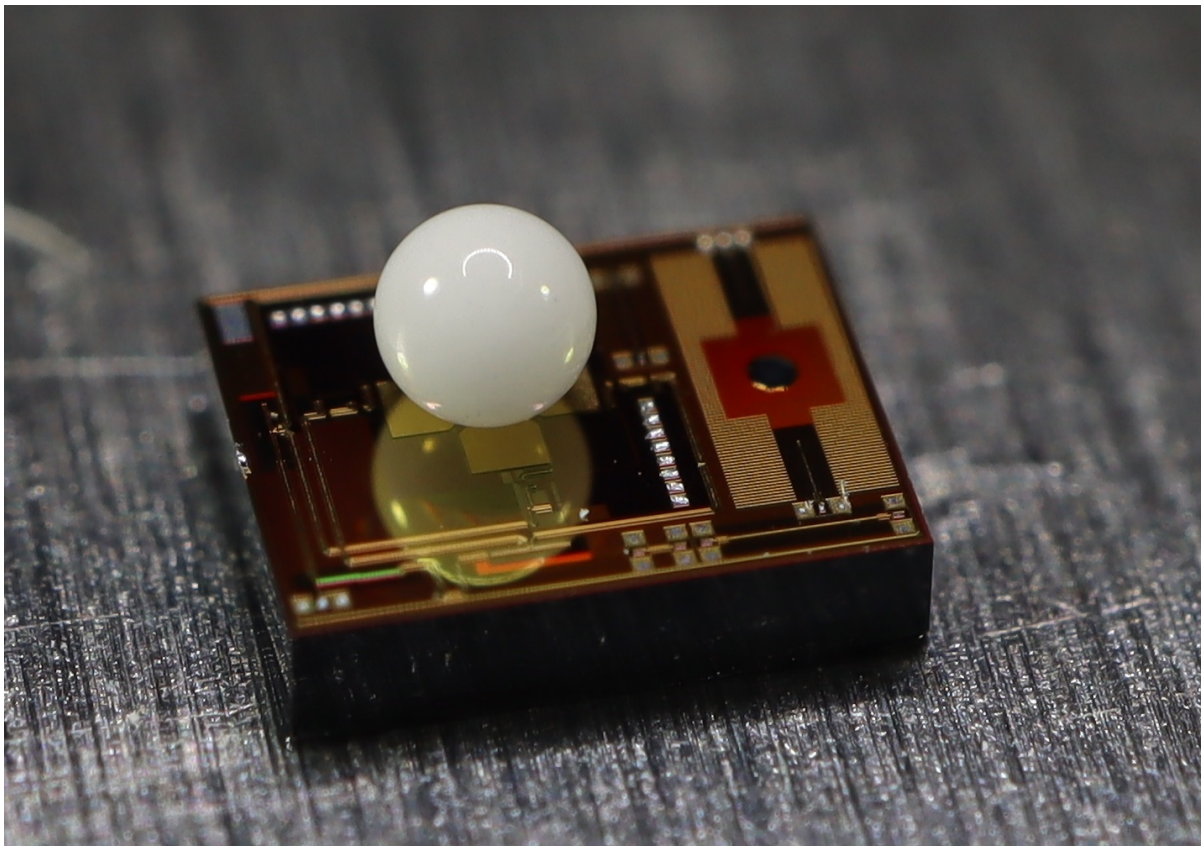

FIGURE 5.6: Photo of 4-port antenna with $1.1\,\mathrm{mm}$ diameter ceramic sphere on the SiGe chip-circuit.

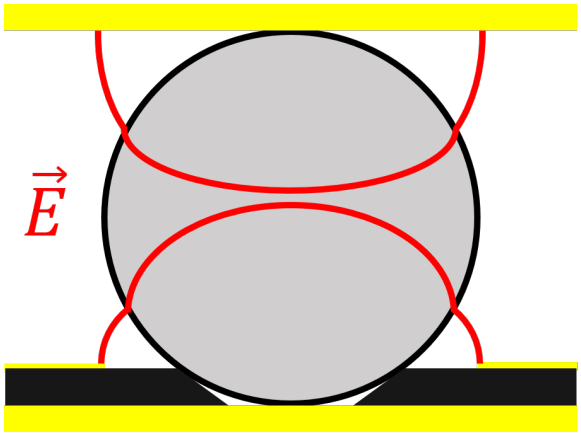

FIGURE 5.7: Side view on illustration of working principal of on-chip SDR [25]. Ground and MSTL metal as the sandwiching top cover is golden, and the substrate is black. In the crate in the middle is a gray ceramic sphere placed as a resonator. The important E-field lines are visualized with red lines.

5.2 SDR filter on SiGe

In Fig. 5.7, the working principle of the on-chip SDR is illustrated [25]. The E-field (red line) couples inside the sphere from an open-end MSTL. The sphere is sandwiched between the top metal cover and the bottom metal ground of the MSTL. On the opposite sides, the E-field also couples loose from the sphere in the other open-end transmission line. The width of the MSTL is $10.5\,\mu\mathrm{m}$ and the open-end is $137\,\mu\mathrm{m}$ away from the closest edge of the etched crate. A $1\,\mathrm{mm}$ diameter Al_2O_3 sphere with $\epsilon_r = 10.15$ is used [10]. The crate for this sphere has an upper inner circle diameter of $241\,\mu\mathrm{m}$ and $226\,\mu\mathrm{m}$ lower diameter. The resonator is measured on-chip also as the antenna with a GSG probe with a $100\,\mu\mathrm{m}$ pitch and a network analyzer [25].

The critical characteristic of a transmission filter with a single transmission peak is the Q-factor. The chart with the transmission measurement, which is used for the Q calculation and simulations results, is in Fig. 5.8. At first, the chip was glued on an alumina metal plate for the probe measurement (Fig. 5.8 blue curve). This scenario is now a SDR filter with a restricted size of the surrounding ground metal and the top metal cover. Therefore, this results in a measured transmission Q of 53. The reasons for this low Q compared to the Q of 1800 in [10] are not only the higher loss of the materials and lower substrate height but also the tiny dimensions of both sandwiching metal plates facilitate sidewards radiation leakage. Another reason is the chip thickness of $730\,\mu\mathrm{m}$ including more than $700\,\mu\mathrm{m}$ thick high-loss bulk silicon to which the field of the resonator is exposed. The field wraps around the chip edges and causes loss in the bulk silicon.

A solution to increase the Q is shown with another similar chip. This chip was

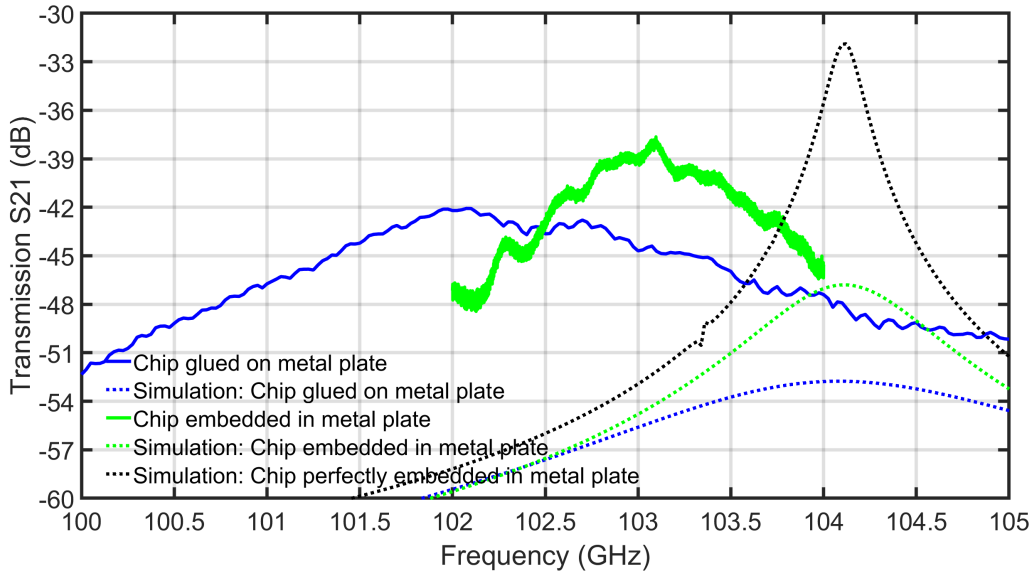

FIGURE 5.8: Transmission measurement and simulation results of the on-chip SDR [25].

embedded inside an aluminum plate. Therefore, pockets were milled in the metal plate, and the chip was glued inside so that the top of the chip was flush with the plate top, as shown in Fig. 5.9. This increased the Q now to 143 (Fig. 5.8 green curve). Because of the production tolerances, there are little trenches with $20\,\mu\mathrm{m}$ to $60\,\mu\mathrm{m}$ width between the chip and the top of the metal plate. Also, there are big drilling holes at the corners of the chip. This is good to see in Fig. 5.10. At last, a simulation of a perfect setup with no trenches and enough big metal plates was done (Fig. 5.8 black curve). This results in a Q of 536. This value goes to the amount of the in [10] reached Q of 1800 at $103\,\mathrm{GHz}$ with a $24\,\mu\mathrm{m}$ thick low-permittivity substrate thin-film circuit. As the SDR sensor presented in this work, also the SDR filters are affected by the sphere position, orientation, and surrounding temperature. Therefore, the resonance frequency of the measurement moves, too.

These values are now compared with the state of art filters for silicon at around $100\,\mathrm{GHz}$ in the Table 5.2. No big comparison of the Q-factor is necessary. The SDR filter is way beyond the state of art filters even for the unloaded Q factor Q-unloaded $= Q_U$ calculated with (1.13).

5.3 Voltage tunable SDR filter

The chip with the tunable SDR was once glued on a metal plate as in Fig. 5.11 and the other time embedded in an aluminum metal plate to increase the surrounding metal and therefore the Q-factor and transmission of the SDR [25]. A photo of the

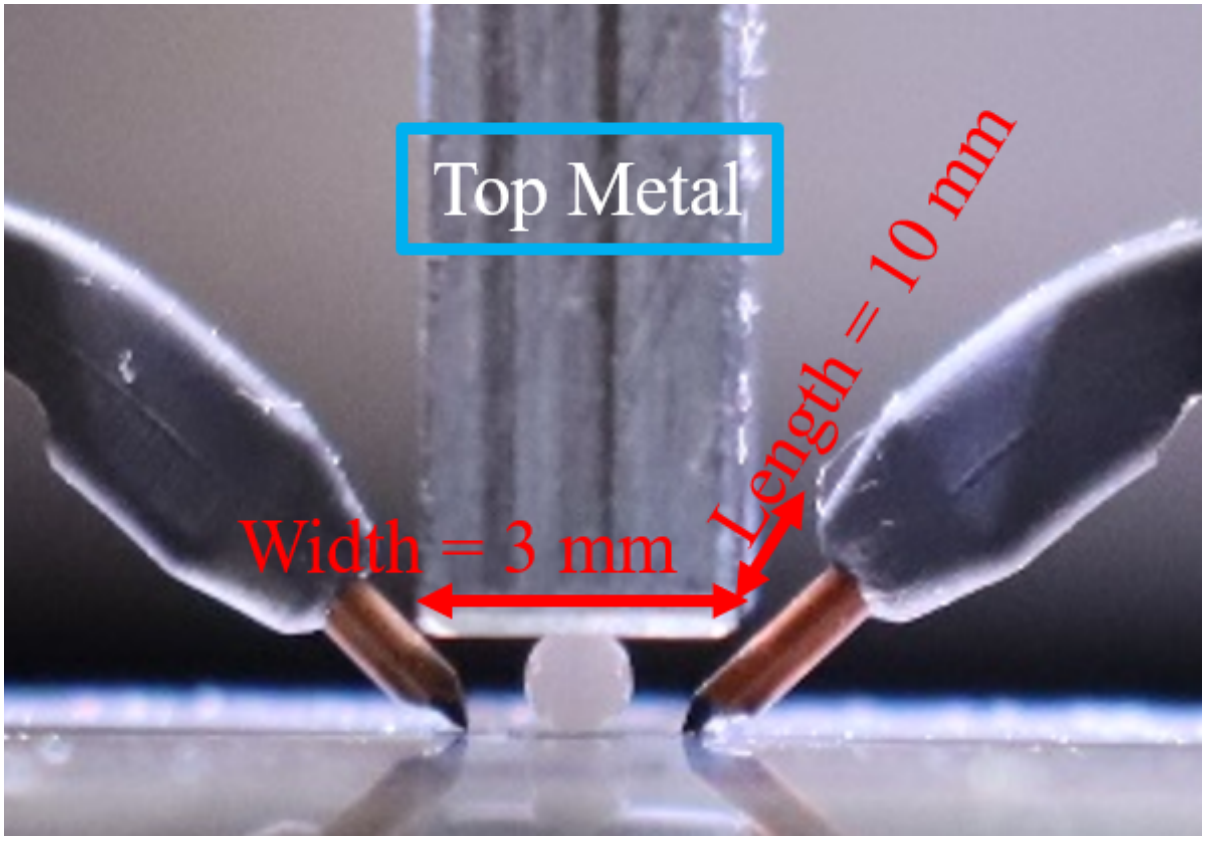

FIGURE 5.9: Photo from the side of the resonator with the covering top metal sandwiching the ceramic sphere. The test chip is embedded in a milled pocket of an alumina plate, and the probes are attached to the chip [25].

TABLE 5.2: Comparison of state of the art silicon filters at around 100 GHz with the SDR filters.

Ref	Q-factor	Q-unloaded	at f [GHz]
Filter with lumped elements [13]	19 (sim/meas)	34	77
Planar, edge coupled lines [14]	11(no Si)(sim), 7(LBE)(meas)	30, 14	130
Planar, edge coupled lines [15]	<3 (sim)	6	240
Ring-based filter tunable with MEMS [16]	9 (meas)	17	74.2
This work: chip glued on plate [25]	53	53 (meas)	102.3
This work: chip embedded in plate [25]	143	145 (meas)	103.1
This work: chip perfectly embedded [25]	536	549 (sim)	104.12

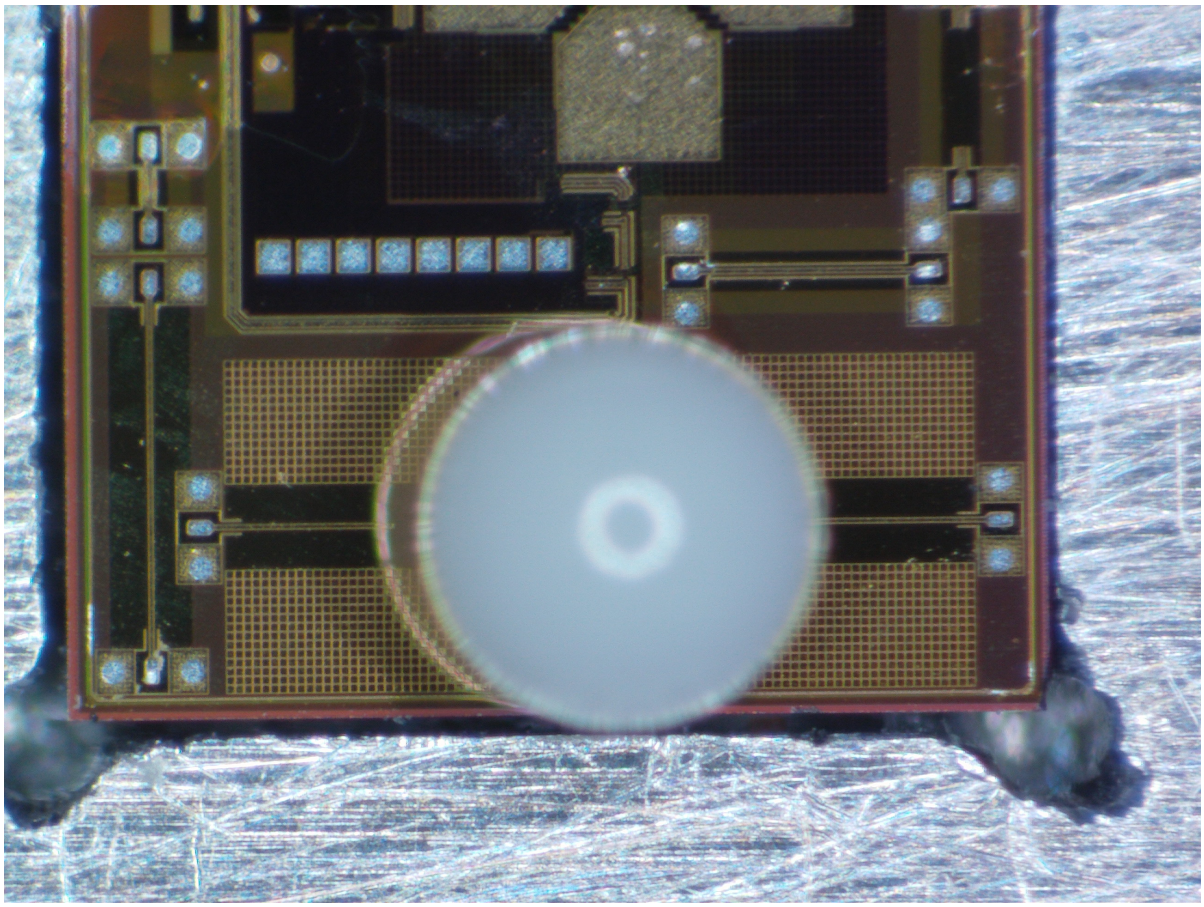

FIGURE 5.10: Photo from the top of the resonator test chip. The test chip is embedded in a milled pocket of an alumina plate. The covering top metal is removed for the picture [25].

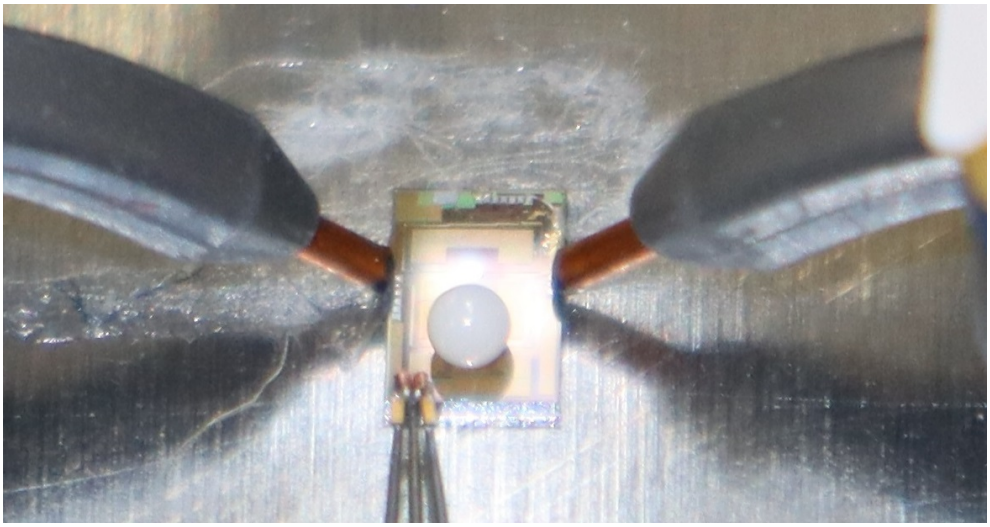

FIGURE 5.11: Photo of setup voltage tunable SDR. The top cover was removed.

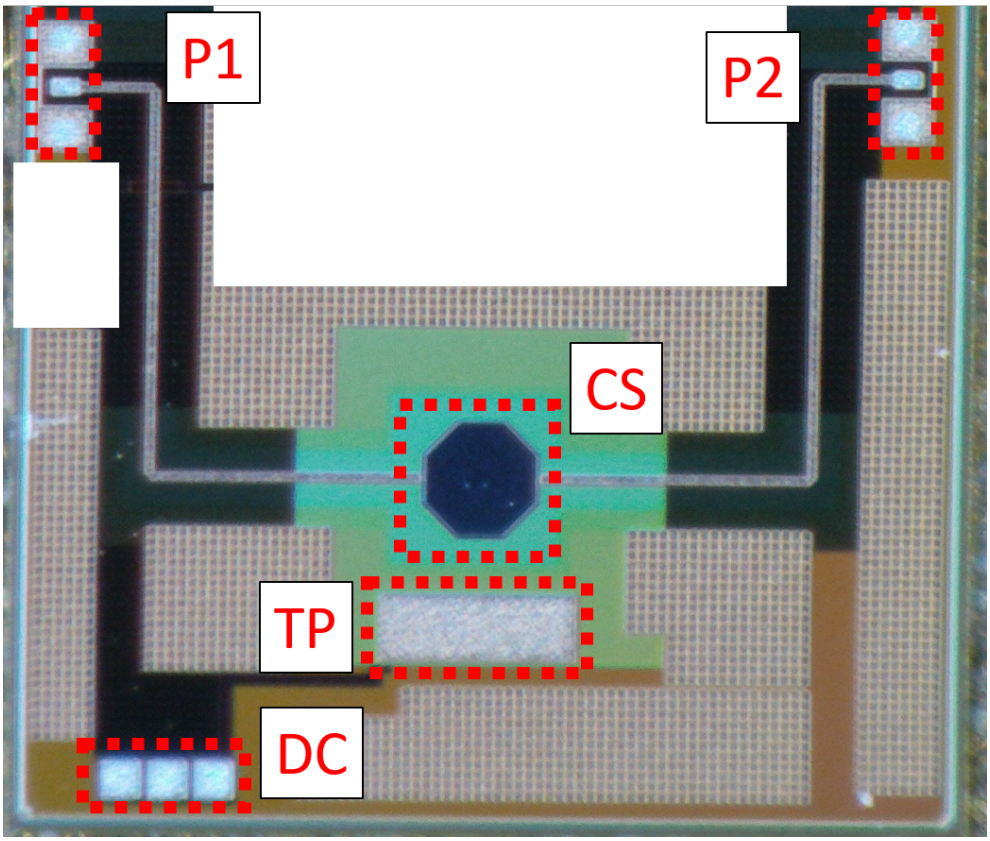

FIGURE 5.12: Photo of tunable SDR circuit with annotations.

corresponding circuit to Fig. 5.11 is shown in Fig. 5.12. Parts from other circuits are painted white. Between the circuit parts are fillers to fulfill design rules. The different colors of shapes appear because of the different heights and thicknesses of the metal and transparent oxide layers. The diodes on the left short side of the tuning patch (TP) are used for the voltage-controlled frequency tuning. They are fed with a three-pin DC probe from the (DC) pads. The resonator sphere is sandwiched between the etched crate (CS) and a small metal cover so that the cover does not touch the probes. The S-parameters were measured at the pads (P1) and (P2) with two GSG-100 probes linked with a VNA. The tuning voltages were changed from $0\,\mathrm{V}$ to $5\,\mathrm{V}$ in $1\,\mathrm{V}$ steps. The measurement result is shown in Fig. 5.13. Measurement of negative voltages was not possible with the used voltage source, but negative voltage would also increase the tuning range. There is no frequency shift identifiable for the measured tuning of the SDR in Fig. 5.13 only an amplitude change of $1.5\,\mathrm{dB}$. The simulation results in Fig. 5.14 show a frequency shift over voltage. There is no explanation found yet as to why the measurement of the tunable SDR behaves differently from the simulation and also different from the measured VCO in the following section. The Q-factor of the tunable filter is around 44 at $103.72\,\mathrm{GHz}$ for the 5V curve and is close to the 53 from [25], which

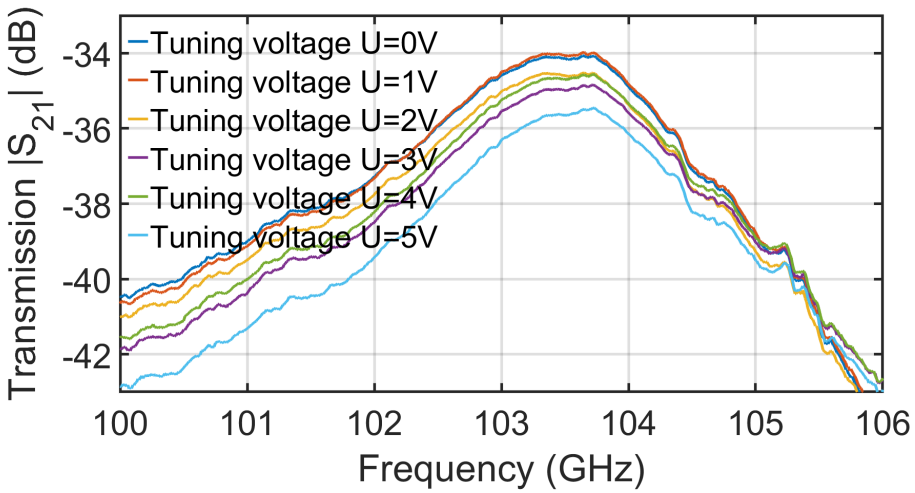

FIGURE 5.13: Voltage tunable SDR measurement results for different tuning voltages.

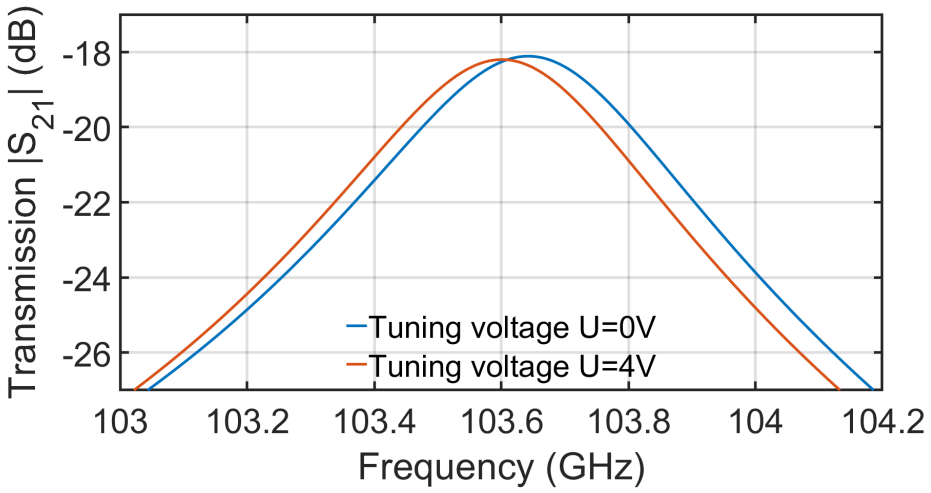

FIGURE 5.14: Voltage tunable SDR simulation results for different tuning voltages.

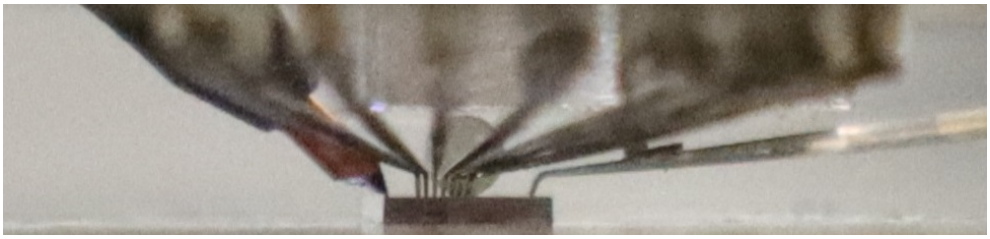

FIGURE 5.15: Photo from the side view of setup VCO glued on top of aluminum plate with top metal cover.

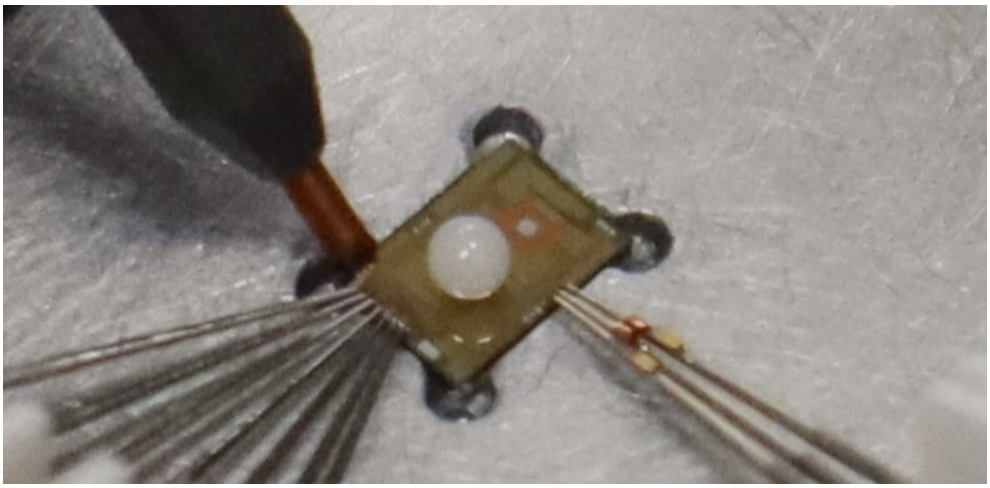

FIGURE 5.16: Photo of setup VCO in aluminum plate embedded. The top cover was removed.

has a weaker transmission. The simulated tuning range from $0\,\mathrm{V}$ to $4\,\mathrm{V}$ is circa $40\,\mathrm{MHz}$.

5.4 VCO

The chip with the VCO was once glued on a metal plate as in Fig. 5.15 and the other time embedded in an aluminum metal plate as in Fig. 5.16 to increase the surrounding metal and therefore the Q-factor and transmission ot the SDR of the oscillator.

A photo of the corresponding circuit to the VCO is shown in Fig. 5.17. Parts from the tunable SDR circuit are painted white. The diodes on the left short side of the tuning patch (TP) control via voltage change the oscillator's frequency. They are fed a three-pin DC probe from the (DC) pads. The sphere for the filter is sandwiched between the etched crate (CS) with two white unwanted dust particles in the Fig. 5.17 and a small metal cover as for the others SDRs. The transistors of the amplifiers (AC) of the VCO are fed with a seven-pin probe from the (TC) pads. The VCO signal was measured with a GSG-100 probe at the (P1) pads, linked with a passive down converter/mixer and spectrum analyzer. The signal frequency was down-mixed with factor 10. The tuning voltages was changed from $0\,\mathrm{V}$ to $3\,\mathrm{V}$ in $1\,\mathrm{V}$ steps. Measurement of negative voltages

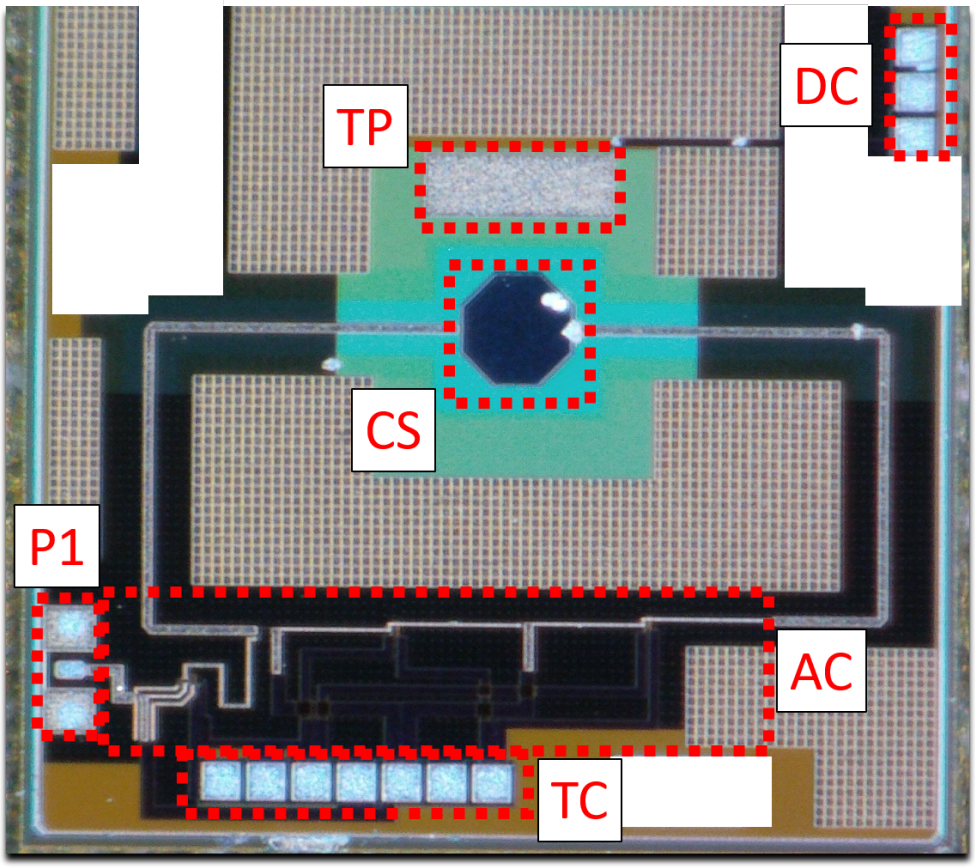

FIGURE 5.17: Photo of VCO circuit with annotations.

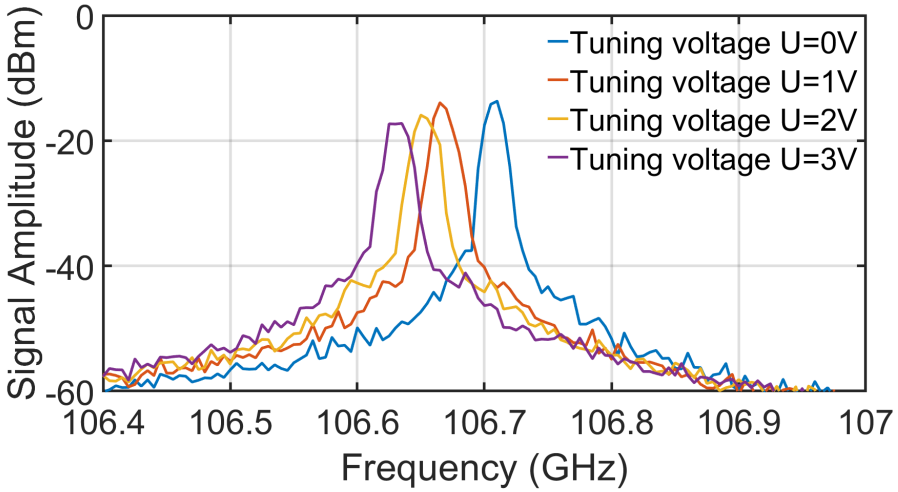

FIGURE 5.18: VCO measurement results for different tuning voltages.

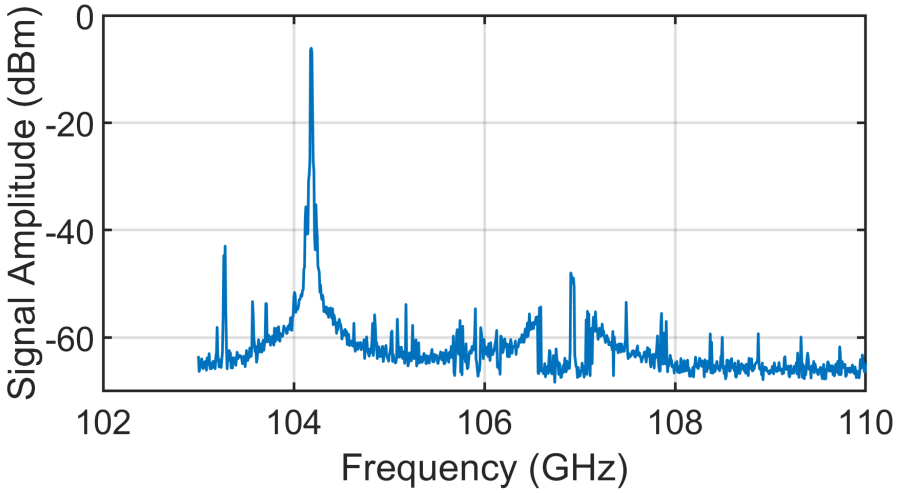

FIGURE 5.19: Strongest VCO measurement results.

was not possible with the used voltage source, but negative voltage would also increase the tuning range of the oscillator. The frequency shift caused by the voltage tuning can be seen in Fig. 5.18. The tuning range of the VCO is $80\,\mathrm{MHz}$ and is circa double as the simulated tuning range of the voltage tunable SDR from Fig. 5.14. There is no reason yet why it is double and not the same. Maybe there are some production errors with the tunable SDR, which did not occur for the VCO. Unfortunately, the VCO signal significantly changes amplitude and frequency. Therefore, the measurement and saving of different tune voltages must be done quickly in a row before the signal changes in amplitude or frequency again. The strongest signal, which could be saved, is in Fig. 5.19 with $-6.104\,\mathrm{dBm}$ amplitude at $104.183\,\mathrm{GHz}$. On the display occurred also amplitudes of more than $-4\,\mathrm{dBm}$ in the area between $104\,\mathrm{GHz}$ and $106.5\,\mathrm{GHz}$. In these

results, the losses of the two cables to connect the down converter with the spectrum analyzer's measurement port and reference signal port are considered, but not the loss of circa $1\,\mathrm{dB}$ caused by the GSG probe. The power consumption of the oscillator is under $35\,\mathrm{mW} = 15.4\,\mathrm{dBm}$. The Signal to Noise Ratio (SNR)$> 55\,\mathrm{dB}$ in Fig. 5.19 and the best measured phase noise is between $83\,\mathrm{dBc/Hz}$ and $89\,\mathrm{dBc/Hz}$ from $100\,\mathrm{kHz}$ to $1\,\mathrm{MHz}$ at the nominal frequency $106.38\,\mathrm{GHz}$.

Chapter 6

Summary, Conclusion, and Outlook

This chapter highlights the sensors and the silicon on-chip application results and ideas for future improvements, tasks, and ideas.

6.1 Summary, Conclusion, and Outlook of the sensors

Several on-chip applications based on dielectric spheres have been presented at microwaves, mm-waves, and sub-THz frequencies. Sensor concepts for permittivity spectroscopy of lossy liquids are explained at microwaves and scaled up to sub-THz frequencies. A definition of sensitivity to compare dielectric sensors with each other is elucidated. It is shown in Chapter 3 that at microwave, low permittivity should be sensed with E-field perpendicular penetrating the MUT, and for very high permittivity, parallel penetration is more sensitive. Also, the sensors with the capacitive gap are more sensitive at microwave frequency because of the better E-field focus. The dielectric sensors are the more sensitive option at mm-waves because of the high Q-factor. In this work, the most sensitive electromagnetic sensor for determining the complex permittivity of LUT at mm-wave and sub-THz is presented with an active volume of $0.35\,\mathrm{nl}$.

Now to differentiate the SDR filter even more to the state of art of filters, such as Fabry-Perot resonators, need help with positioning and accuracy, especially the Fabry-Perot with the production of mirrors. If the MUT is not ideally in the focus of the E-field of the Fabry-Perot resonator or any other resonator, the sensitivity of the spectroscopy decreases rapidly.

Another advantage of the SDR against other resonators is the possibility to use other modes for other applications, too. In [52,77], a second resonance structure was used to compensate for temperature influence on the sensor. In this work, how to compensate, notice, and measure the temperature influence on the whole system with the same resonator and another mode is shown and explained.

The question remains whether it is possible to distinguish cancer cells from healthy cells with these resonators. It is possible to measure volumes small enough for single-cell spectroscopy. Until now, the sensitivity of the presented sensor is not high enough to distinguish cells from cancer cells or to detect cells. The in [12] presented sensor can be sensitive enough with an airtight and temperature-stable measurement environment. Maybe resonators with higher resonance frequencies have to be used. Factor 10 to 30 resulting in $1.9\,\mathrm{THz}$ to $5.7\,\mathrm{THz}$ should be possible to realize now. This would mean, to use Al_2O_3 spheres with a diameter of $0.05\,\mathrm{mm}$ to $0.017\,\mathrm{mm}$. Now the question would be if the signal would be strong enough to create a measurable resonance with this compared to the wavelength much bigger volume of MUT, but now less lossy material because of the higher frequency. Nevertheless, the most sensitive sensors to determine the spectroscopy are presented, and the details are highlighted in this work.

In the future SDRS, it could also be tried to increase the Q-factor of the hole system by using less lossy or no substrate, which would lead to more sensitivity for small changes. Also, the feed coupling could be improved to have less loss and excite fewer unwanted modes. The SDRSs could also be scaled up to THz frequencies and adapted to an integrated on-chip platform.

Packaging is another next big step to take. Only if the setup gets rid of their sensitivity of mechanical vibrations and movements more accurate results can be expected, and the next steps of data processing for temperature compensation, as described in section 3.4.1, for example, could be done. Gluing could be a good solution so that nothing is moving anymore. Another option would be to embed the hole setup in a medium, which holds it and is mechanically stable and has a permittivity similar to air with less loss. Maybe an inverse setup could also work. This means having a full ceramic, glass, or another material block with less loss and a specific permittivity, maybe also surrounded by a material with higher or lower permittivity in which a sphere shape cavity with air or a particular material filling is. With this kind of inverse setup, top and bottom metal could be easily held together with pressure or glue.

Another method to increase the sensitivity and reduce the measurement effort is using mixed-signal paths and measuring the mixed intermediate signal. To one signal path, the SDR sensor with the LUT is added, and the other has a sensor with air as MUT in the tube. Therefore, the absolute intermediate and higher frequencies are shallow for sub-THz measurements. Therefore, the absolute intermediate frequency changes much more for a slight change in the sensor's resonance frequency with the liquid inside the tube. The challenge for this setup would be to get two SDR with a similar frequency to have a low and, therefore, more sensitive mixed intermediate frequency output signal as presented in [112].

Another interesting topic that should be checked is high power application with the spheres especially mm-wave heating of MUT between spheres. This could heat up and kill cancer cells during the measurement.

Electrophoresis and dielectrophoresis are also exciting topics that should be checked more for future applications with SDR sensors. Cells or particles could be trapped with it in the E-field max of the sensor and maybe also pushed away after the measurement. Last, for the spectroscopy, a full-band spectroscopy with a rectangular standard WG with a hole and tube through it is not that easy and, with analytical formulas, impossible to calculate.

6.2 Summary, Conclusion, and Outlook of the silicon on-chip application

This thesis presents more details and background to the antenna and filter of [25]. Also, an active 4-port version of the SDRA, a voltage tunable SDR filter, and a VCO with a ceramic sphere as high Q resonator on-chip produced with BiCMOS SiGe technology is shown. The SiGe technology was extended with an extra process etching a crate in the BEOL for sphere positioning. The antennas have a simulated directivity of circa $10\,\mathrm{dBi}$ and simulated efficiency of $33\,\%$. The resonator with a maximum measured Q of 143 was also used as a voltage tunable filter and for a VCO both working at $\approx 100\,\mathrm{GHz}$ and with circa $100\,\mathrm{MHz}$ tuning range for $4\,\mathrm{V}$ tuning range. The power consumption of the VCO is below $35\,\mathrm{mW}$, the $SNR > 55\,\mathrm{dB}$ and the phase noise is between $83\,\mathrm{dBc/Hz}$ and $89\,\mathrm{dBc/Hz}$ from $100\,\mathrm{kHz}$ to $1\,\mathrm{MHz}$ at the nominal frequency $106.38\,\mathrm{GHz}$. The task to create on silicon chips application as antenna, filter, and oscillator without LBE is full-filled. A new benchmark of Q-factor is set for the filters.

The next step with this technology should be to build up complete circuit systems such as radar and improve the application's performance. Another task is the packaging to keep the sphere in place. Simple gluing or a lossless dielectric cover for the antenna could be the solution: For the resonator, the solution could also be gluing or some from the top sandwiching box with space between box side walls and the sphere if this box should be made entirely out of metal, or metal-coated, or just the top part has to be figured out.

Bibliography

[1] L.-F. Chen, C. K. Ong, C. Neo, V. V. Varadan, and V. K. Varadan, *Microwave electronics: measurement and materials characterization*. John Wiley & Sons, 2004.

[2] A. A. Abduljabar, D. J. Rowe, A. Porch, and D. A. Barrow, "Novel microwave microfluidic sensor using a microstrip split-ring resonator," *IEEE Transactions on Microwave Theory and Techniques*, vol. 62, no. 3, pp. 679–688, 2014.

[3] H. Hamzah, J. Lees, and A. Porch, "Split ring resonator with optimised sensitivity for microfluidic sensing," *Sensors and Actuators A: Physical*, vol. 276, pp. 1–10, 2018.

[4] H. Hamzah, A. Abduljabar, J. Lees, and A. Porch, "A compact microwave microfluidic sensor using a re-entrant cavity," *Sensors*, vol. 18, no. 3, p. 910, 2018.

[5] A. H. Sklavounos and N. S. Barker, "Liquid-permittivity measurements using a rigorously modeled overmoded cavity resonator," *IEEE Transactions on Microwave Theory and Techniques*, vol. 62, no. 6, pp. 1363–1372, 2014.

[6] S. Liu, I. Ocket, D. Schreurs, W. De Raedt, and B. Nauwelaers, "A 90 GHz liquid sensing substrate integrated cavity resonator in LTCC for microfluidic sensing applications," in *2014 IEEE MTT-S International Microwave Workshop Series on RF and Wireless Technologies for Biomedical and Healthcare Applications (IMWS-Bio2014)*, pp. 1–3, 2014.

[7] A. I. Gubin, A. A. Barannik, N. T. Cherpak, I. A. Protsenko, S. Pud, A. Offenhäusser, and S. A. Vitusevich, "Whispering-gallery-mode resonator technique with microfluidic channel for permittivity measurement of liquids," *IEEE Transactions on Microwave Theory and Techniques*, vol. 63, no. 6, pp. 2003–2009, 2015.

[8] A. Barannik, N. Cherpak, A. Gubin, I. Protsenko, and S. Vitusevich, "WGM resonators with microfluidic channel for sub-mm wave characterization of biological liquids," in *2016 German Microwave Conference (GeMiC)*, pp. 15–18, IEEE, 2016.

[9] S. Hanham, C. Watts, W. Otter, S. Lucyszyn, and N. Klein, "Dielectric measurements of nanoliter liquids with a photonic crystal resonator at terahertz frequencies," *Applied Physics Letters*, vol. 107, no. 3, p. 032903, 2015.

[10] D. L. Cuenca, G. Alavi, and J. Hesselbarth, "On-chip mm-wave spherical dielectric resonator bandpass filter," in *2017 IEEE MTT-S International Microwave Symposium (IMS)*, pp. 1460–1463, 2017.

[11] G. Sterzl and J. Hesselbarth, "Characterization of permittivity of liquids-in-flow with spherical dielectric resonators," in *2020 50th European Microwave Conference (EuMC)*, pp. 901–904, 2021.

[12] G. Sterzl, U. Dey, and J. Hesselbarth, "Subnanoliter sensing of dielectric properties of liquid-in-flow at 190 GHz," *IEEE Microwave and Wireless Components Letters*, vol. 31, no. 6, pp. 808–811, 2021.

[13] B. Dehlink, M. Engl, K. Aufinger, and H. Knapp, "Integrated bandpass filter at 77 GHz in SiGe technology," *IEEE Microwave and Wireless Components Letters*, vol. 17, no. 5, pp. 346–348, 2007.

[14] K. Schmalz, J. Borngraber, M. Kaynak, W. Winkler, J. Wessel, M. Neshat, and S. Safavi-Naeini, "A 120 GHz dielectric sensor in SiGe BiCMOS," *IEEE Microwave and Wireless Components Letters*, vol. 23, no. 1, pp. 46–48, 2012.

[15] D. Wang, J. Yun, M. Eissa, M. Kucharski, K. Schmalz, A. Malignaggi, Y. Wang, J. Borngräber, Y. Liang, H. Ng, *et al.*, "207-257 GHz integrated sensing readout system with transducer in a 130-nm SiGe BiCMOS technology," in *2019 IEEE MTT-S International Microwave Symposium (IMS)*, pp. 496–499, 2019.

[16] P. Rynkiewicz, A.-L. Franc, F. Coccetti, S. T. Wipf, M. Wietstruck, M. Kaynak, and G. Prigent, "Tunable dual-mode ring filter based on BiCMOS embedded MEMS in V-band," in *2017 IEEE Asia Pacific Microwave Conference (APMC)*, pp. 124–127, 2017.

[17] C. Mustacchio, L. Boccia, E. Arnieri, and G. Amendola, "W-band on-chip monopole antenna in standard 0.13 μm SiGe BiCMOS technology," in *2019 14th International Conference on Advanced Technologies, Systems and Services in Telecommunications (TELSIKS)*, pp. 138–140, IEEE, 2019.

[18] M. S. Khan, F. A. Tahir, and H. M. Cheema, "Design of bowtie-slot on-chip antenna backed with E-shaped FSS at 94 GHz," in *2016 10th European Conference on Antennas and Propagation (EuCAP)*, pp. 1–3, IEEE, 2016.

[19] M. Jenning, B. Klein, R. Hahnel, and D. Plettemeier, "On-chip integrated antennas for 200 GHz applications," in *2015 IEEE International Conference on Ubiquitous Wireless Broadband (ICUWB)*, pp. 1–5, 2015.

[20] H. J. Ng, J. Wessel, D. Genschow, R. Wang, Y. Sun, and D. Kissinger, "Miniaturized 122 GHz system-on-chip radar sensor with on-chip antennas utilizing a novel antenna design approach," in *2016 IEEE MTT-S International Microwave Symposium (IMS)*, pp. 1–4, 2016.

[21] R. Hahnel, M. Becker, B. Klein, and D. Plettemeier, "Integrated dual polarized on-chip antenna for mm-wave applications," in *2017 IEEE International Symposium on Antennas and Propagation & USNC/URSI National Radio Science Meeting*, pp. 1817–1818, 2017.

[22] M. V. Thayyil, P. V. Testa, C. Carta, and F. Ellinger, "A 190 GHz inset-fed patch antenna in SiGe BEOL for on-chip integration," in *2018 IEEE Radio and Antenna Days of the Indian Ocean (RADIO)*, pp. 1–2, 2018.

[23] X.-D. Deng, Y. Li, C. Liu, W. Wu, and Y.-Z. Xiong, "340 GHz on-chip 3-D antenna with 10 dBi gain and 80% radiation efficiency," *IEEE Transactions on Terahertz Science and Technology*, vol. 5, no. 4, pp. 619–627, 2015.

[24] K. Schmalz, J. Borngraber, W. Debski, M. Elkhouly, R. Wang, P. Neumaier, and H.-W. Hubers, "245 GHz SiGe transmitter array for gas spectroscopy," in *2014 IEEE Compound Semiconductor Integrated Circuit Symposium (CSICS)*, pp. 1–4, 2014.

[25] G. Sterzl, Y. Zhu, J. Hesselbarth, C. Carta, M. Lisker, and F. Ellinger, "Self-aligned on-chip spherical dielectric resonators and antennas for SiGe MMIC," in *2022 Asia-Pacific Microwave Conference (APMC)*, pp. 686–688, 2022.

[26] R. Richtmyer, "Dielectric resonators," *Journal of Applied Physics*, vol. 10, no. 6, pp. 391–398, 1939.

[27] S. Long, M. McAllister, and L. Shen, "The resonant cylindrical dielectric cavity antenna," *IEEE Transactions on Antennas and Propagation*, vol. 31, no. 3, pp. 406–412, 1983.

[28] D. L. Cuenca, J. Hesselbarth, and G. Alavi, "Chip-mounted dielectric resonator antenna with alignment and testing features," in *2016 46th European Microwave Conference (EuMC)*, pp. 723–726, 2016.

[29] J. G. Marin, A. A. Baba, J. Hesselbarth, R. M. Hashmi, and K. P. Esselle, "Millimeter-wave low-loss multifeed superstrate-based antenna," *IEEE Transactions on Antennas and Propagation*, vol. 68, no. 5, pp. 3387–3396, 2020.

[30] U. Dey and J. Hesselbarth, "Building blocks for a millimeter-wave multiport multicast chip-to-chip interconnect based on dielectric waveguides," *IEEE Transactions on Microwave Theory and Techniques*, vol. 66, no. 12, pp. 5508–5520, 2018.

[31] C.-T. Chang, C.-L. Yang, U. Dey, and J. Hesselbarth, "Measuring vital signs on fingertip using K-band spherical dielectric resonator," in *2020 50th European Microwave Conference (EuMC)*, pp. 933–936, 2021.

[32] J. C. Maxwell, "A dynamical theory of the electromagnetic field," *Philosophical Transactions of the Royal Society of London*, no. 155, pp. 459–512, 1865.

[33] D. M. Pozar, *Microwave engineering*. John wiley & sons, 2011.

[34] W. E. Steven, *Electromagnetics Vol 2*. Virginia Tech Publishing, 2020.

[35] C. A. Balanis, *Adanced engineering electromagnetics*. John wiley & sons, 1989.

[36] C. F. Bohren and D. R. Huffman, *Absorption and scattering of light by small particles*. John Wiley & Sons, 2008.

[37] D. L. Cuenca, *On-chip spherical dielectric resonator-based millimeter-wave components*. PhD thesis, University of Stuttgart, 2018.

[38] E. Shaforost, N. Klein, S. Vitusevich, A. Barannik, and N. Cherpak, "High sensitivity microwave characterization of organic molecule solutions of nanoliter volume," *Applied Physics Letters*, vol. 94, no. 11, p. 112901, 2009.

[39] H. Banting and C. E. Saavedra, "Dielectric spectroscopy of fluids and polymers for microwave microfluidic circuits and antennas," *IEEE Transactions on Microwave Theory and Techniques*, vol. 69, no. 1, pp. 337–343, 2020.

[40] J. R. Macdonald, "Impedance spectroscopy," *Annals of Biomedical Engineering*, vol. 20, pp. 289–305, 1992.

[41] H. M. Hamzah, *Microwave microfluidic resonant sensors and applicators*. PhD thesis, Cardiff University, 2017.

[42] A. A. Abduljabar, *Compact microwave microfluidic sensors and applicator*. PhD thesis, Cardiff University, 2016.

[43] F. Antwerpes, N. van den Höfel, and J. Nolte, "Spektroskopie." `https://flexikon.doccheck.com/de/Spektroskopie`, Feb. 2022.

[44] T. Tosaka, K. Fujii, K. Fukunaga, and A. Kasamatsu, "Development of complex relative permittivity measurement system based on free-space in 220–330-GHz range," *IEEE Transactions on Terahertz Science and Technology*, vol. 5, no. 1, pp. 102–109, 2014.

[45] O. L. Bo and E. Nyfors, "Application of microwave spectroscopy for the detection of water fraction and water salinity in water/oil/gas pipe flow," *Journal of Non-Crystalline Solids*, vol. 305, no. 1-3, pp. 345–353, 2002.

[46] W. Scott and G. Smith, "Dielectric spectroscopy using monopole antennas of general electrical length," *IEEE Transactions on Antennas and Propagation*, vol. 34, no. 7, pp. 919–929, 1986.

[47] M. A. Suster and P. Mohseni, "An RF/microwave microfluidic sensor based on a center-gapped microstrip line for miniaturized dielectric spectroscopy," in *2013 IEEE MTT-S International Microwave Symposium Digest (MTT)*, pp. 1–3, 2013.

[48] X. Bao, S. Liu, I. Ocket, J. Bao, D. Schreurs, S. Zhang, C. Cheng, K. Feng, and B. Nauwelaers, "A general line–line method for dielectric material characterization using conductors with the same cross-sectional geometry," *IEEE Microwave and Wireless Components Letters*, vol. 28, no. 4, pp. 356–358, 2018.

[49] X. Bao, S. Liu, I. Ocket, J. Bao, D. Kil, S. Zhang, C. Cheng, K. Feng, G. Avolio, B. Puers, D. Schreurs, and B. Nauwelaers, "Coplanar waveguide for dielectric material measurements at frequencies from 140 GHz to 220 GHz," in *2017 90th ARFTG Microwave Measurement Symposium (ARFTG)*, pp. 1–4, 2017.

[50] H. Yamamoto, "Measurement of the dielectric constant and loss tangent of liquids by the transmitted-reflected wave method in the millimeter-wave range," *IEEE Transactions on Microwave Theory and Techniques*, vol. 19, no. 10, pp. 827–829, 1971.

[51] H. Hamzah, A. A. Abduljabar, and A. Porch, "High Q microwave microfluidic sensor using a central gap ring resonator," *IEEE Transactions on Microwave Theory and Techniques*, vol. 68, no. 5, pp. 1830–1838, 2020.

[52] A. A. Abduljabar, H. Choi, D. A. Barrow, and A. Porch, "Adaptive coupling of resonators for efficient microwave heating of microfluidic systems," *IEEE*

Transactions on Microwave Theory and Techniques, vol. 63, no. 11, pp. 3681–3690, 2015.

[53] E. L. Chuma, Y. Iano, G. Fontgalland, L. L. B. Roger, and H. Loschi, "PCB-integrated non-destructive microwave sensor for liquid dielectric spectroscopy based on planar metamaterial resonator," *Sensors and Actuators A: Physical*, vol. 312, p. 112112, 2020.

[54] L. Devlin, G. Pearson, J. Pittock, and B. Hunt, "RF and microwave component development in LTCC," in *IMAPS Nordic 38th Annu. Conf*, pp. 96–110, 2001.

[55] S. Liu, I. Ocket, B. Nauwelaers, and D. Schreurs, "Millimeter wave on-wafer measurement of yeast cell suspension using a CPW test fixture in LCP technology," in *82nd ARFTG Microwave Measurement Conference*, pp. 1–4, IEEE, 2013.

[56] M. Afsar, "Dielectric measurements of millimeter-wave materials," *IEEE Transactions on Microwave Theory and Techniques*, vol. 32, no. 12, pp. 1598–1609, 1984.

[57] A. N. Leontakianakos, "Determination of water vapor by microwave spectroscopy with application to quality control of natural gas," *IEEE Transactions on Instrumentation and Measurement*, vol. 41, no. 3, pp. 370–374, 1992.

[58] H. Hallil, P. Menini, and H. Aubert, "Novel millimeter-wave gas sensor using dielectric resonator with sensitive layer on TiO_2," in *Sensors, 2009 IEEE*, pp. 226–228, 2009.

[59] H. Yu, B. Yu, X. Ding, J. S. Gómez-Díaz, and Q. J. Gu, "A 162 GHz ring resonator based high resolution dielectric sensor," in *2020 IEEE/MTT-S International Microwave Symposium (IMS)*, pp. 233–236, 2020.

[60] W. J. Otter, S. M. Hanham, N. M. Ridler, G. Marino, N. Klein, and S. Lucyszyn, "100 GHz ultra-high Q-factor photonic crystal resonators," *Sensors and Actuators A: Physical*, vol. 217, pp. 151–159, 2014.

[61] N. Chaffey, B. Alberts, A. Johnson, J. Lewis, M. Raff, K. Roberts, and P. Walter, "Molecular biology of the cell. 4th edn.," *Annals of Botany*, vol. 91, pp. 401–401, 02 2003.

[62] J. H. Wilson, T. Hunt, and B. Alberts, *Molecular biology of the cell. The problems book / John Wilson, Tim Hunt.* New York: Garland Publishing, rev. ed. ed., 1994.

[63] J. Wesse, K. Schmalz, F. I. Jamal, and D. Kissinger, "Contactless investigation of dielectric samples with a high-Q millimeter-wave sensor," in *2018 40th Annual International Conference of the IEEE Engineering in Medicine and Biology Society (EMBC)*, pp. 5926–5929, 2018.

[64] K. Cheung, S. Gawad, and P. Renaud, "Impedance spectroscopy flow cytometry: on-chip label-free cell differentiation," *Cytometry Part A*, vol. 65, no. 2, pp. 124–132, 2005.

[65] A. A. Abduljabar, X. Yang, D. A. Barrow, and A. Porch, "Modelling and measurements of the microwave dielectric properties of microspheres," *IEEE Transactions on Microwave Theory and Techniques*, vol. 63, no. 12, pp. 4492–4500, 2015.

[66] S. Gawad, K. Cheung, U. Seger, A. Bertsch, and P. Renaud, "Dielectric spectroscopy in a micromachined flow cytometer: theoretical and practical considerations," *Lab on a Chip*, vol. 4, no. 3, pp. 241–251, 2004.

[67] M. Li, J. Xu, M. Romero-Gonzalez, S. A. Banwart, and W. E. Huang, "Single cell Raman spectroscopy for cell sorting and imaging," *Current opinion in biotechnology*, vol. 23, no. 1, pp. 56–63, 2012.

[68] K. Grenier, D. Dubuc, T. Chen, F. Artis, T. Chretiennot, M. Poupot, and J.-J. Fournie, "Recent advances in microwave-based dielectric spectroscopy at the cellular level for cancer investigations," *IEEE Transactions on Microwave Theory and Techniques*, vol. 61, no. 5, pp. 2023–2030, 2013.

[69] K. Grenier, D. Dubuc, M. Poupot, and J.-J. Fournié, "Microwave signatures of alive B-lymphoma cells suspensions," in *2011 IEEE Topical Conference on Biomedical Wireless Technologies, Networks, and Sensing Systems*, pp. 95–98, 2011.

[70] C. Watts, *Electromagnetic sensing of cell suspensions in microfluidic systems*. PhD thesis, Imperial College London, 2017.

[71] K. Shih, P. Pitchappa, M. Manjappa, C. P. Ho, R. Singh, and C. Lee, "Microfluidic metamaterial sensor: Selective trapping and remote sensing of microparticles," *Journal of Applied Physics*, vol. 121, no. 2, p. 023102, 2017.

[72] X. Xu, P. Sarder, Z. Li, and A. Nehorai, "Optimization of microfluidic microsphere-trap arrays," *Biomicrofluidics*, vol. 7, no. 1, p. 014112, 2013.

[73] S. Blatt, *Dielectrophoresis of single-walled carbon nanotubes*. Karlsruhe Institute of Technology, 2008.

[74] T. Chen, F. Artis, D. Dubuc, J. Fournie, M. Poupot, and K. Grenier, "Microwave biosensor dedicated to the dielectric spectroscopy of a single alive biological cell in its culture medium," in *2013 IEEE MTT-S International Microwave Symposium Digest (MTT)*, pp. 1–4, 2013.

[75] Y. Ning, C. Multari, X. Luo, C. Palego, X. Cheng, J. C. Hwang, A. Denzi, C. Merla, F. Apollonio, and M. Liberti, "Broadband electrical detection of individual biological cells," *IEEE Transactions on Microwave Theory and Techniques*, vol. 62, no. 9, pp. 1905–1911, 2014.

[76] U. Kaatze, "Complex permittivity of water as a function of frequency and temperature," *Journal of Chemical and Engineering Data*, vol. 34, no. 4, pp. 371–374, 1989.

[77] A. A. Abduljabar, N. Clark, J. Lees, and A. Porch, "Dual mode microwave microfluidic sensor for temperature variant liquid characterization," *IEEE Transactions on Microwave Theory and Techniques*, vol. 65, no. 7, pp. 2572–2582, 2017.

[78] J. A. G. Marín, *Functional Dielectric-Based Multi-Feed Antennas*. PhD thesis, University of Stuttgart, 2020.

[79] D. Di Marco, K. Drissi, N. Delhote, O. Tantot, P.-M. Geffroy, S. Verdeyme, and T. Chartier, "Dielectric properties of pure alumina from 8 GHz to 73 GHz," *Journal of the European Ceramic Society*, vol. 36, no. 14, pp. 3355–3361, 2016.

[80] Evonik Industries AG, *Product Information ROHACELL® HF Polymethacrylimide Foam*, 2011.

[81] A. P. Gregory and R. Clarke, "Tables of the complex permittivity of dielectric reference liquids at frequencies up to 5 GHz.," *National Physical Laboratory*, 2012.

[82] T. Sato and R. Buchner, "Dielectric relaxation processes in ethanol/water mixtures," *The Journal of Physical Chemistry A*, vol. 108, no. 23, pp. 5007–5015, 2004.

[83] J. Kindt and C. Schmuttenmaer, "Far-infrared dielectric properties of polar liquids probed by femtosecond terahertz pulse spectroscopy," *The Journal of Physical Chemistry*, vol. 100, no. 24, pp. 10373–10379, 1996.

[84] J. Barthel, K. Bachhuber, R. Buchner, and H. Hetzenauer, "Dielectric spectra of some common solvents in the microwave region. Water and lower alcohols," *Chemical Physics Letters*, vol. 165, no. 4, pp. 369–373, 1990.

[85] R. Davis, "Why the mohs scale remains relevant for metrology [basic metrology]," *IEEE Instrumentation & Measurement Magazine*, vol. 21, no. 6, pp. 49–51, 2018.

[86] M. Naftaly and A. Gregory, "Terahertz and microwave optical properties of single-crystal quartz and vitreous silica and the behavior of the boson peak," *Applied Sciences*, vol. 11, no. 15, p. 6733, 2021.

[87] MathWorks, "movmean." Online documentation, 2021.

[88] J. Barthel and R. Buchner, "High frequency permittivity and its use in the investigation of solution properties," *Pure and Applied Chemistry*, vol. 63, no. 10, pp. 1473–1482, 1991.

[89] J. Krupka, P. Kamiński, R. Kozłowski, B. Surma, A. Dierlamm, and M. Kwestarz, "Dielectric properties of semi-insulating silicon at microwave frequencies," *Applied Physics Letters*, vol. 107, no. 8, p. 082105, 2015.

[90] Z. Xie, W. Xue, H. Chen, and Y. Huang, "Mechanical and thermal properties of 99% and 92% alumina at cryogenic temperatures," *Ceramics International*, vol. 37, no. 7, pp. 2165–2168, 2011.

[91] C. Grosse, "A program for the fitting of Debye, Cole–Cole, Cole–Davidson, and Havriliak–Negami dispersions to dielectric data," *Journal of Colloid and Interface Science*, vol. 419, pp. 102–106, 2014.

[92] C. Rosa and E. C. de Oliveira, "Relaxation equations: fractional models," *Journal of Physical Mathematics*, vol. 6, no. 2, pp. 1 – 7, 2015.

[93] M. B. Sano, R. C. Gallo-Villanueva, B. H. Lapizco-Encinas, and R. V. Davalos, "Simultaneous electrokinetic flow and dielectrophoretic trapping using perpendicular static and dynamic electric fields," *Microfluidics and Nanofluidics*, vol. 15, pp. 599–609, 2013.

[94] T. Heida, W. Rutten, and E. Marani, "Understanding dielectrophoretic trapping of neuronal cells: modelling electric field, electrode-liquid interface and fluid flow," *Journal of Physics D: Applied Physics*, vol. 35, no. 13, p. 1592, 2002.

[95] Y. Wu, Y. Ren, Y. Tao, L. Hou, and H. Jiang, "Large-scale single particle and cell trapping based on rotating electric field induced-charge electroosmosis," *Analytical Chemistry*, vol. 88, no. 23, pp. 11791–11798, 2016.

[96] S. K. Sia and G. M. Whitesides, "Microfluidic devices fabricated in poly (dimethylsiloxane) for biological studies," *Electrophoresis*, vol. 24, no. 21, pp. 3563–3576, 2003.

[97] A. Petosa and A. Ittipiboon, "Dielectric resonator antennas: a historical review and the current state of the art," *IEEE antennas and Propagation Magazine*, vol. 52, no. 5, pp. 91–116, 2010.

[98] R. K. Mongia and P. Bhartia, "Dielectric resonator antennas—a review and general design relations for resonant frequency and bandwidth," *International Journal of Microwave and Millimeter-Wave Computer-Aided Engineering*, vol. 4, no. 3, pp. 230–247, 1994.

[99] K. W. Leung, E. H. Lim, and X. S. Fang, "Dielectric resonator antennas: from the basic to the aesthetic," *Proceedings of the IEEE*, vol. 100, no. 7, pp. 2181–2193, 2012.

[100] P. Bijumon, Y. Antar, A. Freundorfer, and M. Sayer, "Dielectric resonator antenna on silicon substrate for system on-chip applications," *IEEE Transactions on Antennas and Propagation*, vol. 56, no. 11, pp. 3404–3410, 2008.

[101] R. Karim, A. Iftikhar, and R. Ramzan, "Performance-issues-mitigation-techniques for on-chip-antennas–recent developments in RF, mm-wave, and THz bands with future directions," *IEEE Access*, vol. 8, pp. 219577–219610, 2020.

[102] R. Karim, A. Iftikhar, B. Ijaz, and I. B. Mabrouk, "The potentials, challenges, and future directions of on-chip-antennas for emerging wireless applications—a comprehensive survey," *IEEE Access*, vol. 7, pp. 173897–173934, 2019.

[103] L. Pantoli, H. Bello, G. Leuzzi, H. Ng, and D. Kissinger, "SiGe sub-THz VCOs design approach for imaging applications," in *2020 International Workshop on Integrated Nonlinear Microwave and Millimetre-Wave Circuits (INMMiC)*, pp. 1–3, IEEE, 2020.

[104] M. Funabashi, K. Ohata, K. Onda, K. Hosoya, T. Inoue, M. Kuzuhara, K. Kanckawa, and Y. Kobayashi, "A V-band AlGaAs/InGaAs heterojunction FET MMIC dielectric resonator oscillator," in *Proceedings of 1994 IEEE GaAs IC Symposium*, pp. 30–33, 1994.

[105] K. Hosoya, T. Inoue, M. Funabashi, and K. Ohata, "Systematic evaluation and analysis for 60-GHz dielectric resonators coupled to a microstrip line on a GaAs substrate," *IEEE Transactions on Microwave Theory and Techniques*, vol. 46, no. 4, pp. 352–358, 1998.

[106] K. Hosoya, K. Ohata, T. Inoue, M. Funabashi, and M. Kuzuhara, "Temperature- and structural-parameters-dependent characteristics of V-band heterojunction FET MMIC DROs," *IEEE Transactions on Microwave Theory and Techniques*, vol. 51, no. 2, pp. 347–355, 2003.

[107] L. Zhou, W.-Y. Yin, J. Wang, and L.-S. Wu, "Dielectric resonators with high Q-factor for tunable low phase noise oscillators," *IEEE Transactions on Components, Packaging and Manufacturing Technology*, vol. 3, no. 6, pp. 1008–1015, 2013.

[108] K. Hosoya, K. Ohata, M. Funabashi, T. Inoue, and M. Kuzuhara, "V-band HJFET MMIC DROs with low phase noise, high power, and excellent temperature stability," *IEEE Transactions on Microwave Theory and Techniques*, vol. 51, no. 11, pp. 2250–2258, 2003.

[109] R. Kaesbach, M. Van Delden, and T. Musch, "A fixed-frequency, tunable dielectric resonator oscillator with phase-locked loop stabilization," in *2022 Asia-Pacific Microwave Conference (APMC)*, pp. 728–730, IEEE, 2022.

[110] S. B. Fischer, "Voltage-controlled oscillator stabilized by a spherical dielectric resonator," Master's thesis, University of Stuttgart, 2018.

[111] J. G. Marin and J. Hesselbarth, "Circularly-polarized on-chip dielectric resonator antenna," *IET Conference Proceedings*, p. 575, 2018.

[112] A. P. Saghati, J. S. Batra, J. Kameoka, and K. Entesari, "A metamaterial-inspired wideband microwave interferometry sensor for dielectric spectroscopy of liquid chemicals," *IEEE Transactions on Microwave Theory and Techniques*, vol. 65, no. 7, pp. 2558–2571, 2017.

Appendix A

Publications

- J. Hesselbarth, G. Sterzl and J. Moreira, "Probing Millimeter-Wave Antennas and Arrays in their Reactive Near-Field," *2019 49th European Microwave Conference (EuMC)*, Paris, October 2019.
- G. Sterzl, J. Hesselbarth, “Characterization of Permittivity of Liquids-in-Flow with Spherical Dielectric Resonators,” *2020 50th European Microwave Conference (EuMC)*, Utrecht, January 2021.
- G. Sterzl, U. Dey and J. Hesselbarth “Subnanoliter Sensing of Dielectric Properties of Liquid-in-Flow at 190 GHz,” *IEEE Microwave and Wireless Components Letters, vol. 31, no. 6, pp. 808-811*, June 2021.
- G. Sterzl, Y. Zhu, J. Hesselbarth, C. Carta, M. Lisker and F. Ellinger, “Self-Aligned on-Chip Spherical Dielectric Resonators and Antennas for SiGe MMIC,” *2022 Asia-Pacific Microwave Conference (APMC)*, Yokohama, December 2022.
- Y. Zhu, G. Sterzl, J. Hesselbarth, T. Meister and F. Ellinger, "Low Phase Noise 104 GHz Oscillator Using Self-Aligned On-Chip Voltage-Tunable Spherical Dielectric Resonator in 130-nm SiGe BiCMOS," *2024 IEEE 24th Topical Meeting on Silicon Monolithic Integrated Circuits in RF Systems (SiRF)*, San Antonio, TX, USA, February 2024.